Imperial College of Science, Technology and Medicine
Department of Physics

Investigating Optical Absorption in Organic Semiconductors Using a Coarse-Grained Approach

Alise Virbule

Submitted in part fulfilment of the requirements for the degree of
Doctor of Philosophy in Physics, Imperial College London, March 2021

Declaration of originality

All the work in this thesis is my original work undertaken between 2015 and 2020 under the supervision of Prof Jenny Nelson and Dr Johannes Lischner, unless otherwise specified and appropriately cited in the text.

Alise Virbule, March 2021

Copyright declaration

The copyright of this thesis rests with the author. Unless otherwise indicated, its contents are licensed under a Creative Commons Attribution-Non Commercial 4.0 International Licence (CC BY-NC).

Under this licence, you may copy and redistribute the material in any medium or format. You may also create and distribute modified versions of the work. This is on the condition that: you credit the author and do not use it, or any derivative works, for a commercial purpose.

When reusing or sharing this work, ensure you make the licence terms clear to others by naming the licence and linking to the licence text. Where a work has been adapted, you should indicate that the work has been changed and describe those changes.

Please seek permission from the copyright holder for uses of this work that are not included in this licence or permitted under UK Copyright Law.

Abstract

Organic semiconductors have attracted great interest as candidate materials for solar cells, light-emitting diodes and other photonic applications. The performance of such devices depends upon the spectral range and strength of the optical absorption, as well as other material properties. Optical transition energies and strengths are controlled in turn by the chemical structure of the (macro)molecule and its conformation; however, the large conformational phase space of conjugated polymers means that the chemical structure – optical property relationship is not trivial to determine. In the solid state, the conformations and interactions of the molecules are a function of process conditions and hard to control, and yet they control the optoelectronic properties of the material. Whilst many studies have sought to develop and validate computationally efficient methods for prediction of transition energies, relatively few have addressed prediction of transition strength. Methods such as time dependent density functional theory are widely used to complement experimental studies but are too computationally expensive to access the length scales required to fully explain the observed structure-property relationships, especially for polymers with large repeat units or complex phase behaviour. Coarse-grained models of optical properties such as tight-binding exciton models can be used to examine the structure-property relationships at longer length scales, but these use approximations to the electron-hole interactions that do not accurately reproduce the experimentally observed trends in absorption strength as a function of molecular structure. I therefore implement a coarse-grained model using parameters from ab initio calculations as a tool to further our understanding of the relationship between the conformation of pi-conjugated macromolecules and their optical properties. I apply this approach to study two conjugated polymers and show how effects of conformational changes on their optical absorption spectra can be linked to changes in the parameters that characterise the electronic intermonomer interactions in the model.

Acknowledgements

I would like to greatly thank my supervisors Jenny and Johannes for encouraging and supporting me through the ups and downs of this academic adventure, and especially for their great help in the challenging final stages. Additionally, I am grateful to Eric Bittner and Michael Bearpark for taking the time to share their expertise and examine this thesis, your feedback was key to making this thesis a more complete and coherent piece of writing that I can be proud of.

I would also like to acknowledge the Engineering and Physical Sciences Research Council for funding my studies and research at Imperial College London.

There are a lot of people without whom these years would not have been possible or as enjoyable. Firstly, my thanks go to the staff and students from the Centre for Doctoral Training in Theory and Simulation of Materials, especially my friends from Cohort 6. Additionally, it was a great pleasure to be part of two amazing research groups - my understanding of electronic structure theory was regularly challenged and broadened during interesting and sometimes intimidating discussions with Johannes' students and postdocs, and being part of Jenny's group gave me the chance to deeply understand a large variety of research questions in the study of organic semiconductors ranging from synthetic chemistry, experimental techniques and theoretical methods spanning many length scales. Additionally, it was a pleasure to work alongside friends and colleagues from other research groups in office H1101, which has the best view in the whole college.

I am very grateful for this experience, in addition to receiving a doctoral degree I have gained a lot of skills and experiences that have enabled me to pursue a career that I am very passionate about. This journey has also had many challenging moments, especially in the later stages of writing up and working on corrections, which coincided with a lot of hard work addressing a complex set of mental health struggles. I would not have been able to get through these last stages without my amazing support network - my family, my friends at home, "home home" and across the globe, therapists and doctors, and most importantly my favourite person who has supported me through the worst and best parts of this experience - Karlis Berzins.

Contents

Declarations **3**

Abstract **4**

Acknowledgements **5**

1 Introduction **21**

1.1 Organic electronic materials for optoelectronics 21

1.2 Predicting absorption strength 22

1.3 Thesis objective 23

2 Theoretical background **27**

2.1 Electronic structure of organic semiconductors 27

2.2 Photocurrent generation in organic semiconductors 29

2.3 Morphology of organic semiconductors 31

2.4 Optical absorption of organic semiconductors 34

2.4.1 Quantifying Absorption Strength 34

2.4.2 Measuring Optical Properties 39

2.4.3 Coarse-Grained Model Studies of Optical Properties 39

2.5 Relating morphology to optical properties 42

2.5.1 Experimental studies 42

2.5.2 Quantum Chemistry Studies 43

2.5.3 Geometry Dependence in Coarse-Grained Exciton Models 44

2.6 Thesis objectives and overview 45

3 Methods **54**

3.1 Wavefunction based methods 54

3.1.1 The Hartree-Fock method 54

3.1.2 Configuration interaction singles 55

3.2 Density functional theory 57

3.2.1 Ground state formalism 57

3.2.2 Time dependent formalism 58

3.2.3 Exchange-Correlation energy functionals 59

3.2.4 Basis sets 60

3.3 Coarse grained methods for excited state properties 61

3.3.1 Wannier function basis configuration interaction singles 61

3.3.2 Frenkel exciton model 63

4 Conformation dependent optical properties studied using TDDFT **67**

4.1 Introduction 67

4.2 Oligomer length and conformation dependent absorption of polythiophene . . . 69

4.2.1 Experimental context . . . 69

4.2.2 Calculations . . . 70

4.3 Absorption strength of non-fullerene acceptors IDTBR and IDFBR . . . 76

4.3.1 Experimental observations of optical absorption . . . 76

4.3.2 Calculations of optical absorption by IDTBR and IDFBR using TDDFT 78

4.4 Discussion and conclusions . . . 84

5 Calculating optical properties using W-CIS 89

5.1 Introduction . . . 89

5.2 Computational Implementation . . . 90

5.2.1 Method overview . . . 91

5.2.2 Obtaining maximally localised Wannier functions . . . 92

5.2.3 Wannier function integrals . . . 97

5.2.4 Calculating optical properties . . . 100

5.3 Ab initio parameters of polyacetylene . . . 100

5.3.1 Transfer integrals . . . 101

5.3.2 Coulomb interaction . . . 102

5.3.3 Transition dipole moments . . . 103

5.4 Optical properties of oligoacetylenes . . . 104

5.4.1 Optical absorption spectra . . . 104

5.4.2 Convergence of optical properties . . . 105

5.4.3 Method comparison . . . 106

5.5 Exciton characterisation . . . 109

5.6 Discussion and conclusions . . . 111

6 Conformation dependent optical properties studied using W-CIS 115

6.1 Introduction . . . 115

6.2 Bond length alternation in oligoacetylenes . . . 117

6.2.1 Parameterisation . . . 118

6.2.2 Oligomer optical spectra . . . 120

6.2.3 Transition energies . . . 122

6.2.4 Transition dipole strengths . . . 125

6.3 Dihedral angles in oligothiophenes . . . 127

6.3.1 Parameterisation . . . 128

6.3.2 Oligomer optical spectra . . . 130

6.3.3 Transition energies . . . 133

6.3.4 Transition dipole moments . . . 136

6.4 Discussion and conclusions . . . 138

7 Conclusions 142

7.1 Summary of thesis achievements . . . 142

7.2 Applications and future work . . . 144

List of Tables

5.1 Descriptions of the input arguments used in the Wannier function integration code, these correspond to the yellow boxes in figure 5.3. 99

5.2 W-CIS parameters for different single particle separations s: on-site energies ϵ^c, ϵ^v, transfer integrals $t^c(s)$, $t^v(s)$, direct and exchange Coulomb integrals $U^d(s)$, $U^x(s)$ and the components of the intermonomer transition dipole moment $\mu_x(s)$, $\mu_y(s)$, $\mu_z(s)$. 101

6.1 Bond lengths (d_{single}, d_{double}) and bond length alternation (BLA) of the acetylene structures studied in this chapter. 118

List of Figures

2.1 Combination of (a) sp^3, (b) sp^2 and (c) sp hybridised carbon atoms yielding ethane, ethene and ethyne, respectively. Taken from [1]. 28

2.2 Energy level diagram showing the formation of bonding and anti-bonding σ- and π-orbitals between the two carbon atoms in ethene (the carbon-hydrogen bond orbitals are omitted). Taken from [1]. 29

2.3 Electronic states in the photocurrent generation mechanism in an organic photovoltaic device, taken from [3]. 30

2.4 (a) The dihedral angle between the two aromatic units is measured between the plane defined by the points A, B and C (blue) and the plane defined by B, C and D (orange), whereas the bond angle is defined between the bond direction vectors $\vec{u}$ between the neighbouring units. (b) Typical conformations of a 100-mer generated by Monte Carlo Simulations [28], the conformational classes are denoted by I: random coil, II: molten globule, III: toroid, IV: rod, V: defect-coil and VI: defect-cylinder. 32

2.5 According to the Franck–Condon principle the absorption of a photon causes a transition from the ground state to the electronic excited state at Q_0, followed by a vibrational transition to the equilibrium state at Q_0'. The subsequent emission of a photon returns the system to the electronic ground state, and finally, a vibrational relaxation process reverts the system back to its original ground state at the equilibrium position Q_0. Figure reproduced from Fox [37]. 37

4.1 (a) Extinction coefficient as a function of energy of the incoming light for regio-regular and regio-random P3HT thin films, experimental data provided by Mariano Campoy-Quiles.[8][9] 70

4.2 Orientation along the Cartesian axes (red - x, green - y, blue - z) of the optimised structures of trans- and cis-pentathiophene. Calculation details: geometry optimisation in DFT (CAM-B3LYP/cc-pVDZ). 71

4.3 Transition energies from the ground state to the lowest singlet state measured experimentally for regio-regular 3HT oligomers in chloroform and calculated for trans-oligothiophenes in vacuum (for BLYP, B3LYP and CAM-B3LYP) and in chloroform (for CAM-B3LYP). Calculation details: geometry optimisation using DFT (cc-pVDZ) and excited states using TDDFT (cc-pVDZ). 72

4.4 (a) Total and (b) specific oscillator strength of the first excitation for trans-oligothiophenes calculated using different exchange-correlation functionals. Calculation details: geometry optimisation using DFT (cc-pVDZ) and excited states using TDDFT (cc-pVDZ). (c) Mass attenuation coefficient μ_a and molar attenuation coefficient ϵ for lowest energy transition measured experimentally for 3HT oligomers [10]. 73

4.5 (a) Oscillator strength spectra for different lengths of trans- and cis-oligothiophenes. Calculation details: geometry optimisation using DFT (CAM-B3LYP/cc-pVDZ) and excited states using TDDFT (CAM-B3LYP/cc-pVDZ). 74

4.6 Chemical structure of IDFBR and IDTBR. In the case of O-IDFBR and O-IDTBR whose experimental data is presented in this chapter, R represents n-octyl side chains. 76

4.7 Experimentally measured optical spectra of O-IDTBR (blue) and O-IDFBR (green), in solution (solid lines) and solid state (dashed lines). 77

4.8 Energy barriers between different IDTBR conformers, taken from DFT geometry optimisation calculations using the ωB97XD functional and cc-pVDZ basis set. . 78

4.9 Energy barriers between different IDFBR conformers, taken from DFT geometry optimisation calculations using the ωB97XD functional and cc-pVDZ basis set. . 79

4.10 Comparing planarity between IDTBR and IDFBR. 80

4.11 Frontier molecular orbitals of freely optimised IDTBR and IDFBR, as well as planarised IDFBR. 81

4.12 HOMO and LUMO energies and the resulting electronic band gaps (E_g) of freely optimised IDTBR and IDFBR, as well as planarised IDFBR. 81

4.13 (a) Optical spectra of optimised IDTBR and IDFBR, calculated using TDDFT (CAM-B3LYP functional and cc-pVDZ basis states). (b) 83

4.14 Transition energy (E_1), transition dipole strength ($|\mu_1|^2$) and oscillator strength (f_1) of the first excited state of freely optimised IDTBR, IDFBR, as well as planarised IDFBR, calculated using TDDFT (CAM-B3LYP functional and cc-pVDZ basis states). 84

5.1 (a) DFT, Hartree-Fock and WF bands of polyacetylene, (b) maximally localized Wannier functions of monomer LUMO orbital (W^c) and HOMO orbital (W^v) for polyacetylene. 95

5.2 Visualisation of the commands used in the script that is used to perform the wannierisation step of the modelling framework presented in this chapter. The white boxes contain the specific executable used in each step, as well as which software package it is from. The yellow boxes show the input files, and the purple boxes show the final output files containing all the necessary data for the next steps. 96

5.3 Visualisation of the commands used in the script that performs integration between Wannier functions. The white boxes contain the names of the functions defined in the C++ code, the yellow boxes show the input parameters that are defined in the input files, and the purple box shows the final result variable which is written in the output file. 98

5.4 Absolute values of the electron (top) and hole (bottom) transfer integrals as a function of particle separation s. 102

5.5 (top) Direct Coulomb interaction energies calculated as WF integrals, a fitted Mataga-type decay and the Coulomb interaction energy of two point charges, and (bottom) exchange Coulomb interaction energies calculated as WF integrals and a fitted exponential decay. 103

5.6 a) Intermonomer transition dipole moment magnitudes as a function of electron-hole separation s and the absolute values of its components parallel (z) and perpendicular (y) to the long axis and b) a diagram showing a polyacetylene fragment with 5 units with respect to the Cartesian axes. 104

5.7 Optical absorption spectra showing the W-CIS calculated oscillator strength broadened with a Gaussian function of width $\sigma = 0.25\ eV$ as a function of transition energy for different length oligoacetylenes. 105

5.8 Transition energy (E_1), specific transition dipole strength ($|\boldsymbol{\mu}_1|^2/N$) and specific oscillator strength (f_1/N) of the first transition as a function of number of monomers calculated by W-CIS using a different nearest neighbour interaction cut-off indicated by the maximum electron hole separation s_{max}. 106

5.9 Transition energy, specific transition dipole strength and specific oscillator strength of different length oligoacetylenes calculated using W-CIS (purple) and CIS (blue). 107

5.10 Transition energy, specific transition dipole strength and specific oscillator strength of different length oligoacetylenes calculated by W-CIS (purple) and FE (black). 108

5.11 Electron charge density relative to the hole, which is fixed at the centre of an oligoacetylene with 31 C_2H_2 units. 110

5.12 Exciton binding energy of different length oligoacetylenes calculated by W-CIS. . 110

5.13 a) Contributions of exciton basis states with different electron-hole separations (s) to the first excited state of different length oligoacetylenes. b) Exciton radius of different length oligoacetylenes calculated by W-CIS, the value converges to $r_{eh} = 2.1$ at polymer limit. 111

6.1 Repeat units of (left) polyacetylene showing the double bond length d_{double} and single bond length d_{single} used to calculate BLA and (right) polythiophene showing the two planes used to measure the dihedral angle. 117

6.2 a) HF bandstructure (green) of polyacetylene with a BLA of 0.02 Å and the WF bands (orange) corresponding to $W_i^v(\boldsymbol{r})$ and $W_i^c(\boldsymbol{r})$, which are plotted in b). . . 119

6.3 The energies of the valence and conduction band edges for polyacetylenes with different BLAs and associated polymer band gaps. 119

6.4 Optical absorption spectra showing the W-CIS calculated oscillator strengths broadened with a Gaussian function of width $\sigma = 0.25\ eV$ as a function of transition energy for 20-mer oligoacetylenes with different BLAs. 120

6.5 (a) Transition energy E_1, (b) transition dipole strength $|\boldsymbol{\mu}_1|$ and (c) oscillator strength f_1 of the first excited state of a 20-mer oligoacetylene as a function of BLA calculated using the W-CIS method. 121

6.6 Transition energy (E_1), specific transition dipole strength ($|\boldsymbol{\mu}_1|^2/N$) and specific oscillator strength (f_1/N) of the first transition of an oligoacetylene as a function of number of monomers. 122

6.7 (a) HOMO and LUMO energies of 20-mer oligoacetylenes with different BLAs and their associated oligomer band gaps E_g and (b) the same band gaps plotted alongside the exciton binding energy of the oligomers. 123

6.8 (a) On-site energies ϵ^v, ϵ^c of the WFs W^v, W^c representing the HOMO and LUMO of an acetylene unit and their difference $\Delta\epsilon$ and (b) the transfer integrals t^v, t^c of W^v and W^c as a function of particle separation. 124

6.9 a) Direct and exchange Coulomb integral terms $U^d(s)$, $U^x(s)$ for polyacetylene with different BLAs as a function of electron-hole separation s and b) the value of the diagonal Coulomb term of the W-CIS Hamiltonian $2U^x(s) - U^d(s)$. 125

6.10 Intermonomer transition dipole moment magnitudes $|\boldsymbol{\mu}(s)|$ as a function of electron-hole separation s for polyacetylenes with different BLAs. 126

6.11 a) Contributions of exciton basis states with different electron-hole separations (s) to the first excited state of 20-mer oligoacetylenes with different BLAs and b) exciton radius as a function of BLA. 127

6.12 a) DFT band structure (black) and conduction WF band (blue) of polythiophene with a 0° dihedral angle, b) the same polymer's HF band structure (green) with highlighted LUMO bands (pink) and valence and conduction WF bands (orange) and the polymer band gap E_g^∞ and c) the HOMO (bottom) and LUMO (top) WFs associated with the wannierised bands. 129

6.13 The energies of the valence and conduction band edges for polythiophenes with different dihedral angles and associated polymer band gaps. 130

6.14 Optical absorption spectra showing the W-CIS calculated oscillator strength as a function of transition energy for oligothiophenes with different dihedral angles. 131

6.15 (a) Transition energy, (b) transition dipole strength and (c) oscillator strength of the first excited state of a 10-mer oligothiophene as a function of dihedral angle. 132

6.16 Transition energy (E_1), specific transition dipole strength ($|\boldsymbol{\mu}_1|^2/N$) and specific oscillator strength (f_1/N) of the first transition of an oligothiophenes as a function of number of monomers. 133

6.17 (a) HOMO and LUMO energies of 20-mer oligothiophenes with different dihedral angles and their associated oligomer band gaps E_g and (b) the same band gaps plotted alongside the exciton binding energy of the oligomers. 134

6.18 (a) On-site energies of the WFs representing the HOMO (W^v) and LUMO (W^c) of thiophene and their difference $\Delta\epsilon$ and (b) the transfer integrals of W^v and W^c as a function of particle separation. 135

6.19 a) Direct and exchange Coulomb integral terms $U^d(s)$, $U^x(s)$ for polythiophene with different dihedral angles as a function of electron-hole separation s and b) the value of the diagonal Coulomb term of the W-CIS Hamiltonian $2U^x(s) - U^d(s)$. 136

6.20 Intermonomer transition dipole moment magnitudes as a function of electron-hole separation s for thiophenes with different dihedral angles. 137

6.21 a) Contributions of exciton basis states with different electron-hole separations (s) to the first excited state of 20-mer oligothiophenes with different dihedral angles and b) exciton radius as a function of dihedral angle. 138

Chapter 1

Introduction

1.1 Organic electronic materials for optoelectronics

Macromolecular electronic materials such as conjugated polymers have attracted great interest for optoelectronic applications, such as light emitting devices, solar cells and photodetectors, partly because of the ability to tune the optical absorption and emission spectra via chemical design. In addition, the relatively narrow transition bandwidth and the fact that in many, if not most, systems the lowest electronic transition is optically allowed lead to a relatively sharp absorption edge which is useful in e.g. light emission applications.

Whilst many studies have addressed the development and validation of methods for prediction of transition energies, relatively few have addressed prediction of transition strength. Yet transition strength, quantified as oscillator strength, is important in controlling the luminescent efficiency of LEDs, the photocurrent of solar cells and photodetectors and the optimum layer structure for any such device. One of the challenging aspects of studying the properties of polymers is that they are amorphous or at best semicrystalline, and their morphology is determined by a complex interplay between the material's chemical structure and processing conditions. Therefore, a central question in the field of organic semiconductors is how processing conditions control the morphology, and how the morphology in turn controls the properties of the material. This means that to understand and predict the optical properties of macromolecular

materials we need computationally efficient models that account for the shape and chemical structure dependence of optical transitions in molecules of some tens or hundreds of atoms, which is challenging to model due to effects at different length scales.

The morphology of conjugated polymers has been widely studied using statistical mechanics models [1][2][3][4][5], and some of these studies also analyse the effects of the material's morphology on its functional properties. However, much of the work has focused on the effect of microstructure on the material's charge transport[4][6][7][8], or - if optical properties are considered - the studies focused on understanding the effect of polymer conformation on the transition energies [9][10] or vibronic structure [11][12][13][14][15][16] of the optical spectra. The majority of the published optical spectra of conjugated polymers are normalised, and only very few studies consider the absolute absorption strength, such as the work by Vezie et al. [17].

1.2 Predicting absorption strength

The key quantity determining the optical absorption strength is the set of oscillator strengths of the excited state transitions of a molecule or molecular segment, which directly control the absorption strength of the molecular material. At a very simple level transition energy and oscillator strength can be estimated from the energies and symmetries of the highest occupied and lowest unoccupied molecular orbital as obtained from a calculation of the ground state of the system. More reliable estimates require a calculation of the excited states of the system, usually in the basis of the molecular orbitals and taking into account the distribution of the transition oscillator strength over multiple initial and final vibrational modes of the system. The state space for such calculations soon becomes huge and calculations correspondingly expensive, thus methods typically involve a compromise between accuracy and scale.

For reference, a conjugated segment of a polymer or oligomer could contain a few hundred carbon and other atoms in the conjugated backbone. To investigate the effect of molecular conformations explicitly we need to be able to compare the optical response of such segments in many different conformations, and this is very computationally expensive for commonly used

ab initio methods such as time dependent density functional theory (TDDFT). To access larger systems, therefore, we need some form of coarse-graining whereby the properties of individual monomers or molecular sub-units, constructed from an atomistic description of the monomer, are used to build a Hamiltonian that embodies a description of the excited states of a molecule or an oligomer. One relatively simple approach is to use a Frenkel exciton model where excited states of the system are found using a tight-binding Hamiltonian in a basis of singly excited states of the monomers. However, challenges to such an approach are finding a way to include effects of the chemical structure and relative geometry of the building blocks, and incorporating charge transfer character of the excited states.

A better understanding of the relationship between the morphology of organic semiconductors and their optical properties is necessary to design and develop higher performing solar cells. A lot of studies in this area [9][10][11][17][18] complement experimental studies with computational methods such as TDDFT that are too computationally expensive to access the length scales required to fully explain the observed structure-property relationships. Another group of studies [12][13][14][15][16][19][20][21][22] use coarse-grained models to examine the structure-property relationships at longer lengths scales, but these use approximations to the electron-hole interactions that do not accurately reproduce the experimentally observed trends in absorption strength as a function of molecular structure.

1.3 Thesis objective

My thesis will focus on contributing to this particular gap of knowledge on the property-structure relationship of conjugated polymers - understanding how conformational changes of a polymer affect the absorption strength, and thus the efficiency of an organic solar cell. I propose that in order to further our understanding in this area it is necessary to implement a coarse-grained model with a more rigorous treatment of electron-hole interactions. In this thesis I apply a coarse-grained approach - configuration interaction singles in a basis of Wannier functions - to study the conformation dependent optical absorption properties of conjugated

polymers. The key objective of this thesis is developing a modelling framework that can be used to obtain the model parameters from *ab initio* calculations and illustrate how this enables addressing questions around structure-property relationships of π-conjugated materials and ultimately aid in the design of new high absorbing materials for organic solar cells.

Bibliography

[1] Margherita Moreno, Mose Casalegno, Guido Raos, Stefano V. Meille, and Riccardo Po. Molecular modeling of crystalline alkylthiophene oligomers and polymers. *J Phys Chem B*, 114(4), 2010.

[2] K. N. Schwarz, T. W. Kee, and D. M. Huang. Coarse-grained simulations of the solution-phase self-assembly of poly(3-hexylthiophene) nanostructures. *Nanoscale*, 5(5):2017–27, 2013.

[3] D. M. Huang, R. Faller, K. Do, and A. J. Moule. Coarse-grained computer simulations of polymer/fullerene bulk heterojunctions for organic photovoltaic applications. *J. Chem. Theory Comput.*, 6(2), 2010.

[4] P. Prins, F. C. Grozema, F. Galbrecht, U. Scherf, and L. D. A. Siebbeles. Charge transport along coiled conjugated polymer chains. *J. Phys. Chem. C*, 111(29), 2007.

[5] N. E. Jackson, K. L. Kohlstedt, B. M. Savoie, M. Olvera de la Cruz, G. C. Schatz, L. X. Chen, and M. A. Ratner. Conformational order in aggregates of conjugated polymers. *J Am Chem Soc*, 137(19):6254–62, 2015.

[6] D. Niedzialek, V. Lemaur, D. Dudenko, J. Shu, M. R. Hansen, J. W. Andreasen, W. Pisula, K. Mullen, J. Cornil, and D. Beljonne. Probing the relation between charge transport and supramolecular organization down to angstrom resolution in a benzothiadiazole-cyclopentadithiophene copolymer. *Adv Mater*, 25(13):1939–47, 2013.

[7] Carl Poelking, Kostas Daoulas, Alessandro Troisi, and Denis Andrienko. *Morphology and*

Charge Transport in P3HT: A Theorist's Perspective, volume 265 of *Advances in Polymer Science*, pages 139–180. Springer Berlin Heidelberg, 2014.

[8] Scott Himmelberger and Alberto Salleo. Engineering semiconducting polymers for efficient charge transport. *MRS Communications*, 5(03):383–395, 2015.

[9] J. Sjoqvist, M. Linares, M. Lindgren, and P. Norman. Molecular dynamics effects on luminescence properties of oligothiophene derivatives: a molecular mechanics-response theory study based on the CHARMM force field and density functional theory. *Phys Chem Chem Phys*, 13(39):17532–42, 2011.

[10] Jonas Sjöqvist, Mathieu Linares, Kurt V. Mikkelsen, and Patrick Norman. QM/MM-MD simulations of conjugated polyelectrolytes: A study of luminescent conjugated oligothiophenes for use as biophysical probes. *The Journal of Physical Chemistry A*, 118(19):3419–3428, April 2014.

[11] A. V. Gavrilenko, T. D. Matos, C. E. Bonner, S.-S. Sun, C. Zhang, and V. I. Gavrilenko. Optical absorption of poly(thiophene vinylene) conjugated polymers. Experiment and first principle theory. *J. Phys. Chem. C*, 112(21), 2008.

[12] F. C. Spano. The spectral signatures of Frenkel polarons in H- and J-aggregates. *Accounts of Chemical Research*, 43(3):429–439, 2010.

[13] H. Yamagata and F. C. Spano. Interplay between intrachain and interchain interactions in semiconducting polymer assemblies: the HJ-aggregate model. *J Chem Phys*, 136(18):184901, 2012.

[14] F. C. Spano and H. Yamagata. Vibronic coupling in J-aggregates and beyond: a direct means of determining the exciton coherence length from the photoluminescence spectrum. *J Phys Chem B*, 115(18):5133–43, 2011.

[15] H. Yamagata, N. J. Hestand, F. C. Spano, A. Kohler, C. Scharsich, S. T. Hoffmann, and H. Bassler. The red-phase of poly[2-methoxy-5-(2-ethylhexyloxy)-1,4-phenylenevinylene] (MEH-PPV): a disordered HJ-aggregate. *J Chem Phys*, 139(11):114903, 2013.

[16] N. J. Hestand and F. C. Spano. The effect of chain bending on the photophysical properties of conjugated polymers. *J Phys Chem B*, 118(28):8352–63, 2014.

[17] M. S. Vezie, S. Few, I. Meager, G. Pieridou, B. Dorling, R. S. Ashraf, A. R. Goni, H. Bronstein, I. McCulloch, S. C. Hayes, M. Campoy-Quiles, and J. Nelson. Exploring the origin of high optical absorption in conjugated polymers. *Nat Mater*, 2016.

[18] J. L. Bredas, J. P. Calbert, D. A. da Silva Filho, and J. Cornil. Organic semiconductors: A theoretical characterization of the basic parameters governing charge transport. *Proc Natl Acad Sci USA*, 99(9), 2002.

[19] Kenneth S. Schweizer. Configurational dependence of the optical properties of pi-conjugated polymers. I. Strong disorder limit. *The Journal of Chemical Physics*, 85(7):4181, 1986.

[20] G. Rossi, R. R. Chance, and R. Silbey. Conformational disorder in conjugated polymers. *The Journal of Chemical Physics*, 90(12):7594, 1989.

[21] Vladimir Dobrosavljević and Richard M. Stratt. Role of conformational disorder in the electronic structure of conjugated polymers: Substituted polydiacetylenes. *Physical Review B*, 35(6):2781–2794, 1987.

[22] M. Marcus, O. R. Tozer, and W. Barford. Theory of optical transitions in conjugated polymers. II. Real systems. *J Chem Phys*, 141(16):164102, 2014.

Chapter 2

Theoretical background

In this chapter I review the relevant theoretical concepts and background literature supporting the research goals of this thesis. Firstly, I introduce the basic electronic structure concepts that are used to describe the optical properties of conjugated polymers. I then give a short review of the mechanism for photocurrent generation in these materials. Next, I provide an overview of the importance of morphology when studying conjugated polymers, as well as a short review of how optical properties are quantified, measured and modelled using different approaches. Finally, I bring together literature studying the structure-property relationship in polymers and small molecules using a variety of methods, and state what the goal of this thesis is in the context of these studies.

2.1 Electronic structure of organic semiconductors

Before reviewing different approaches of calculating the optical properties of conjugated polymers (CPs), we need to take a step back and look at the electronic structure of these materials. Organic semiconductors are based on carbon, which in its ground state has six electrons. In atomic carbon two of the electrons are in a 1s orbital, two are in a 2s orbital and the remaining two occupy two of the three 2p orbitals. However, when carbon is not in its elementary atomic form, one of the electrons from the 2s orbital is promoted to the third unoccupied 2p orbital.

When this happens, the singly occupied 2s orbital mixes with one or more 2p orbitals forming hybrid orbitals. When the 2s orbital mixes with all three 2p orbitals, the resulting hybrid orbitals are referred to as $2sp^3$ orbitals. This is what happens when the molecule ethane is formed, where one of the $2sp^3$ hybrid orbitals forms a σ-bond with a $2sp^3$ orbital of a second carbon atom and the remaining three $2sp^3$ orbitals form σ-bonds with the 1s orbital of a hydrogen atom (figure 2.1a). In the case of ethene, the 2s orbital mixes with two of the 2p orbitals forming three $2sp^2$ hybrid orbitals, which form σ-bond with one $2sp^2$ orbital of another carbon atom and two hydrogen atoms. The third 2p orbital forms a π-bond with the 2p orbital of the second carbon atom (figure 2.1b). Similarly, in the case of ethyne, often referred to as acetylene, the 2s orbital mixes with one of the 2p orbitals creating two 2sp hybrid orbitals, which form σ-bonds with the 2sp orbital of carbon and the 1s orbital of hydrogen, and the two remaining 2p orbitals form two π-bonds. The σ- and π-bonds described here are usually referred to as molecular orbitals.

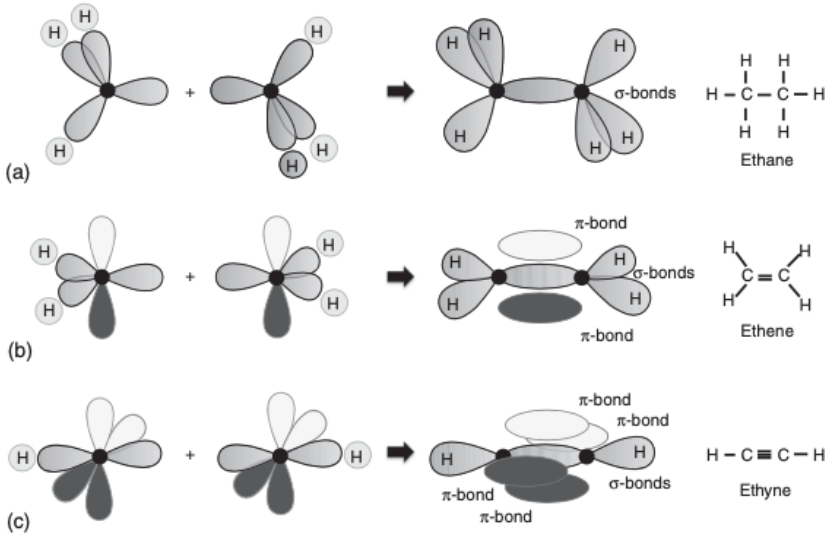

Figure 2.1: Combination of (a) sp^3, (b) sp^2 and (c) sp hybridised carbon atoms yielding ethane, ethene and ethyne, respectively. Taken from [1].

In order to study the optical properties of these materials, we need to find out what energies these molecular orbitals have. There are many ways to calculate the energies of molecular orbitals at different levels of accuracy, some of these will be reviewed in chapter 3. Figure 2.2 contains a qualitative picture of the energy levels in ethene showing the atomic orbitals 1s, $2sp^2$ and 2p of both carbon atoms and the corresponding bonding (σ, π) and anti-bonding (σ^*,

π^*) molecular orbitals approximated by linear combination of atomic orbitals (LCAO). Filling up the molecular orbitals with the eight electrons from the carbon-carbon bonds starting from the lowest energy orbitals, we find that the highest occupied molecular orbital (HOMO) is the bonding π-orbital and that the lowest unoccupied molecular orbital (LUMO) is the anti-bonding π^*-orbital. The HOMO and LUMO, together often referred to as the frontier orbitals, play a crucial role in the optical processes of π-conjugated materials due to the relatively small energy gap between the π and π^* molecular orbitals. This allows $\pi \rightarrow \pi^*$ transitions to occur by absorbing light in the visible range of the spectrum and thus making these materials well suited to applications based on light absorption and emission.

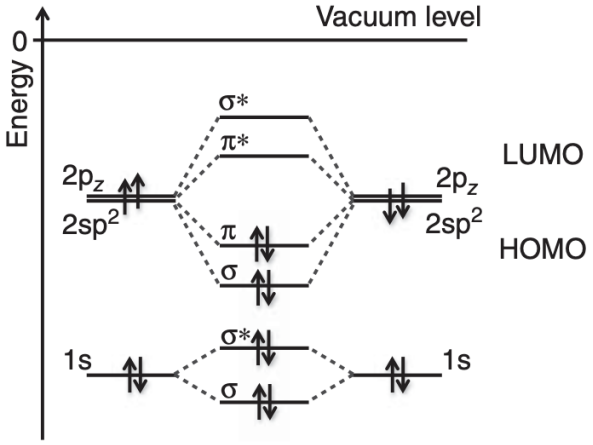

Figure 2.2: Energy level diagram showing the formation of bonding and anti-bonding σ- and π-orbitals between the two carbon atoms in ethene (the carbon-hydrogen bond orbitals are omitted). Taken from [1].

2.2 Photocurrent generation in organic semiconductors

The mechanism for photocurrent generation in organic photovoltaic (OPV) devices is more complex than in inorganic solar cells, as the low dielectric permittivity of organic semiconductors causes a large Coulomb barrier for the photoexcited states to dissociate into separate electrons and holes. To address this most OPV devices use a heterojunction of two different materials with offset energy levels, so that the charge-transfer (CT) state between the donor material and the acceptor material is energetically more favourable than an exciton state localised on either

the donor or the acceptor material. The photocurrent generation mechanism is illustrated in figure 2.3 and can be generally separated into the following steps[2][3]:

- the absorption of a photon and subsequent generation of an exciton - a bound localised electron-hole pair - typically in the donor material (left in figure 2.3),
- the transport or diffusion of this exciton to an interface between the donor and acceptor materials,
- the transition from a localised exciton state to an excited charge-transfer state based on both the donor and acceptor materials, typically the electron from the donor LUMO transfers to the acceptor LUMO (centre of figure 2.3),
- thermal and electronic relaxation of the charge-transfer state (top centre in figure 2.3),
- and, finally, the transition from the charge-transfer state to a separated charge pair, with the electron in the acceptor material and the hole in the donor material (right in figure 2.3).

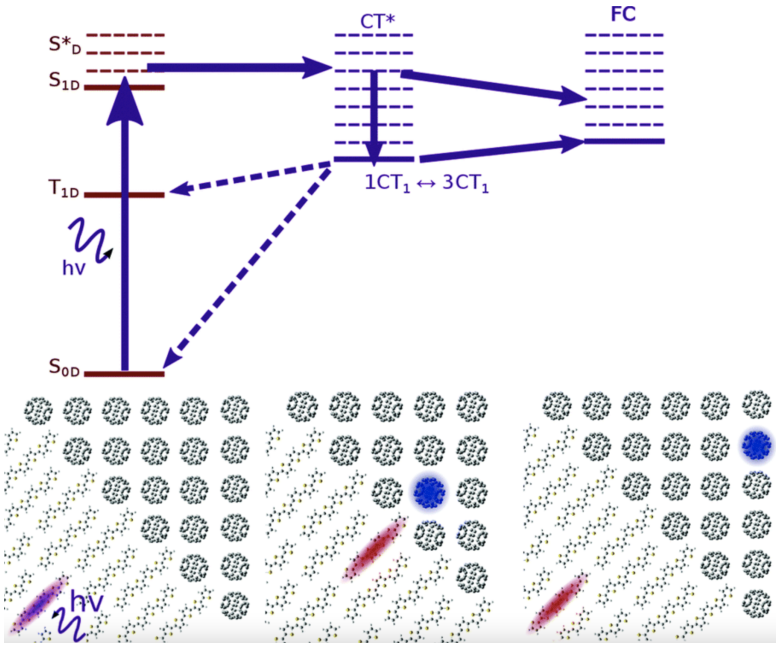

Figure 2.3: Electronic states in the photocurrent generation mechanism in an organic photovoltaic device, taken from [3].

The focus of this thesis is to better understand the first step - the absorption strength of organic semiconductors. However, it is worth considering it in the context of the photocurrent generation process, as studies focusing on understanding exciton diffusion and charge separation use similar approaches to those studying the photoexcitation step. A lot of work has gone into developing model Hamiltonians to characterise the low energy excitons that are involved in the photocurrent generation in conjugated polymers[4][5][6][7][8][9][10][11], and many of these models have been extended to incorporate the effects of conformational disorder on the exciton delocalisation along a polymer chain[12][13][14][15][16][17]. Model Hamiltonians have also been developed and used to study the exciton delocalisation in molecular crystals[18][19][20], as well as the effect of incorporating interchain interactions when modelling semicrystalline polymers[21][22]. Furthermore, there has been a significant amount of work on modelling the optical absorption and photoluminescence spectra of conjugated polymers in order to link spectral signatures to conformational disorder[12][14][16][17][22][23][24] and coupling to vibrational modes[10][21][22][24][25][26][27]. The different types of model Hamiltonians used in the studies referenced above are described in more detail in section 2.4.3, and section 2.5.3 gives some detail on how conformational disorder and aggregation is incorporated into these model Hamiltonian approaches.

2.3 Morphology of organic semiconductors

The photoactive layer of an organic solar cell can exhibit very complicated morphologies, as it usually consists of a blend of different conjugated materials and additives. This thesis is limited to describing the properties of single polymer or small molecules phases without any additives. There are different length scales to consider when discussing the structure, or morphology, of π-conjugated materials. I will divide all the quantities describing the morphology of a polymer chain into two length scales: molecular scale and polymer chain scale.

1. Molecular scale: coplanarity and colinearity described by dihedral and bond angles (figure 2.4a) between successive subunits in a monomer or between monomers. These are affected

by the molecular structure of the backbone, as well as the side-chains.

2. Polymer chain scale: different arrangements of dihedral and bond angles give rise to different conformations of a polymer chain or a group of chains. The final structures can be crystalline, semi-crystalline or amorphous, which can further be classified into conformational classes, such as rigid rod, toroid, globule or random coil (figure 2.4b). Some quantities of interest at this length scale are the radius of gyration and end-to-end distance of a polymer chain, as well as persistence length, which will be discussed in more detail in further sections. Additionally, the nature of interchain interactions is important at this length scale, such as π-stacking and hydrogen bonding.

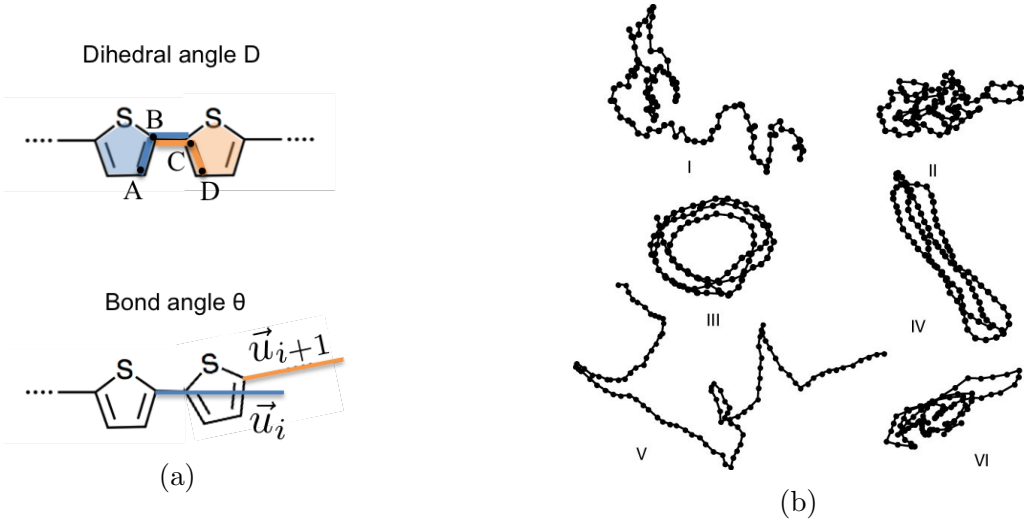

(a) (b)

Figure 2.4: (a) The dihedral angle between the two aromatic units is measured between the plane defined by the points A, B and C (blue) and the plane defined by B, C and D (orange), whereas the bond angle is defined between the bond direction vectors $\vec{u}$ between the neighbouring units. (b) Typical conformations of a 100-mer generated by Monte Carlo Simulations [28], the conformational classes are denoted by I: random coil, II: molten globule, III: toroid, IV: rod, V: defect-coil and VI: defect-cylinder.

Atomistic or coarse-grained Monte-Carlo (MC) or molecular dynamics (MD) can be used to study different amorphous conformations [29] and crystalline phases [30] of polymers and determine their persistence lengths [31]. Additionally, MD can also be used to obtain bond length, dihedral angle and bond angle probabilities and radial distributions [32]. A polymer's conformation can also be related to the structure at the molecular scale by either modelling the distribution of dihedral angles and studying how coiled the resulting polymer is [33], or by performing MD calculations on polymers with different molecular structures and classifying

the resulting structures into conformational classes, as was done by Jackson et al. [34]. They concluded that backbone linearity on the molecular scale is fundamental to obtaining ordered conformational structures, and consequently crystalline materials. However, they also note that this is highly dependent on the choice of sidechains, which were not considered in this study.

An important concept when discussing optical properties of CPs is a chromophore, which can be defined as the part of the polymer chain that absorbs or emits light. Marcus et al. [17] give a short review of different methods of quantifying the size of a chromophore, which is often equated to conjugation length. The conjugation length is defined in different ways by different authors, but is mostly related to the dihedral angles between neighbouring units. Earlier approaches interpreted the conjugation length as the length between two abrupt flips in a polymer chain by assigning a certain critical dihedral angle [35] or modelling the energetics of breaking particular hydrogen bonds that lead to rotations of single bonds, which in turn break the conjugation of the chain [13]. A different approach was taken by Chang et al. [23] who took the conjugation length to be a Gaussian variable and determined the centre and width of the distribution by fitting the theoretical spectra to experiment, where the theoretical spectra are obtained by adding the individual spectra of the conjugated units. A different treatment of these conformational features was taken in an early study by Rossi et al. [15] who determine the bond vectors $\hat{u}_i$ and normals to the subunit planes $\hat{\sigma}_i$ by considering the torsional potentials for different structures. They then define the bond correlation length λ_p, which is analogous to persistence length, in terms of the bond vector of the first unit in the chain $\hat{u}_0$ and the last unit $\hat{u}_L$ in a chain of L units

$$\left\langle \hat{u}_0 \cdot \hat{u}_L \right\rangle \sim e^{-L/\lambda_p}. \tag{2.1}$$

Additionally, they define the conformational conjugation length λ_c in terms of the unit vectors perpendicular to the planes of the subunits $\hat{\sigma}_0$, $\hat{\sigma}_1$,...,$\hat{\sigma}_L$

$$\left\langle (\hat{\sigma}_0 \cdot \hat{\sigma}_L)^2 \right\rangle - \left\langle (\hat{\sigma}_0 \cdot \hat{\sigma}_L)^2 \right\rangle_0 \sim e^{-L/\lambda_c}, \tag{2.2}$$

where $\left\langle (\hat{\sigma}_0 \cdot \hat{\sigma}_L)^2 \right\rangle_0$ is the value of $\left\langle (\hat{\sigma}_0 \cdot \hat{\sigma}_L)^2 \right\rangle$ when all the allowed motions of the bonds are unhindered. A more recent approach is described by Zhang et al. [36], where the persistence

length mean-square end-to-end distance of semi-flexible polymers is estimated both analytically and numerically from dihedral angle distributions. The main advantage of this approach is that it is very general and is thus not limited to only simple polymer structures and can treat complicated copolymers.

2.4 Optical absorption of organic semiconductors

I will first define the relevant quantities to describe optical absorption strength both on a molecular scale and a macroscopic scale, then briefly outline the main methods of experimentally measuring absorption spectra. Finally, I will outline quantum chemical methods used to calculate optical properties and review different coarse-grained models to capture the optical properties of conjugated polymers (CPs).

2.4.1 Quantifying Absorption Strength

The net transition rate between two states is given by Fermi's golden rule

$$\Gamma_{i\to f} = 2\pi|M_{if}|^2 g_i g_f (f_i - f_f)\delta(\omega_{0f} - \omega_{0i} - \omega_a), \tag{2.3}$$

where g_i and g_f are the degeneracies and f_i and f_f are the occupancies of the initial and final state, respectively, the difference between ω_{0i} and ω_{0f} is the resonant frequency of the transition from the initial to the final state and ω_a is the frequency of the absorbed photon. M_{if} is the matrix element of the transition and quantifies the quantum system's response to the perturbation of the incoming light wave

$$M_{if} = \langle\psi_f| H' |\psi_i\rangle , \tag{2.4}$$

where H' is the light-atom interaction Hamiltonian and ψ_i and ψ_f are the wavefunctions of the initial and final state. In the electric dipole approximation, it is assumed that the wavelength of

the incoming electromagnetic wave is much larger than the size of the system under investigation and the electric field $\vec{E} = \vec{E}_0 e^{-i\omega t}$ can be treated as constant in space, which allows expressing the perturbation caused by the incoming electromagnetic wave as

$$H' = -e\vec{r} \cdot \vec{E}_0. \tag{2.5}$$

Therefore, it can be shown that M_{if} is directly proportional to the transition dipole moment $\vec{\mu_{if}}$

$$M_{if} = \vec{E}_0 \cdot \langle \psi_f | - e\vec{r} | \psi_i \rangle = \vec{E}_0 \cdot \vec{\mu}_{if}. \tag{2.6}$$

Finally, the oscillator strength can be expressed in terms of $\vec{\mu}_{if}$ and the angular frequency of the transition ω_{if}, which for isotropically oriented molecules is given by [37]

$$f_{if} = \frac{2m\omega_{if}}{3\hbar} |\vec{\mu}_{if}|^2. \tag{2.7}$$

Clasically, discrete optical transitions can be modelled as the response to an electromagnetic field of Lorentz oscillators of resonant frequency equal to the transition frequencies. Then the relative permittivity can be expressed as a function of angular frequency ω according to

$$\epsilon_r(\omega) = 1 + \frac{Ne^2}{\epsilon_0 m_0} \sum_j \frac{f_j}{(\omega_{0j}^2 - \omega^2 - i\gamma_j \omega)}, \tag{2.8}$$

where N is the number of oscillators per unit volume, and f_j, ω_{0j} and γ_j are the oscillator strength, resonant frequency and damping coefficient of the j-th contributing transition. The relative permittivity is easily relatable to other optical properties of interest via the complex refractive index

$$\widetilde{n} = n + i\kappa = \sqrt{\epsilon_r}, \tag{2.9}$$

where n is the real part of the refractive index and κ is the extinction coefficient, which is directly related to the absorption coefficient

$$\alpha = \frac{4\pi}{\lambda} \kappa, \tag{2.10}$$

where λ is the wavelength of light in free space.

Many different quantities are used to measure optical absorption strength experimentally, including κ and α, as well as the optical density $O.D.$ and the decadic attenuation coefficient ϵ_d, which are related to the transmitted intensity of light according to

$$I = I_0 \times e^{\alpha z} = I_0 \times 10^{-O.D.} = I_0 \times 10^{-\epsilon_d c z}, \tag{2.11}$$

where I_0 is the initial light intensity, z is the distance travelled through the absorbing medium, and c is the concentration of the absorbing species usually given in units of $g.L^{-1}$ or $mol.L^{-1}$ to obtain the mass or molar attenuation coefficient, respectively.

Vibronic Features in Optical Spectra

In organic materials the transition between two electronic states is usually accompanied by a change in the nuclear motion. It is convenient to visualise vibronic transitions (involving electronic-vibrational coupling) with the aid of molecular configuration diagrams, which plot the energy of two electronic states with respect to a generalised coordinate Q associated with a local normal mode. In the case of a diatomic molecule, Q is simply the separation of the two atoms. The Franck–Condon principle as well as the resulting absorption and emission spectra are shown schematically in figure 2.5.

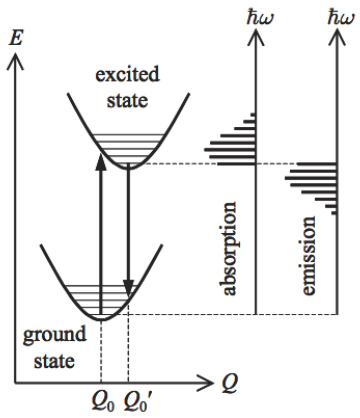

Figure 2.5: According to the Franck–Condon principle the absorption of a photon causes a transition from the ground state to the electronic excited state at Q_0, followed by a vibrational transition to the equilibrium state at Q_0'. The subsequent emission of a photon returns the system to the electronic ground state, and finally, a vibrational relaxation process reverts the system back to its original ground state at the equilibrium position Q_0. Figure reproduced from Fox [37].

The energy of the absorbed and emitted photons are given by

$$\hbar\omega_a = \hbar\omega_{vert} + n_e\hbar\Omega_e \tag{2.12}$$

and

$$\hbar\omega_e = \hbar\omega_{vert} - n_g\hbar\Omega_g, \tag{2.13}$$

where ω_{vert} is the vertical transition frequency, n_g and n_e are the number of excited vibrational quanta and Ω_g and Ω_e are the vibrational frequencies of the occupied ground and excited states, respectively. Different vibronic transitions are usually denoted by $n_g - n_e$, for example, 0-1 stands for the transition between the $n_g = 0$ vibrational level of the electronic ground state and the $n_e = 1$ vibrational level of the electronic excited state.

As the timescales of vibrational transitions are much longer than electronic transitions, it is possible to invoke the Born–Oppenheimer approximation and separate the electronic and vibrational contributions to the vibronic wavefunction according to

$$\psi_{i,n}(\vec{r}, Q) = \psi_i(\vec{r})\phi_n(Q - Q_0), \tag{2.14}$$

where i denotes the electronic level and n denotes the vibrational level occupied by the electron.

The relative heights of the absorption and emission peaks shown in figure 2.5 can be estimated by comparing the quantum transition rates $\Gamma_{i\to f}$ between different vibronic transitions, which are proportional to the square of the matrix element

$$|M_{if}|^2 \propto |\vec{\mu_{if}}|^2 \times |\langle \phi_{n_1} | \phi_{n_2} \rangle|^2. \tag{2.15}$$

The electronic component of the wavefunction gives rise to the transition dipole moment, which will be the same for all the vibronic transitions between the same electronic states. Hence, it is clear that the relative contribution of each vibronic transition to the optical spectra will mainly be determined by the square of the overlap integral of the initial and final vibrational wavefunctions, commonly referred to as the Franck–Condon factor

$$F_{n_1 n_2} \equiv |\langle \phi_{n_1} | \phi_{n_2} \rangle|^2. \tag{2.16}$$

By invoking several approximations, such as expressing the vibrational wavefunctions as simple harmonic oscillator states centered at the equilibrium coordinates Q_0 and Q_0', it is possible to obtain an analytical expression for $F_{n_1 n_2}$, generally referred to as the Huang-Rhys [38] parameter and is given by

$$S = \frac{(Q_0' - Q_0)^2}{2(\hbar/\mu\Omega)}, \tag{2.17}$$

where μ and Ω are the mass and angular frequency of the vibrational oscillator.

The relative strengths of vibronic transitions (especially 0-0 versus 0-1) and their dependence on disorder and aggregation has been explored in many studies [17][24][25][21]. However, in my work I focus on the effect of polymer conformation on the absorption strength of only the electronic transitions with the aim to study how changing a polymer's morphology changes the total area under an absorption peak instead of its vibronic features.

2.4.2 Measuring Optical Properties

As the focus of this project is on calculating the optical properties of polymers, only a few relevant experimental methods will be mentioned, a more thorough discussion can be found elsewhere[39]. The most common way of measuring the optical properties of conjugated materials is UV/visible transmission spectroscopy, which can be used to measure the absorption spectra for materials both in solution and in films. Typically, the measurement is recorded in terms of transmittance $T = I/I_0$, and the data can then be processed into different quantities of interest, as shown in equation (2.11). Another useful method is ellipsometry, which measures the change in polarisation of a reflected or transmitted light beam through a sample and is used to determine the complex dielectric function of the film.

2.4.3 Coarse-Grained Model Studies of Optical Properties

I will first review different methods of modelling the exciton delocalisation along a polymer chain due to intrachain interactions. These models can be expressed in a localised Frenkel exciton basis, an electron basis or an electron and hole basis. Then I will briefly review approaches to include interchain interactions, which affect the optical properties when two polymer chains or two chromophores on the same chain are close enough together.

Intrachain interactions

Early Frenkel Exciton (FE) Hamiltonians [5] consider only the ground state and one excited state of a given atom and express the energy of the system in terms of the energies of the localised FE (an electron promoted to the excited state from the ground state on the same atom) and their interaction energies. This is the general framework that FE Hamiltonians follow, but instead of atoms, the basis is mostly chosen to be monomer units. Barford and Marcus [11] use the following form of the Frenkel-Holstein Hamiltonian (the vibronic coupling

terms have been omitted below, as I focus only on the electronic transitions in this thesis)

$$H_{FH} = \sum_n \epsilon_n \hat{a}_n^\dagger \hat{a}_n + \sum_n J_{n,n+1}(\hat{a}_{n+1}^\dagger \hat{a}_n + \hat{a}_n^\dagger \hat{a}_{n+1}) \tag{2.18}$$

where $\hat{a}_n^\dagger$ ($\hat{a}_n$) creates (destroys) a Frenkel exciton on monomer n, ϵ_n is that monomer's transition energy and $J_{n,n+1}$ is the excitonic coupling between excitons on neighbouring units. The exciton transfer integral, which is composed of a through-bond (superexchange) J_{SE} and a through-space (dipole-dipole) J_{DD}, which can be expressed as

$$J_{SE} = -\frac{2\tilde{t}^2}{(\tilde{U} - \tilde{V} - 2\tilde{X}\delta_{SO})}, \tag{2.19}$$

where $\tilde{t}$ is the electron transfer integral, $\tilde{U}$ and $\tilde{V}$ are the intra and inter monomer Coulomb repulsion terms and $2\tilde{X}$ is the singlet-triplet interaction energy, and

$$J_{DD} = -\frac{2\mu_1^2 \delta_{SO}}{4\pi\epsilon_r\epsilon_0 d^3}, \tag{2.20}$$

where μ_1 is the transition dipole moment of the Frenkel exciton on a monomer and d is the repeat unit distance. Many studies use Hamiltonians similar to the one in (2.18) to study effects of disorder or different conformations [17][23][25][24] mainly by introducing a conformation dependence to the excitonic coupling. The FE model can also be used to estimate quantities relating to the chromophore size by treating J as a Gaussian variable with a temperature dependent variance and quantify the localisation of an exciton in terms of local exciton ground states[16], as introduced by Malyshev and Malyshev[7]. This is a more rigorous treatment of chromophore size than discussed previously, as it also takes into account the coupling strength between units not just their relative orientation, as was done by Rossi et al. [15].

Another group of effective Hamltonians used to study the optical properties of conjugated polymers are models that use π electron orbitals as their basis, including the Hückel method and its variations[13][15][14][12], as well as the Pariser-Parr-Pople (PPP) Hamiltonian[8][6]. The general form of these models can be given by the simplified Born-Oppenheimer Hamiltonian

for the π electrons

$$H_{BO}^{\pi} = \sum_i \epsilon_i N_i - \sum_{i\sigma} t_i (c_{i+1\sigma}^{\dagger} c_{i\sigma} + c_{i\sigma}^{\dagger} c_{i+1\sigma}) + U \sum_i N_{i\uparrow} N_{i\downarrow} + \frac{1}{2} \sum_{i \neq j} V_{ij} N_i N_j + V_{n-n}, \quad (2.21)$$

where $\epsilon_i N_i$ gives the energy for all electrons in the i-th orbital, t_i describes the transfer of an electron with spin σ from site to site, $U N_{i\uparrow} N_{i\downarrow}$ and $V_{ij} N_i N_j$ are the Coulumb interaction energies for electrons on the same and different sites, respectively, and lastly V_{n-n} is the screened nuclear-nuclear interaction. There are several studies on how to best capture the electron-electron interactions in terms of determining parameters [40] and what effect different electron-electron interactions have on the binding energy of the exciton [41].

Finally, I am also considering models that express the Hamiltonian in a basis of electrons and holes, often referred to as the two-state molecular orbital model. One major advantage of this approach is that it scales very well with system size, as there will always be only two particles in a basis function, as all the other electrons in the system are treated implicitly. Several studies [42][9][10][26] use this approach to study the properties of excitons in conjugated polymers, where the Hamiltonian is of the form

$$H_{eh} = \epsilon_e + \epsilon_h + \sum_i (t_e c_{i+1}^{\dagger} c_i + t_h d_{i+1}^{\dagger} d_i + h.c.) + \sum_{ij} V_{ij} c_i^{\dagger} c_i d_j^{\dagger} d_j, \quad (2.22)$$

where $c_i^{\dagger}$ and c_i ($d_i^{\dagger}$ and d_i) are the electron (hole) creation and annihilation operators, ϵ_e and ϵ_h are the energies of the electron and hole, t_e and t_h are the electron and hole hopping integrals, and V_{ij} is the interaction energy between an electron on the i-th monomer and a hole on the j-th monomer.

Interchain interactions

The effect of interchain interactions on the optical properties of CPs can be studied by considering the approaches used to model the excitonic interactions in molecular crystals. Early work includes the exciton model for molecule pairs by Kasha et al. [18] who looked at energies and transition strengths of pairs of molecules, and Rhodes [19] who also treated hypochromism

(increase in absorption strength) for pairs of emitters. These can also be seen as a basis for the FE models described in the beginning of this section, which are also used to study excitons in molecular crystals [20].

An interesting study to highlight was carried out by Yamagata and Spano [21] who use a Holstein-based Hamiltonian to study PDA and P3HT chains, focusing on both intrachain and interchain coupling of excitons. For polydiacetylene (PDA) they consider two semiconductor chains next to each other, where each chain is described by an effective particle-hole Hamiltonian, such as the one in equation (2.22), which includes the intrachain coupling (electron and hole hopping integrals), and the total Hamiltonian consists of the two effective Hamiltonians for each chains and a coupling term J_{inter}, which is the interchain excitonic coupling introduced in equation (2.18). For P3HT they use a Frenkel exciton Hamiltonian for both the intrachain part and the interchain coupling. Yamagata et al. [22] then complement the same model by including a disorder Hamiltonian term. The focus of both studies were the vibronic features in the resulting spectra and how varying the different coupling terms affect these.

2.5 Relating morphology to optical properties

2.5.1 Experimental studies

P3HT is one example of a polymer whose structure-property relationship has been widely studied. A good review on different approaches and studies on the optical spectra of P3HT in different morphologies is given by Tremel and Ludwigs[43]. A typical study involves observing the change in optical spectra of the polymer solution or film after changing the processing conditions, such as solvent or molecular weight[44][45]. In these studies the morphology is most often inferred from the vibronic features of the measured spectra, as the ratio of the vibronic peaks can be related to the excitonic coupling strength and exciton coherence length using Spano's model for polymer aggregation. A different approach is taken by Koch [46] who measured optical spectra of semicrystalline 3HT oligomers, whose structures were determined

using X-ray diffraction. The effect of morphology on the optical properties can also be studied using single molecule photoluminescence (PL) spectroscopy, which has been done by Thiessen et al. [47], who studied how the energetic disorder of chromophores in P3HT are related to the material's final morphology, as well as Baderschneider et al. [48] who studied the effect of conjugation length on the electron-phonon coupling. Finally, a very different study is performed by Chung et al. [49] who measure both the persistence length and absorption strength of poly(dialkylsilane)s experimentally and thus establish an empirical relationship between the two quantities, and they find that there is a saturation in absorption strength with persistence length.

2.5.2 Quantum Chemistry Studies

An early quantum mechanical study on the structural effects on the optical properties was done by Bredas et al. [50], who calculated the excitonic splitting energy for pairs of molecules in different arrangements and distances using semi-empirical Hartree-Fock. Although the study was performed for small molecules, it has implications for polymers in terms of the interchain interactions for different orientations and distances, as well as the coupling between neighbouring monomers in a disordered chain. Most modern studies use time-dependent DFT to study the effect of different polymer conformations. An uncommon approach was taken by Gavrilenko et al. [51] who treated poly(thiophene vinylene) (PTV) as a periodic structure and perform DFT calculations on two different unit cells of PTV, which have different π-stacking distances. They used the calculated spectra to interpret the appearance of a shoulder in experimental absorption spectra for differently treated samples. A more common approach is to combine a coarse-grained MD study with quantum mechanical calculations for the excited states on a certain number of snapshots of MD runs with different parameters.[52][53] Additionally, the effect of different conformations can be studied by considering oligomers with different structures on the molecular scale, as was done by Vezie et al. [54], who performed TDDFT calculations on oligomers for structures with alternating (trans) and non-alternating (cis) bond angles, which were used to represent two extremes cases of largest and smallest persistence

length, respectively. The analysis was complemented by estimates of persistence lengths for different polymers to aid the understanding of why some polymers exhibit higher absorption strength than others.

Many studies in the past have worked on extrapolating the transition energies of oligomers to the polymer limit. Some of these methods are reviewed by Torras et al. [55]. Although the more rigorous methods include saturation effects, they do not consider the effect of polymer conformation, in contrast to an early study by Rossi et al. [15] where they find a simple relationship between the band gap of the polymer and the torsional angles between successive units. However, these studies do not consider the transition probabilities.

A study by Schwarz et al. [31] consider the effect of nanofibre dimensions on the optical properties by using linear extrapolation for the transition energies and dipole strengths with respect to nanofibre width, which corresponds to the length of a P3HT chain before it folds over itself. A different approach is taken by Chang et al. [23] who calculate the distribution of conjugation lengths using torsional potentials and assign a transition energy and dipole moment to each chromophore using an exciton model, and then construct spectra as a sum of the spectra for the individual chromophores. The reverse effect of the same approach is applied by Kohler and Samuel [56] who also first find the excitation energies and transition dipole moments of different lengths of oligomers, but they then estimate the chain length distribution in their system by fitting the sums individual oligomer spectra to experimental absorption spectra.

2.5.3 Geometry Dependence in Coarse-Grained Exciton Models

One of the earlier approaches to include the effects of polymer conformation on the optical properties is described by Schweizer [12] who divided a polymer chain into submolecules due to conjugation breaks defined by a critical dihedral angle, and the properties of the polymer chain were expressed as the sum of properties of the submolecules.

The most common approach of introducing geometry dependence into the exciton models described in section 2.4.3 is by treating the exciton coupling integral or electron hopping integral

as a function of the dihedral angle between neighbouring units, as was done by Rossi et al. [15] who thus obtain a relationship for the band gap in terms of the conformational conjugation length, which is related to the torsional angles, as well as Dobrosavljević and Stratt [13] who discuss the significance of the average length of rod-like segments (between hydrogen bond breaks) and localisation length, where the latter is calculated by varying the coupling between neighbouring units due to changes in dihedral angles. This has some similarities with a more recent study by Marcus et al. [17] who treat the excitonic coupling in the Frenkel-Holstein model of equation (2.18) as a Gaussian variable and calculate the inverse participation ratio (IPR) of the disordered polymer, which they use as a measure of chromophore size.

Another type of conformational change to consider is polymer chain bending, which has been studied by Hestand and Spano [24] by introducing a finite bend angle between monomer units, which affects the excitonic coupling and also misaligns the transition dipole moments. Finally, aggregation is also a very important concept when discussing polymer morphologies, which has been studied extensively by Spano's group, [25][21][27] whose model is used a lot to relate the vibronic shape of experimental optical spectra to the nature of aggregation present in a sample [22].

2.6 Thesis objectives and overview

Designing organic solar cells with high power conversion efficiencies requires accurate modelling of complex multi-scale processes that are involved in photocurrent generation, as described in section 2.2. The focus of this thesis is on the first step in this process - the optical absorption of a photon generating an exciton. Specifically, the goal of this thesis is to gain insight into the morphology dependence of the optical absorption strength of the lowest energy excitations, which mainly contribute to the efficiency of the solar cell. As polymers display very complex amorphous or at best semi-crystalline morphologies, we have to consider length scales that are typically too large to be studied using *ab initio* methods and model Hamiltonians have to be employed instead.

Most studies in the literature that employ coarse-grained model Hamiltonians in the basis of Frenkel excitons or electrons and holes obtain their parameters by fitting to experimental optical spectra. My early calculations showed that many nearest neighbour interactions had to be included in the chosen model Hamiltonian in order to reproduce the superlinear trend of transition dipole strength with polymer chain length, as will be discussed in more detail in section 5.4.2 and is illustrated in figure 5.8. This meant that there were too many parameters to fit, and I chose to obtain the Hamiltonian matrix elements from *ab initio* calculations. An additional advantage is that this gives the approach predictive power - it allows analysing and identifying potential high absorbing materials by scanning over chemical and physical structures. For example, rather than treating the intermonomer coupling as a Gaussian variable, *ab initio* parameterisation allows explicitly calculating the electronic coupling between units at different distances and angles, thus allowing the method to be applied to particular conformations, for example, results from molecular dynamics calculations. The parameterisation route I have chosen most resembles the work of Karabunarliev and Bittner, [10] where the parameters are obtained from first principles calculations by using a Wannier function basis. The main technical difference in our approaches is that their starting point is the Parriser-Parr-Pople (PPP) approximation, which is a semi-empirical quantum-mechanical method, these results are then used to construct the Wannier functions used for parameterisation. Whereas I start with a DFT calculation followed by a Hartree-Fock energy correction using a one-shot perturbation theory approach. Additionally, their work centres around incorporating the coupling of the electronic states with the lattice vibrations into their calculations, and the analysis of results focuses on the vibronic structure of the calculated excited states, and they do not publish values for their obtained oscillator strengths, which is my core focus.

The goal of the work presented in this thesis is to develop a modelling framework to describe the morphology dependence of excited states in organic semiconductors using a model Hamiltonian parameterised from *ab initio* calculations. The developed modelling framework also has the potential to be applied to the study of charge transfer states at donor-acceptor interfaces if combined with other work on electron-phonon coupling, which would provide more insights into the efficiency of charge pair generation beyond the first step of photoexcitation.

The thesis is structured as follows:

- in chapter 2 - this chapter, I reviewed the relevant theoretical concepts and background literature supporting the research goals of this thesis,
- in chapter 3, I outline the electronic structure methods used in this thesis,
- in chapter 4, I present two case studies on how TDDFT can be used to explore the conformation dependent absorption strength of polymers and small molecules, and conclude that these findings are not enough to explain the experimentally observed structure-property relationships,
- in chapter 5, I present a coarse grained approach to calculate the optical absorption properties of conjugated polymers by applying configuration interaction singles in a basis of Wannier functions (W-CIS) and compare its computational efficiency and accuracy to other methods,
- in chapter 6, I apply W-CIS to study the effect of conformational changes on the optical absorption spectra of two polymers - bond length alteration in polyacetylene and dihedral angles in polythiophene - and link the observed effects on the optical properties to changes in the underlying electronic intermonomer interactions,
- and, finally, in chapter 7, I summarise the thesis achievements and outline areas of future work.

Bibliography

[1] Anna Kohler and Heinz Bassler. *The Electronic Structure of Organic Semiconductors*. 2015.

[2] René A. J. Janssen and Jenny Nelson. Factors limiting device efficiency in organic photovoltaics. *Advanced Materials*, 25(13):1847–1858, December 2012.

[3] Sheridan Few, Jarvist M. Frost, and Jenny Nelson. Models of charge pair generation in organic solar cells. *Physical Chemistry Chemical Physics*, 17(4):2311–2325, 2015.

[4] R. E. Merrifield. Ionized states in a one-dimensional molecular crystal. *The Journal of Chemical Physics*, 34(5):1835–1839, May 1961.

[5] S. Takeno and M. Mabuchi. A theory of Frenkel excitons using a two-level-atom model. *Progress of Theoretical Physics*, 50(6), 1973.

[6] Mikhail Yu. Lavrentiev, William Barford, Simon J. Martin, and Helen Daly. Theoretical investigation of the low-lying electronic structure of poly(p-phenylene vinylene). *Physical Review B*, 59(15), 1999.

[7] V. A. Malyshev and A. V. Malyshev. Statistics of low energy levels of a one-dimensional weakly localized Frenkel exciton: A numerical study. *Phys. Rev. B*, 63, 2001.

[8] A. Race, W. Barford, and R. J. Bursill. Low-lying excitations of polydiacetylene. *Physical Review B*, 64(3), 2001.

[9] William Barford, Robert J. Bursill, and Richard W. Smith. Theoretical and computational studies of excitons in conjugated polymers. *Physical Review B*, 66(11), 2002.

[10] Stoyan Karabunarliev and Eric R. Bittner. Polaron–excitons and electron–vibrational band shapes in conjugated polymers. *The Journal of Chemical Physics*, 118(9), 2003.

[11] W. Barford and M. Marcus. Theory of optical transitions in conjugated polymers. I. Ideal systems. *J Chem Phys*, 141(16):164101, 2014.

[12] Kenneth S. Schweizer. Configurational dependence of the optical properties of pi-conjugated polymers. I. Strong disorder limit. *The Journal of Chemical Physics*, 85(7):4181, 1986.

[13] Vladimir Dobrosavljević and Richard M. Stratt. Role of conformational disorder in the electronic structure of conjugated polymers: Substituted polydiacetylenes. *Physical Review B*, 35(6):2781–2794, 1987.

[14] Z. G. Soos and K. S. Schweizer. Absorption spectrum of flexible conjugated polymers: The weak-disorder limit. *Chem. Phys. Lett.*, 139(2):196–200, 1987.

[15] G. Rossi, R. R. Chance, and R. Silbey. Conformational disorder in conjugated polymers. *The Journal of Chemical Physics*, 90(12):7594, 1989.

[16] Dmitry V. Makhov and William Barford. Local exciton ground states in disordered polymers. *Physical Review B*, 81(16), 2010.

[17] M. Marcus, O. R. Tozer, and W. Barford. Theory of optical transitions in conjugated polymers. II. Real systems. *J Chem Phys*, 141(16):164102, 2014.

[18] M. Kasha, H. R. Rawls, and M. Ashraf el Bayoumi. The exciton model in molecular spectroscopy. *Pure Appl. Chem.*, 11(3-4), 1965.

[19] William Rhodes. Hypochromism and other spectral properties of helical polynucleotides. *J. Amer. Chem. Soc.*, 83(17), 1961.

[20] I. Vragovic and R. Scholz. Frenkel exciton model of optical absorption and photoluminescence in α-PTCDA. *Physical Review B*, 68(15), 2003.

[21] H. Yamagata and F. C. Spano. Interplay between intrachain and interchain interactions in semiconducting polymer assemblies: the HJ-aggregate model. *J Chem Phys*, 136(18):184901, 2012.

[22] H. Yamagata, N. J. Hestand, F. C. Spano, A. Kohler, C. Scharsich, S. T. Hoffmann, and H. Bassler. The red-phase of poly[2-methoxy-5-(2-ethylhexyloxy)-1,4-phenylenevinylene] (MEH-PPV): a disordered HJ-aggregate. *J Chem Phys*, 139(11):114903, 2013.

[23] R. Chang, J.H. Hsu, W.S. Fann, K.K. Liang, C.H. Chang, M. Hayashi, J. Yu, S.H. Lin, E.C. Chang, K.R. Chuang, and S.A. Chen. Experimental and theoretical investigations of absorption and emission spectra of the light-emitting polymer MEH-PPV in solution. *Chem. Phys. Lett.*, 317, 2000.

[24] N. J. Hestand and F. C. Spano. The effect of chain bending on the photophysical properties of conjugated polymers. *J Phys Chem B*, 118(28):8352–63, 2014.

[25] F. C. Spano. The spectral signatures of Frenkel polarons in H- and J-aggregates. *Accounts of Chemical Research*, 43(3):429–439, 2010.

[26] H. Yamagata and F. C. Spano. Vibronic coupling in quantum wires: applications to polydiacetylene. *J Chem Phys*, 135(5):054906, 2011.

[27] F. C. Spano and H. Yamagata. Vibronic coupling in J-aggregates and beyond: a direct means of determining the exciton coherence length from the photoluminescence spectrum. *J Phys Chem B*, 115(18):5133–43, 2011.

[28] D. Hu, J. Yu, K. Wong, Bagchi B., Rossky P. J., and Barbara P. F. Collapse of stiff conjugated polymers with chemical defects into ordered, cylindrical conformations. *Nature*, 405, 2000.

[29] S. Forster, E. Kohl, M. Ivanov, J. Gross, W. Widdra, and W. Janke. Polymer adsorption on reconstructed Au(001): a statistical description of P3HT by scanning tunneling microscopy and coarse-grained Monte Carlo simulations. *J Chem Phys*, 141(16):164701, 2014.

[30] Margherita Moreno, Mose Casalegno, Guido Raos, Stefano V. Meille, and Riccardo Po. Molecular modeling of crystalline alkylthiophene oligomers and polymers. *J Phys Chem B*, 114(4), 2010.

[31] K. N. Schwarz, T. W. Kee, and D. M. Huang. Coarse-grained simulations of the solution-phase self-assembly of poly(3-hexylthiophene) nanostructures. *Nanoscale*, 5(5):2017–27, 2013.

[32] D. M. Huang, R. Faller, K. Do, and A. J. Moule. Coarse-grained computer simulations of polymer/fullerene bulk heterojunctions for organic photovoltaic applications. *J. Chem. Theory Comput.*, 6(2), 2010.

[33] P. Prins, F. C. Grozema, F. Galbrecht, U. Scherf, and L. D. A. Siebbeles. Charge transport along coiled conjugated polymer chains. *J. Phys. Chem. C*, 111(29), 2007.

[34] N. E. Jackson, K. L. Kohlstedt, B. M. Savoie, M. Olvera de la Cruz, G. C. Schatz, L. X.

Chen, and M. A. Ratner. Conformational order in aggregates of conjugated polymers. *J Am Chem Soc*, 137(19):6254–62, 2015.

[35] Sophia N. Yaliraki and Robert J. Silbey. Conformational disorder of conjugated polymers: Implications for optical properties. *The Journal of Chemical Physics*, 104(4):1245, 1996.

[36] W. Zhang, E. D. Gomez, and Milner S. T. Predicting chain dimensions of semiflexible polymers from dihedral potentials. *Macromolecules*, 47, 2014.

[37] M. Fox. *Optical Properties in Solids*. OUP, second edition, 2010.

[38] Kun Huang and Avril Rhys. Theory of light absorption and non-radiative transitions in F-centres. 1950.

[39] A. N. Alias, Z. M. Zabidi, A. M. M. Ali, M. K. Harun, and M. Z. A. Yahya. Optical characterization and properties of polymeric materials for optoelectronic and photonic applications. *IJAST*, 3(5), 2013.

[40] G. Chiappe, E. Louis, E. San-Fabian, and J. A. Verges. Can model hamiltonians describe the electron-electron interaction in pi-conjugated systems? PAH and graphene. *J Phys Condens Matter*, 27(46):463001, 2015.

[41] Gergely Barcza, Örs Legeza, Florian Gebhard, and Reinhard M. Noack. Density matrix renormalization group study of excitons in polydiacetylene chains. *Physical Review B*, 81(4), 2010.

[42] Mark N. Kobrak and Eric R. Bittner. Quantum molecular dynamics study of polaron recombination in conjugated polymers. *Physical Review B*, 62(17), 2000.

[43] Kim Tremel and Sabine Ludwigs. *Morphology of P3HT in Thin Films in Relation to Optical and Electrical Properties*, volume 265 of *Advances in Polymer Science*, pages 39–82. Springer Berlin Heidelberg, 2014.

[44] Jui-Fen Chang, Jenny Clark, Ni Zhao, Henning Sirringhaus, Dag W. Breiby, Jens W. Andreasen, Martin M. Nielsen, Mark Giles, Martin Heeney, and Iain McCulloch. Molecular-

weight dependence of interchain polaron delocalization and exciton bandwidth in high-mobility conjugated polymers. *Phys. Rev. B*, 74, 2006.

[45] Christina Scharsich, Ruth H. Lohwasser, Michael Sommer, Udom Asawapirom, Ullrich Scherf, Mukundan Thelakkat, Dieter Neher, and Anna Köhler. Control of aggregate formation in poly(3-hexylthiophene) by solvent, molecular weight, and synthetic method. *Journal of Polymer Science Part B: Polymer Physics*, 50(6):442–453, 2012.

[46] Felix Peter Vinzenz Koch. *Synthesis and Physical Chemistry of Poly(3-hexylthiophene) a "Monomer-up Approach"*. Thesis, ETH Zurich, 2013.

[47] A. Thiessen, J. Vogelsang, T. Adachi, F. Steiner, D. Vanden Bout, and J. M. Lupton. Unraveling the chromophoric disorder of poly(3-hexylthiophene). *Proc Natl Acad Sci U S A*, 110(38):E3550–6, 2013.

[48] S. Baderschneider, U. Scherf, J. Kohler, and R. Hildner. Influence of the conjugation length on the optical spectra of single ladder-type (p-phenylene) dimers and polymers. *J Phys Chem A*, 120(2):233–40, 2016.

[49] Woojung Chung, Hiroshi Shibaguchi, Ken Terao, Michiya Fujiki, and Masanobu Naito. Evaluation of global conformation of polydialkylsilane using correlation between persistence length and excitonic absorption. *Macromolecules*, 44(16):6568–6573, 2011.

[50] J. L. Bredas, J. P. Calbert, D. A. da Silva Filho, and J. Cornil. Organic semiconductors: A theoretical characterization of the basic parameters governing charge transport. *Proc Natl Acad Sci USA*, 99(9), 2002.

[51] A. V. Gavrilenko, T. D. Matos, C. E. Bonner, S.-S. Sun, C. Zhang, and V. I. Gavrilenko. Optical absorption of poly(thiophene vinylene) conjugated polymers. Experiment and first principle theory. *J. Phys. Chem. C*, 112(21), 2008.

[52] J. Sjoqvist, M. Linares, M. Lindgren, and P. Norman. Molecular dynamics effects on luminescence properties of oligothiophene derivatives: a molecular mechanics-response theory study based on the CHARMM force field and density functional theory. *Phys Chem Chem Phys*, 13(39):17532–42, 2011.

[53] Jonas Sjöqvist, Mathieu Linares, Kurt V. Mikkelsen, and Patrick Norman. QM/MM-MD simulations of conjugated polyelectrolytes: A study of luminescent conjugated oligothiophenes for use as biophysical probes. *The Journal of Physical Chemistry A*, 118(19):3419–3428, April 2014.

[54] M. S. Vezie, S. Few, I. Meager, G. Pieridou, B. Dorling, R. S. Ashraf, A. R. Goni, H. Bronstein, I. McCulloch, S. C. Hayes, M. Campoy-Quiles, and J. Nelson. Exploring the origin of high optical absorption in conjugated polymers. *Nat Mater*, 2016.

[55] J. Torras, J. Casanovas, and C. Aleman. Reviewing extrapolation procedures of the electronic properties on the pi-conjugated polymer limit. *J Phys Chem A*, 116(28):7571–83, 2012.

[56] Bryan E. Kohler and I. D. W. Samuel. Experimental determination of conjugation lengths in long polyene chains. *J. Chem. Phys.*, 103(14), 1995.

Chapter 3

Methods

3.1 Wavefunction based methods

A review on the advances in quantum chemistry methods for the calculation of optical properties can be found here[1], where particular emphasis is put on Configuration Interaction Singles (CIS), which is an expansion of the Hartree-Fock (HF) method. These two methods are used in this thesis and the basic concepts are outlined below, a detailed overview can be found in a review by Dreuw and Head-Gordon [2].

3.1.1 The Hartree-Fock method

The Hartree-Fock (HF) method is an electronic structure method whose aim is to find the set of spin orbitals $\{\phi_a(r)\}$ that form a single Slater determinant

$$\Phi_0(r) = |\phi_1(r)\phi_2(r)...\phi_n(r)| \tag{3.1}$$

that is the best approximation to the ground state of an n-electron system described by the full electronic Hamiltonian $\mathcal{H}$. According to the variation principle, the ground state wavefunction can be found by minimising the energy

$$E_0 = \langle \Phi_0 | \, \mathcal{H} \, | \Phi_0 \rangle \, . \tag{3.2}$$

Further derivations result in an eigenvalue equation referred to as the Hartree-Fock equation

$$\hat{F}(r)\Psi_0(r) = E_0\Psi_0(r), \tag{3.3}$$

where

$$\hat{F}(r) = \sum_{i}^{n} \hat{f}_i(r) \tag{3.4}$$

and $\hat{f}_i(r)$ is the Fock operator, which is an effective one-electron operator given by

$$\hat{f}_i(r) = \hat{h}_i(r) + \hat{J}_i(r) - \hat{K}_i(r). \tag{3.5}$$

Here $\hat{h}_i(r)$ represents the kinetic energy of the i-th electron and electron-nuclei attraction, and $\hat{J}_i(r)$ and $\hat{K}_i(r)$ are the direct and exchange Coulomb operators describing the average electron-electron interactions. The potential energies depend on the spin orbitals of all other electrons and thus the Hartree-Fock equations need to be solved iteratively until a self-consistent solution is reached. Therefore, this approach is often called the self-consistent-field (SCF) method.

An inherent approximation in the Hartree-Fock method is the neglect of explicit electron-electron correlations, and there are many quantum chemical *ab initio* methods (e.g. section 3.2.1) that have emerged to incorporate the missing electron correlations.

3.1.2 Configuration interaction singles

Configuration interaction singles (CIS) is used to calculate the excited-state properties of molecular systems[3]. CIS is an extension of the HF method, where instead of representing the

wavefunction of the N-electron system by a single Slater determinant the exact wavefunction of the system is represented as a linear combination of N-electron Slater determinants. CI determinants are typically constructed from the HF ground state wavefunction $\Phi_0(r)$ (equation 3.1) by replacing one, two or N occupied spin orbitals with the same amount of unoccupied spin orbitals giving singly, doubly or N-tuply excited determinants. In the case of CIS that is used in this thesis, the CI basis is restricted to singly excited determinants and the many-body wavefunction can thus be expressed as

$$\Psi_{CIS} = \sum_{ia} c_i^a \Phi_i^a(r), \tag{3.6}$$

where $\Phi_i^a(r)$ differs from $\Phi_0(r)$ in having an occupied spin orbital ϕ_i replaced with and unoccupied orbital ϕ_a. This many-body wavefunction is then substituted into the time-independent Schrödinger equation

$$\hat{H}(r)\Psi_{CIS}(r) = [\hat{T}(r) + \hat{V}_{el-nuc}(r) + \hat{V}_{el-el}(r)]\Psi_{CIS} = E_{CIS}\Psi_{CIS}(r), \tag{3.7}$$

where $\hat{T}$ is the kinetic energy operator, $\hat{V}_{el-nuc}$ represents the electron-nuclei attraction energy and $\hat{V}_{el-el}$ is the electron-electron interaction energy. The eigenvalues E_{CIS} are the total energies for various excited states, and the excitation energies are simply the difference between the HF ground state energy and the CIS excited state energies.

In this thesis I use two different implementations of CIS - one is the traditional approach using a full-electron basis, and the other uses a coarse-grained basis. The coarse-grained approach is briefly introduced in section 3.3.1 of this chapter, and chapter 5 describes the computational implementation in detail and presents initial results. To evaluate the performance of the coarse-grained approach, I compare these results with calculations using the full-basis CIS method, as implemented in Gaussian 09, Revision C.01[4].

3.2 Density functional theory

One of the most widely used methods to calculate the excited state properties of molecular systems is Time-Dependent Density Functional Theory (TDDFT), which calculates the excited state properties of many-body systems by casting the Schrödinger equation in terms of functionals of the electron density rather than the many-body operators. The formalism was derived by Runge and Gross [5] in 1984 and is based on the earlier work on ground-state DFT by Hohenberg and Kohn [6] and Kohn and Sham [7]. A good review of both of the ground state and time-dependent DFT formalisms are given in the publication by Fiolhais *et al.* [8], and here I will outline only the general calculation scheme and approximations.

All the TDDFT results presented in chapter 4 of this thesis are produced using the linear response formalism of TDDFT as implemented in Gaussian 09, Revision C.01 [4]. Ground state DFT is used to perform geometry optimisations and calculate ground state energies for different structures, and TDDFT is then applied to determine the excitation energies and corresponding oscillator strengths of the optimised structures. Additionally, I use ground state DFT calculations as the first step for obtaining parameters for the Wannier function basis Configuration Interaction Singles method used in chapters 5 and 6, in which case I use the QUANTUM ESPRESSO software package's implementation of DFT using periodic boundary conditions[9][10].

3.2.1 Ground state formalism

The basis of DFT is the reformulation of the many body Schrödinger equation in terms of the electron density as introduced by the Hohenberg and Kohn theorems[11], where the energy operators of the many-body Hamiltonian are expressed as functionals of the electron density. The ground state energy can then be expressed as

$$E[n(r)] = \int d^3r V_{ext}(r)n(r) + T_{NI}[n(r)] + V_H[n(r)] + E_{xc}[n(r)], \tag{3.8}$$

where n is the electron density, V_{ext} is the external potential from the nuclei, T_{NI} is the kinetic energy functional for a system of non-interacting electrons, V_H is the Hartree energy functional for electron-electron interactions and E_{xc} is the exchange-correlation energy functional, which quantifies the errors introduced by neglecting the exchange and correlation effects in the former two energy functionals. DFT is an exact theory and would provide accurate energies if the precise form of the exchange-correlation potential was known. Instead, it has to be approximated, which will be discussed in more detail in section 3.2.3.

The energy of the system can be calculated using the approach outlined by Kohn and Sham [12], by self-consistently solving the single particle Schrödinger equation

$$[-\frac{1}{2}\nabla^2 + V_{KS}]\phi^{KS}(r) = \varepsilon^{KS}\phi^{KS} \tag{3.9}$$

for non-interacting single particle orbitals $\{\phi_i^{KS}\}$ and eigenvalues $\{\varepsilon^{KS}\}$, where V_{KS} is the effective Kohn-Sham potential and is given by

$$V_{KS}(r) = V_{ext}(r) + V_H(r) + V_{xc}(r), \tag{3.10}$$

where V_H is the Hartree potential from electron-electron interactions and V_{xc} is the exchange-correlation potential.

3.2.2 Time dependent formalism

TDDFT is based on the theorems by Runge and Gross [5], which establish a one-to-one mapping of the time-dependent electron density of a system and the external potential this system is experiencing and expresses the quantum mechanical action integral as a functional of the time-dependent electron density. In the linear response formalism the excitation energies of a system are calculated via the linear density response, which is defined as

$$\chi(\vec{r}, t, \vec{r'}, t') = \frac{\delta n(\vec{r}, t)}{\delta V_{KS}(\vec{r'}, t')}. \tag{3.11}$$

The poles of the linear response function in the frequency domain give the excitation energies of the system, and the linear response function of the fully interacting system can be calculated by self-consistently solving the following Dyson equation

$$\chi(\vec{r},\vec{r}',\omega) = \chi_0(\vec{r},\vec{r}',\omega) + \int d^3r_1 d^3r_2 \chi_0(\vec{r},\vec{r}',\omega)\left(\frac{1}{|\vec{r}_1-\vec{r}_2|} + f_{xc}(\vec{r}_1,\vec{r}_2,\omega)\right)\chi(\vec{r}_2,\vec{r}',\omega), \quad (3.12)$$

where χ_0 is the non-interacting linear response function obtained using the ground state Kohn-Sham orbitals and eigenvalues and f_{xc} is the exchange-correlation kernel, which in a simple picture is just the functional derivative of the electron density with respect to the exchange-correlation potential mentioned in section 3.2.1. Thus, the resultant energies will highly depend on the form of the exchange-correlation potential.

3.2.3 Exchange-Correlation energy functionals

The simplest type of exchange-correlation functional is obtained using the local-density approximation (LDA), where the exchange and correlation energies of a system are approximated to be the same as that for a homogeneous electron gas with the same density. By also considering the system's density gradient using the generalised gradient approximation (GGA), the method is expected to give more accurate results.

In chapter 4 of this thesis I will use the BLYP parameterisation[13][14] of the GGA functional. These approximations have been found to poorly capture the properties of organic molecules, especially for excited state calculations, which leads to the use of hybrid functionals, such as B3LYP[15], which replaces a fraction of the GGA exchange energy with exact exchange energy given by Hartree–Fock theory. The parameters that control the fraction of exact and GGA exchange are determined by fitting results to experimental data, which means that the accuracy of the method will not be consistent for all systems and properties. Additionally, many groups have worked on developing functionals that correct the long-range decay of the exchange energy to improve the prediction of excitation energies. One of these approaches is the Coulomb-attenuating method (CAM) proposed by Yanai *et al.* [16], where the fraction of

exact exchange in relation to GGA exchange is varied with distance.

In chapters 5 and 6 of this thesis, where I use DFT calculations as a first step in parameterising the coarse-grained W-CIS Hamiltonian, I use the Gaussian-Perdew-Burke-Ernzerhof (Gau-PBE) parameterisation of the GGA functional[17], as it is suitable for calculations using periodic boundary conditions. This parameterisation is based on the Perdew-Burke-Ernzerhof (PBE) functional[18], but it uses a Gaussian attenuation scheme (Gau) to include short-range HF exchange.

3.2.4 Basis sets

In chapter 4 of this thesis I use basis sets of localised atomic orbitals, which are represented in terms of linear combinations of primitive gaussians of the form

$$g(\alpha, r) = x^a y^b z^c e^{-\alpha r^2}, \tag{3.13}$$

where a, b and c are integers that determine the angular momentum of the orbital and α determines the spread of the function. A minimal basis set contains the amount of orbitals to accommodate the filled orbitals of each atom in the ground state of a given system. Additional functions are added to improve accuracy of ground state calculations, and enable the calculation of polarisabilities and excited state properties. A widely used group of basis sets are Dunning's [19] correlation consistent polarized valence N zeta (cc-pVNZ) basis sets, where in the case of first and second row atoms *N-1* is the number of additional shells of functions added to the core functions. The basis set used for most calculations in this work is cc-pVDZ, which includes three s, two p and one d orbital for all second row atoms, and two s and one p orbital for hydrogen, which corresponds to 48 basis functions in the case of ethene (C_2H_4).

In chapter 5 and 6 where I use DFT calculations as a first step in parameterising the W-CIS Hamiltonian, I am using periodic boundary conditions and thus use plane waves as a basis instead of localised orbitals. All-electron plane-wave calculations are computationally very expensive, so usually core electrons are approximated using pseudo-potentials[20]. In

this thesis I use SG15 optimised norm-conserving Vanderbilt pseudopotentials, which can be obtained using the ONCVSP code[21], and the procedure for generating the pseudopotentials is described by Hamann[22].

3.3 Coarse grained methods for excited state properties

Ground state and time-dependent DFT are good tools to calculate the optical properties of oligomers in different conformations, but as will be shown in chapter 4, there is a need to also consider coarse-grained methods in order to predict the optical properties of longer polymer chains in different conformations. The coarse-grained methods introduced in this section are used to produce the results presented in chapters 5 and 6.

3.3.1 Wannier function basis configuration interaction singles

To study optical properties of long oligomers, we employ the configuration interaction singles (CIS) method in a basis of Wannier functions, as a shorthand we will refer to this approach as Wannier-CIS (W-CIS). In this method, excited states $|\Psi_n\rangle$ are expressed as linear combinations of singly excited Slater determinants according to

$$|\Psi_n\rangle = \sum_{ij} A^n_{ij} c_i^\dagger d_j \, |\Psi_0\rangle = \sum_{ij} A^n_{ij} |ij\rangle, \tag{3.14}$$

where $|ij\rangle$ denotes a Slater determinant with one hole in the highest occupied molecular orbital (HOMO) of monomer i (described by the corresponding Wannier function $W_i^v(\mathbf{r})$) and one electron in the lowest unoccupied molecular orbital (LUMO) of monomer j (described by the Wannier function $W_j^c(\mathbf{r})$). The coefficients A^n_{ij} are solutions of the eigenvalue problem

$$\sum_{i'j'} H_{ij,i'j'} A^n_{i'j'} = E_n A^n_{ij}, \tag{3.15}$$

where E_n denotes the excitation energy and the W-CIS matrix for singlet excitations is given by

$$H_{ij,i'j'} = t^c_{jj'}\delta_{ii'} - t^v_{i'i}\delta_{jj'} + 2U^d_{ij,i'j'} - U^x_{ij,i'j'}. \tag{3.16}$$

Here, $t^{v(c)}_{ii'}$ denotes the onsite energy ϵ^v_i for holes (electrons) on monomer i for $i = i'$ and the hole (electron) hopping energy from monomer i to monomer i' for $i \neq i'$. Also, U^x and U^d denote the exchange and direct Coulomb matrix elements, respectively.

To simplify the determination of the parameters in Eq. (3.16), we assume that the Wannier functions on all momomers of the oligomer are equal to those of an infinitely long chain. Similarly, the hopping energies are assumed to depend only on the separation $s = i - i'$ of the momomers, i.e. $t^{v(c)}_{ii'} = t^{v(c)}_{i-i'} \equiv t^{v(c)}_s$, while the onsite energies are independent of the monomer index. Finally, we have found through explicit calculations that the Coulomb matrix elements have only significant magnitudes if $i = i'$ and $j = j'$, i.e. the two HOMO Wannier functions are located on the same monomer and so are the two LUMO Wannier functions. Then, the Coulomb matrix elements depend only on the separation $s = i - j$ and are given by

$$U^d_s = \int d^3r \int d^3r' W^c_i(\mathbf{r}) W^v_{i+s}(\mathbf{r}') \frac{1}{|\mathbf{r} - \mathbf{r}'|} W^c_i(\mathbf{r}) W^v_{i+s}(\mathbf{r}'), \tag{3.17}$$

$$U^x_s = \int d^3r \int d^3r' W^c_i(\mathbf{r}) W^v_{i+s}(\mathbf{r}') \frac{1}{|\mathbf{r} - \mathbf{r}'|} W^v_{i+s}(\mathbf{r}) W^c_i(\mathbf{r}'). \tag{3.18}$$

Importantly, all parameters of the W-CIS approach are obtained from first-principles calculations, as described in more detail in section 5.2.

The oscillator strength of the transition from the ground state $|GS\rangle$ to excited state $|\Psi_n\rangle$ is given by

$$f_n = \frac{2}{3} E_n |\boldsymbol{\mu}_n|^2. \tag{3.19}$$

Here, $\boldsymbol{\mu}_n$ denotes the transition dipole moment

$$\boldsymbol{\mu}_n = -e \langle GS| \mathbf{r} |\Psi_n\rangle = \sum_{i,s} A^n_{i,i+s} \boldsymbol{\mu}(s), \tag{3.20}$$

where the intermonomer transition dipole moment is calculated as

$$\boldsymbol{\mu}(s) = -e \int d^3 r W^c_i(\boldsymbol{r}) \boldsymbol{r} W^v_{i+s}(\boldsymbol{r}) \tag{3.21}$$

3.3.2 Frenkel exciton model

For comparison, I have also carried out calculations with the Frenkel exciton (FE) model. In this approach, the electron and hole are assumed to sit on the same monomer, i.e. charge transfer (CT) states which are included in the W-CIS approach are neglected. The excited states Ψ^{FE}_n are expressed as a linear combination of singly excited Slater determinants

$$|\Psi^{FE}_n\rangle = \sum_i B^n_i |ii\rangle, \tag{3.22}$$

where $|ii\rangle$ denotes a Slater determinant with a hole in the highest occupied molecular orbital (HOMO) of monomer i and an electron in the lowest unoccupied molecular orbital (LUMO) of the same monomer i, which is consistent with the notation used for the W-CIS method. The coefficients B^n_i are solutions of the eigenvalue problem

$$\sum_{i'} H^{FE}_{i,i'} B^n_{i'} = E^{FE}_n B^n_i, \tag{3.23}$$

where E^{FE}_n denotes the excitation energy. The FE matrix for singlet excitations is given by

$$H^{FE}_{i,i'} = \tilde{E}_i \delta_{ii'} + J_{ii'} \tag{3.24}$$

where $\tilde{E}_i$ is the excitation energy of monomer i and $J_{ii'}$ describes the hopping of a Frenkel exciton from monomer i to monomer i'. Diagonalization of H_{FE} yields excited state energies

E_n^{FE} and the wavefunctions coefficients B_i^n, which determine the transition dipole moment via

$$\boldsymbol{\mu}_n^{FE} = -e \langle GS | \mathbf{r} | \Psi_n^{FE} \rangle = \sum_i B_i^n \boldsymbol{\mu}(0). \tag{3.25}$$

Bibliography

[1] L. Gonzalez, D. Escudero, and L. Serrano-Andres. Progress and challenges in the calculation of electronic excited states. *Chem Phys Chem*, 13, 2012.

[2] Andreas Dreuw and Martin Head-Gordon. Single-reference ab initio methods for the calculation of excited states of large molecules. *Chemical Reviews*, 105(11):4009–4037, oct 2005.

[3] James B Foresman, Martin Head-Gordon, John A Pople, and Michael J Frisch. Toward a systematic molecular orbital theory for excited states. *The Journal of Physical Chemistry*, 96(1):135–149, 1992.

[4] M. J. Frisch, G. W. Trucks, H. B. Schlegel, G. E. Scuseria, M. A. Robb, J. R. Cheeseman, G. Scalmani, V. Barone, B. Mennucci, G. A. Petersson, H. Nakatsuji, M. Caricato, X. Li, H. P. Hratchian, A. F. Izmaylov, J. Bloino, G. Zheng, J. L. Sonnenberg, M. Hada, M. Ehara, K. Toyota, R. Fukuda, J. Hasegawa, M. Ishida, T. Nakajima, Y. Honda, O. Kitao, H. Nakai, T. Vreven, J. A. Montgomery, Jr., J. E. Peralta, F. Ogliaro, M. Bearpark, J. J. Heyd, E. Brothers, K. N. Kudin, V. N. Staroverov, R. Kobayashi, J. Normand, K. Raghavachari, A. Rendell, J. C. Burant, S. S. Iyengar, J. Tomasi, M. Cossi, N. Rega, J. M. Millam, M. Klene, J. E. Knox, J. B. Cross, V. Bakken, C. Adamo, J. Jaramillo, R. Gomperts, R. E. Stratmann, O. Yazyev, A. J. Austin, R. Cammi, C. Pomelli, J. W. Ochterski, R. L. Martin, K. Morokuma, V. G. Zakrzewski, G. A. Voth, P. Salvador, J. J. Dannenberg, S. Dapprich, A. D. Daniels, Ö. Farkas, J. B. Foresman, J. V. Ortiz, J. Cioslowski, and D. J. Fox. Gaussian 09 Revision C.01. Gaussian, Inc., Wallingford CT, 2009.

[5] Erich Runge and E. K. Gross. Density-functional theory for time-dependent systems. *Physical Review Letters*, 52(12), 1984.

[6] P Hohenberg and W. Kohn. Inhomogeneous electron gas. *Phys. Rev.*, 136(3B), 1964.

[7] W. Kohn and L. J. Sham. Self-consistent equations including exchange and correlation effects. *Phys. Rev.*, 140(4A), 1965.

[8] C. Fiolhais, F. Nogueira, and M. Marques, editors. *A Primer in Density Functional Theory*, volume 620 of *Lecture Notes in Physics*. Springer, 2003.

[9] Paolo Giannozzi, Stefano Baroni, Nicola Bonini, Matteo Calandra, Roberto Car, Carlo Cavazzoni, Davide Ceresoli, Guido L Chiarotti, Matteo Cococcioni, Ismaila Dabo, Andrea Dal Corso, Stefano de Gironcoli, Stefano Fabris, Guido Fratesi, Ralph Gebauer, Uwe Gerstmann, Christos Gougoussis, Anton Kokalj, Michele Lazzeri, Layla Martin-Samos, Nicola Marzari, Francesco Mauri, Riccardo Mazzarello, Stefano Paolini, Alfredo Pasquarello, Lorenzo Paulatto, Carlo Sbraccia, Sandro Scandolo, Gabriele Sclauzero, Ari P Seitsonen, Alexander Smogunov, Paolo Umari, and Renata M Wentzcovitch. QUANTUM ESPRESSO: a modular and open-source software project for quantum simulations of materials. *Journal of Physics: Condensed Matter*, 21(39):395502 (19pp), 2009.

[10] P Giannozzi, O Andreussi, T Brumme, O Bunau, M Buongiorno Nardelli, M Calandra, R Car, C Cavazzoni, D Ceresoli, M Cococcioni, N Colonna, I Carnimeo, A Dal Corso, S de Gironcoli, P Delugas, R A DiStasio Jr, A Ferretti, A Floris, G Fratesi, G Fugallo, R Gebauer, U Gerstmann, F Giustino, T Gorni, J Jia, M Kawamura, H-Y Ko, A Kokalj, E Küçükbenli, M Lazzeri, M Marsili, N Marzari, F Mauri, N L Nguyen, H-V Nguyen, A Otero de-la Roza, L Paulatto, S Poncé, D Rocca, R Sabatini, B Santra, M Schlipf, A P Seitsonen, A Smogunov, I Timrov, T Thonhauser, P Umari, N Vast, X Wu, and S Baroni. Advanced capabilities for materials modelling with QUANTUM ESPRESSO. *Journal of Physics: Condensed Matter*, 29(46):465901, 2017.

[11] P. Hohenberg and W. Kohn. Inhomogeneous electron gas. *Phys. Rev.*, 136(3B):864–871, 1964.

[12] W. Kohn and L.J. Sham. Self-consistent equations including exchange and correlation effects. *Phys. Rev.*, 140(4A):1133–1138, 1965.

[13] A.D. Becke. Density-functional exchange-energy approximation with correct asymptotic behaviour. *Phys. Rev. A*, 38(6), 1988.

[14] C. Lee, W. Yang, and R.G. Parr. Development of the Colle-Salvetti correlation-energy formula into a functional of the electron density. *Phys. Rev. B*, 37(2), 1988.

[15] A.D. Becke. Density functional thermochemistry. iii. the role of exact exchange. *J. Chem. Phys.*, 98(7), 1993.

[16] T. Yanai, D.P. Tew, and N.C. Handy. A new hybrid exchange-correlation functional using the coulumb-attenuating method (CAM-B3LYP). *Chem. Phys. Lett.*, 393, 2004.

[17] Jong-Won Song, Koichi Yamashita, and Kimihiko Hirao. Communication: A new hybrid exchange correlation functional for band-gap calculations using a short-range gaussian attenuation (gaussian-perdue–burke–ernzerhof). *The Journal of Chemical Physics*, 135(7):071103, aug 2011.

[18] John P. Perdew, Kieron Burke, and Matthias Ernzerhof. Generalized gradient approximation made simple. *Physical Review Letters*, 77(18):3865–3868, oct 1996.

[19] T. H. Dunning Jr. Gaussian basis sets for use in correlated molecular calculations. I. The atoms boron through neon and hydrogen. *J. Chem. Phys.*, 90(2):1007–1023, 1989.

[20] Warren E. Pickett. Pseudopotential methods in condensed matter applications. *Computer Physics Reports*, 9(3):115–197, apr 1989.

[21] D. R. Hamann. Open-source pseudopotential code oncvpsp.

[22] D. R. Hamann. Optimized norm-conserving vanderbilt pseudopotentials. *Physical Review B*, 88(8), aug 2013.

Chapter 4

Conformation dependent optical properties studied using TDDFT

4.1 Introduction

This chapter addresses the question whether quantum chemical calculations, such as time dependent density functional theory (TDDFT), can reproduce and explain the origin of experimentally observed trends of optical properties in organic semiconductors, especially focusing on the structure-property relationships. TDDFT is widely used in this field of study, as it offers great compromise between accuracy and computational efficiency. In this chapter I present two case studies looking at the structure dependent optical properties of polythiophene in section 4.2 and the two small molecules (5Z,5'Z)-5,5'-((7,7'-(4,4,9,9-tetraoctyl-4,9-dihydro-s-indaceno[1,2-b:5,6-b']dithiophene-2,7-diyl)bis(benzo[c][1,2,5]thiadiazole-7,4-diyl))bis(methanylylidene))bis(3-ethyl-2-thioxothiazolidin-4-one) and (5Z,5'Z)-5,5'-((7,7'-(4,4,9,9-tetraoctyl-4,9-dihydro-s-indaceno[1,2-b:5,6-b']dithiophene-2,7-diyl)bis(benzo[c][1,2,5]thiadiazole-7,4-diyl))bis(methanylylidene))bis(3-ethyl-2-thioxothiazolidin-4-one) (IDTBR and IDFBR) in section 4.3.

Even though a lot of new polymers have been designed that display higher efficiencies in devices, poly(3-hexylthiophene) (P3HT) is still often used as a model material to understand the relationship between microstructure and electronic properties[1] [2]. Furthermore, blends of P3HT

and acceptor molecules are studied to get a more realistic picture of the optical properties of the optical layer in a solar cell, for example studies on P3HT and PCBM[3] [4].

The discovery of small-molecular acceptors other than fullerenes, so called non fullerene acceptors (NFAs) has led to an increase in efficiency of bulk heterojunction solar cells [5]. The improved performance is largely due to the optical properties of the NFAs and the fact that, unlike fullerenes, they show visible absorption peaks that are both strong and chemically tunable. Some NFAs such as the ITIC/IDIC families show very intense optical absorption strength [6]. Therefore there is great interest in understanding and optimising the photophysical properties of NFAs.

Let us consider the study by Rezasoltani et al. that studies blends of P3HT and the two non-fullerene acceptors IDTBR and IDFBR [7]. They showed that changing the fraction of the NFAs changes the crystalline-to-amorphous fraction of the P3HT component. So the optical spectra of the blends are not simply superpositions of the separate spectra of the polymer and the NFA. Also, there is significant overlap between the spectra of IDFBR and P3HT, making the interpretation of the absorption spectra even harder. The study concludes that using non-destructive optical probes can provide an efficient way to explore the huge chemical phase space and wide range of compositions and microstructures of new promising NFAs for solar cells. There is a need to further investigate the microstructure, particularly the amorphous phase of the blends. For this optical probing has the most potential, as many other structural analysis techniques help characterise crystalline parts of samples.

In this chapter I am using TDDFT to calculate the optical properties of P3HT and the two NFAs IDTBR and IDFBR in different conformations, and I will compare the results to the experimentally measured optical spectra. Having a better understanding of how the optical properties vary with conformation for the polymer, the two NFAs and their blends can be helpful for analysing the experimental spectra, as well as come up with design criteria for new materials. Therefore, in this chapter I test the suitability of TDDFT as a means of screening conformation-dependent optical properties of these materials. I will first consider the optical absorption properties of oligothiophenes of different lengths and conformations in section 4.2,

and then the two NFAs IDTBR and IDFBR in section 4.3.

4.2 Oligomer length and conformation dependent absorption of polythiophene

4.2.1 Experimental context

Figure 4.1a shows the optical spectra of thin films of regio-regular (rr) and regio-random (rra) P3HT. rr-P3HT has a very high degree of regioregularity, meaning that a larger fraction of the polymer exhibits a head-to-tail coupling, as shown in the top diagram of figure 4.1b. This organisation of sidechains encourages a very regular coupling pattern and results in more planar and straighter polymer backbones compared to rra-P3HT, which has a much less regular coupling pattern and thus more regions where the hindrance between sidechains causes the polymer backbone to twist and bend (bottom diagram of figure 4.1b). Thus, the rra-P3HT chains have a shorter effective conjugation length, as the chain twisting can break the π-conjugation along the backbone limiting the degree of electronic coupling between the neighbouring chains, and the chains also exhibit more bending. The optical spectrum of rr-P3HT has a higher and red-shifted low energy absorption peak compared to the rra-P3HT.

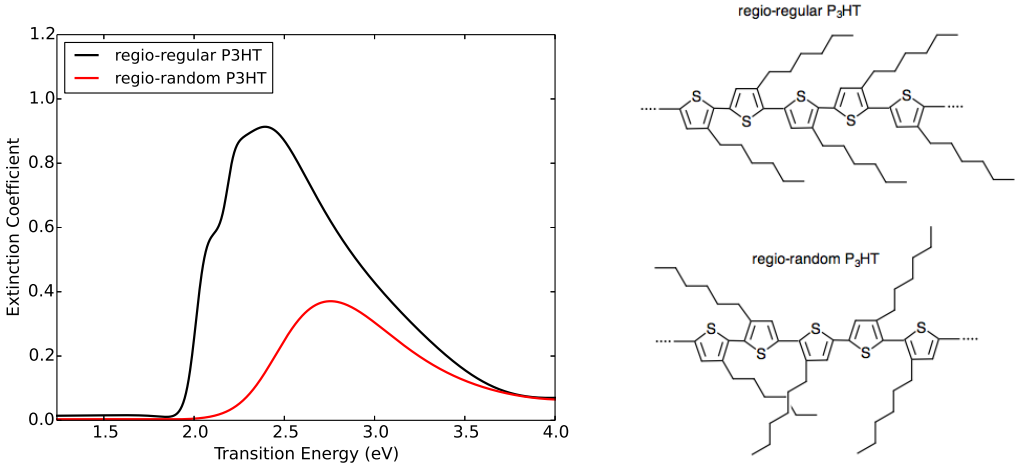

(a) (b)

Figure 4.1: (a) Extinction coefficient as a function of energy of the incoming light for regio-regular and regio-random P3HT thin films, experimental data provided by Mariano Campoy-Quiles.[8][9]

4.2.2 Calculations

In order to investigate the optical absorption properties of polythiophene, I performed a series of calculations for oligothiophenes of different length and conformation and looked at the potential conformations present in the material and the progression of excitation energies and corresponding oscillator strengths. I then compare the observed behaviour to experimental measurements for highly monodisperse regio-regular 3HT oligomers in solution.

In order to make the calculations more computationally accessible, the hexyl sidechains present in 3HT oligomers were substitued with hydrogen atoms (see figure 4.3b). This does not significantly affect the results of the excited state calculations, as the hexyl sidechains do not contribute to the excitations in the low energy part of the spectrum that is relevant to photovoltaic applications.

As a first step ground state DFT is used to perform a geometry relaxation on the structures of interest, followed by a time-dependent density functional theory (TDDFT) calculation, which gives the excitation energies and oscillator strengths. No geometrical constraints were imposed in these calculations.

Before analysing the optical properties of the oligothiophenes, it is important to note that

the use of different exchange-correlation functionals resulted in differences in the optimised geometries of the oligomers, such as the dihedral angle between neighbouring monomer units and bend angles (in the y direction in figure 4.2a). The calculated transition energies and oscillator strengths depend on both the geometry of the oligomers and on the parameters, such as the exchange-correlation functional, used in the TDDFT calculation.

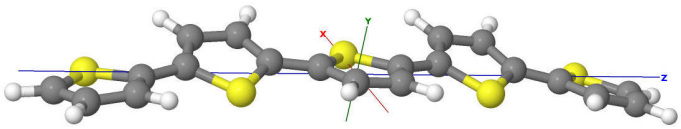

(a) trans-pentathiophene

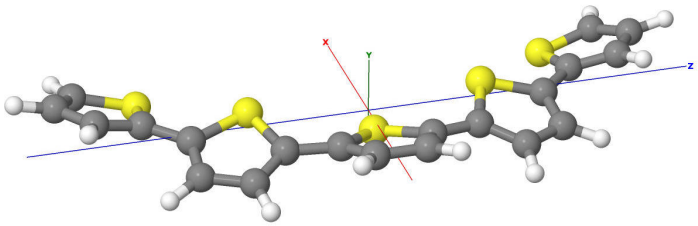

(b) cis-pentathiophene

Figure 4.2: Orientation along the Cartesian axes (red - x, green - y, blue - z) of the optimised structures of trans- and cis-pentathiophene. Calculation details: geometry optimisation in DFT (CAM-B3LYP/cc-pVDZ).

First, I look at how the transition energies depend on oligomer length, ranging from 3 to 22 monomer units. The calculated transition energies from the ground state to the lowest excited state are summarised in figure 4.3a, which also includes a comparison to experimental results[10] for 3HT oligomers in solution. Three exchange-correlation functionals were used - the GGA functional BLYP, the hybrid functional B3LYP and the range-separate hybrid functional CAM-B3LYP, which includes different fractions of exact exchange depending on the distance. The best agreement between experiment and calculation is obtained using the CAM-B3LYP functional. The same calculation was repeated including solvent effects by using the polarisable continuum model as implemented in Gaussian 09. This did not significantly change the resultant excitation energies, as can be seen in figure 4.3a, therefore, all further calculations were performed in vacuum to simplify the calculations.

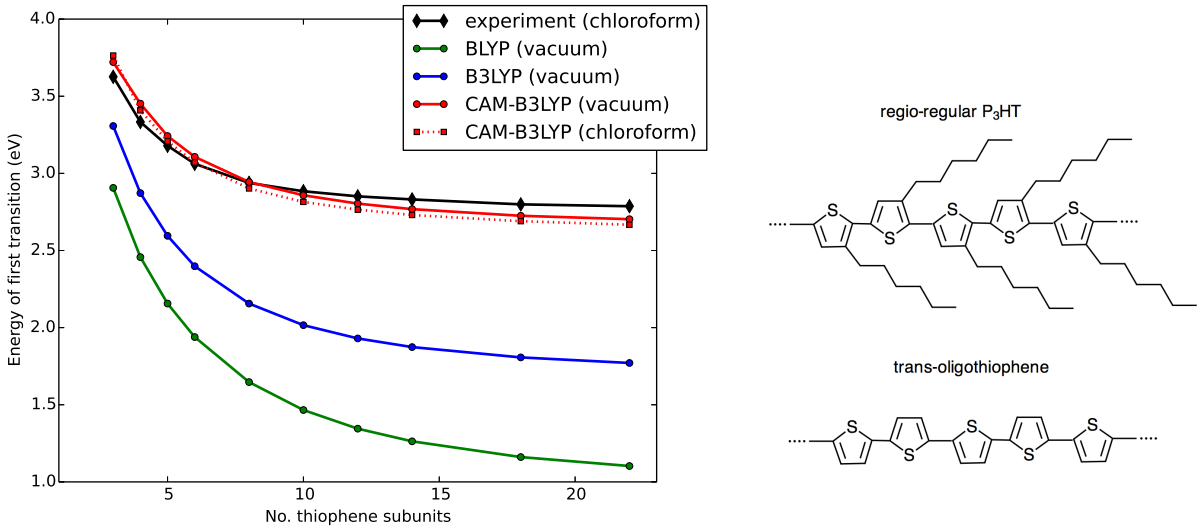

(a) (b)

Figure 4.3: Transition energies from the ground state to the lowest singlet state measured experimentally for regio-regular 3HT oligomers in chloroform and calculated for trans-oligothiophenes in vacuum (for BLYP, B3LYP and CAM-B3LYP) and in chloroform (for CAM-B3LYP). Calculation details: geometry optimisation using DFT (cc-pVDZ) and excited states using TDDFT (cc-pVDZ).

The comparison of experimental absorption strength to calculated oscillator strength is less straight forward. Experimental studies report values of absorbance, molar or mass extinction coefficients or another measure of absorption at the maximum of a peak in the measured optical spectrum. The oscillator strength obtained in calculations is proportional to the area under the broadened peak, so a direct comparison of the values also requires the knowledge of the broadening of each electronic transition. It is possible to use *ab initio* calculations to obtain the broadening and vibronic features of these excitations by analysing the vibrational spectrum of the system and the coupling of the vibrational excitations to the electronic ones, but this has not been implemented in the scope of this work. However, assuming there is only one electronic transition with non-zero oscillator strength that contributes to an absorption peak in an experimentally measured absorption spectrum, the molar attenuation coefficient (given by the maximum value of this peak) is proportional to the oscillator strength at this transition energy. Note that this is only true if we assume that the broadening of the peaks is the same for the different length oligomers. Similarly, the mass attenuation coefficient is proportional to the specific oscillator strength (oscillator strength divided by the molecular mass).

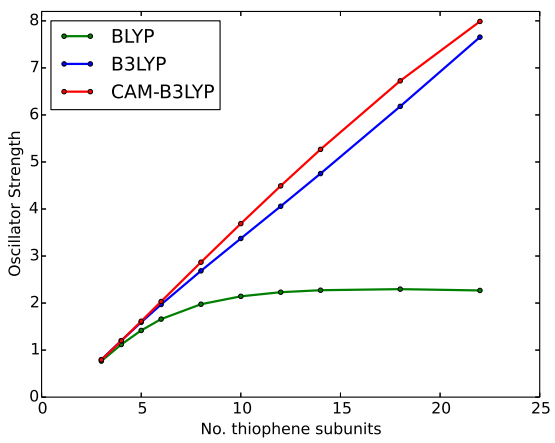

(a)

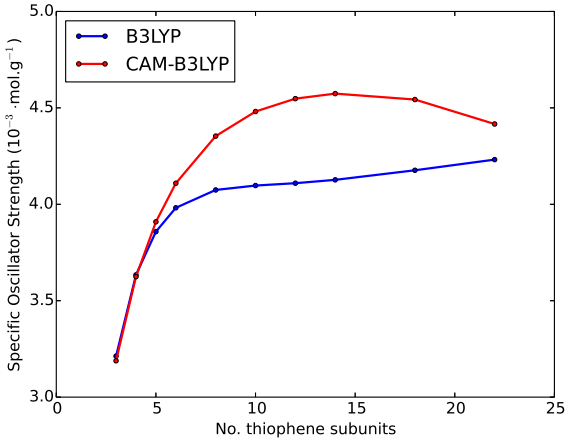

(b)

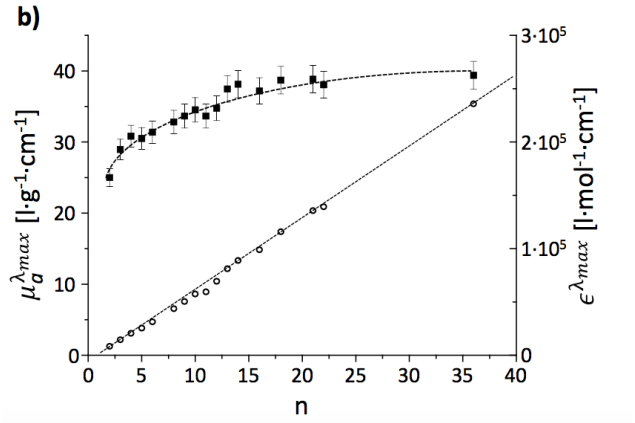

(c)

Figure 4.4: (a) Total and (b) specific oscillator strength of the first excitation for trans-oligothiophenes calculated using different exchange-correlation functionals. Calculation details: geometry optimisation using DFT (cc-pVDZ) and excited states using TDDFT (cc-pVDZ). (c) Mass attenuation coefficient μ_a and molar attenuation coefficient ϵ for lowest energy transition measured experimentally for 3HT oligomers [10].

Figure 4.4a shows the first transition's oscillator strength predicted by TDDFT using the three considered functionals as a function of oligomer length. The results obtained when using the BLYP functional show that the oscillator strength converges to a value of around 2 for oligomers with more than 10 monomer units. This is very different from the behaviour predicted by the two hybrid functionals, B3LYP and CAM-B3LYP, and also the experimental trend of the molar attenuation coefficient (empty circles in figure 4.4c). Figure 4.4b shows the specific oscillator strengths calculated using the two hybrid functionals. These results, except for the last two data points in the CAM-B3LYP series, show an increase in the specific absorption strength. It is important to note that the same trend is observed in the experimental mass attenuation

coefficient (filled squares in figure 4.4c). In other words, there is a superlinear increase in the absorption strength with oligomer length. The decrease in specific oscillator strength for the 18-mer and 22-mer calculated using the CAM-B3LYP functional can be attributed to a change in the calculated ground state geometries, as the trans-oligothiophenes start bending out of plane (in the direction of the y axis in figure 4.2a), when the length exceeds 14 monomer units. The effect of chain bending on the absorption strength is discussed next.

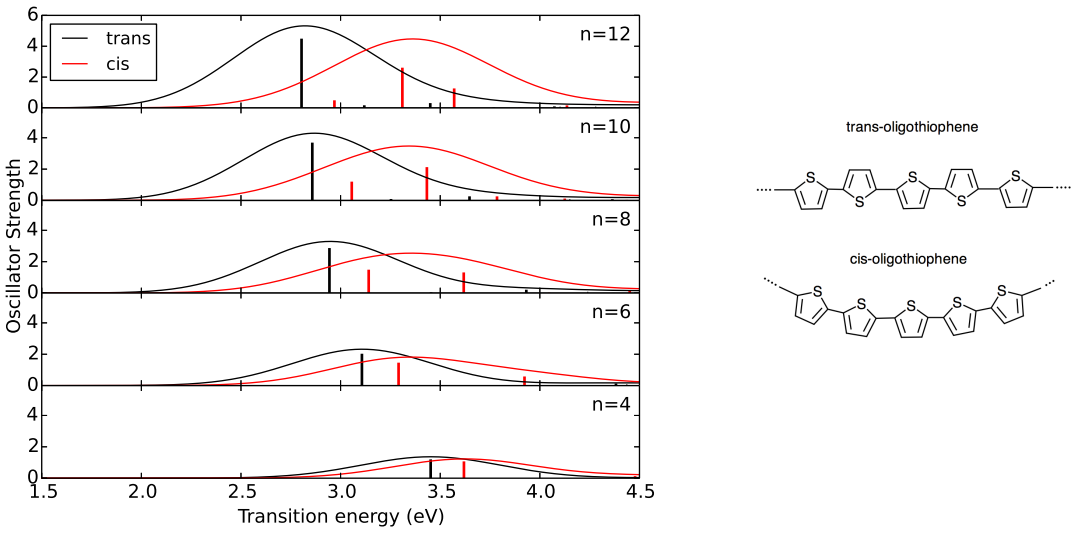

(a) (b)

Figure 4.5: (a) Oscillator strength spectra for different lengths of trans- and cis-oligothiophenes. Calculation details: geometry optimisation using DFT (CAM-B3LYP/cc-pVDZ) and excited states using TDDFT (CAM-B3LYP/cc-pVDZ).

Finally, I consider what happens to the optical absorption properties when varying the co-linearity of oligothiophenes. Figure 4.5a shows the progression of the calculated oscillator strengths broadened with a Gaussian function for trans- and cis-oligothiophenes for different length oligomers. The structures were optimised without any geometrical constraints, and the relaxed structures of the two conformations of pentathiophene are shown in figure 4.2. The main difference is that the cis-oligothiophenes bend in the direction of their short axis (x axis in figure 4.2). Neither of the conformations showed significant bending out of plane (y axis in figure 4.2). The difference between the excitation energies of the first transition for cis- and trans-oligothiophenes is approximately 0.18 eV. This difference is largely due to the difference in the dihedral angle of the two structures, as the relaxed structure of the trans-conformation

has a smaller dihedral angle than the cis-conformation, which allows for more orbital overlap and electron delocalisation along the chain, thus lowering the transition energy. This was confirmed by repeating the same calculations for oligomers of length 3, 4 and 6 repeat units where the dihedral angle was constrained to 180° during the geometry relaxation. The difference in the first transition energies was below 0.05 eV when both the cis- and trans-oligothiophenes were planarised. Note that the results of these calculations are not shown in figure 4.5.

In order to compare the position and height of the absorption maximum between the two conformations, the calculated excitations are broadened using a Gaussian function with a broadening coefficient resulting in peak widths comparable to experimental values reported by[10]. The results for the lowest energy excitation of the trans conformation are the same as were shown in figures 4.3 and 4.4. We can see that the lowest energy transition is also the brightest in this spectral range and the main transition contributing to the broadened absorption peak. The transition dipole moment of this transition is along the oligomer backbone (z axis in figure 4.2) and is increasing with length for the trans-oligothiophene, but the higher energy transitions are dark. In the case of the cis-oligothiophenes, the oligomer chain is bent in the direction of its short axis (x axis in figure 4.2), and we can see that higher energy transition become available. The transition dipole moment of the second excitation that is growing in strength with increasing oligomer length is along the short axis. The decrease in the oscillator strength of the lowest energy transition can be explained by a decrease in the transition dipole moment along the backbone of the oligomer, as it gets more bent. This redistribution of oscillator strength for the cis-oligothiophenes results in a blue-shift of the position and decrease in height of the broadened peak in comparison to the trans-oligothiophene. These findings are in agreement with other studies [11] [12] which showed a redistribution of oscillator strength to a higher energy transition with increased chain bending.

4.3 Absorption strength of non-fullerene acceptors IDTBR and IDFBR

In this section I will consider the optical absorption properties of two small molecules IDFBR and IDTBR, which have very similar chemical structures (see figure 4.6). Studies have shown that one of the key structural differences between them is that IDTBR has a more planar backbone [13] and that IDFBR has a twisted backbone [14]. Therefore, these molecules are a great candidate to gain more insight into the structure-property relationship of conjugated materials.

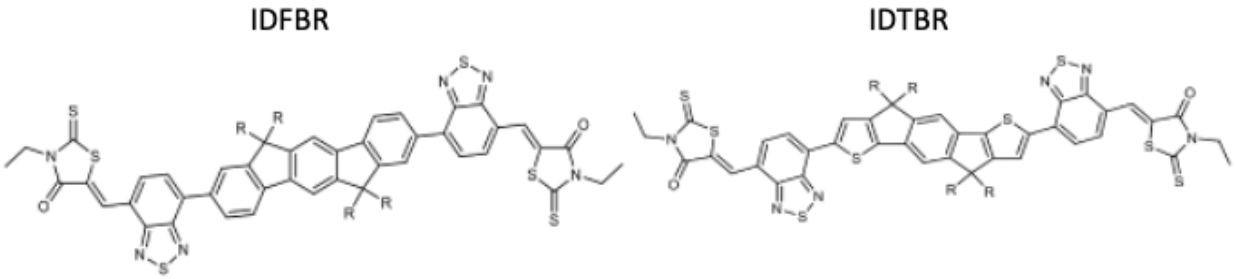

Figure 4.6: Chemical structure of IDFBR and IDTBR. In the case of O-IDFBR and O-IDTBR whose experimental data is presented in this chapter, R represents n-octyl side chains.

4.3.1 Experimental observations of optical absorption

Figure 4.13b shows the optical properties of O-IDTBR and O-IDFBR in solution and in solid state form measured by Dr Elham Rezasoltani. The dashed lines are the solid state absorption coefficients obtained from the complex refractive data collected using spectroscopic ellipsometry as reported in [7]. The full lines represent the equivalent solid-state absorption coefficient obtained from solution measurements of decadic extinction coefficients in chloroform, repeated at concentrations in the range of 0.1 to 0.0001 g/L (unpublished data). The solid-state equivalent was obtained assuming a density of molecules 1 g/cm^3 and scaling the molecular extinction to the appropriate density.

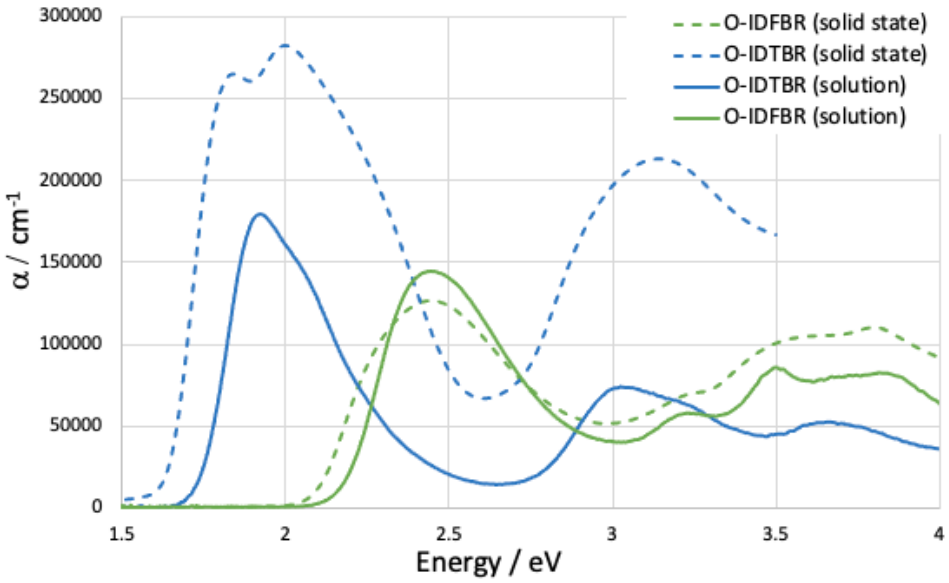

Figure 4.7: Experimentally measured optical spectra of O-IDTBR (blue) and O-IDFBR (green), in solution (solid lines) and solid state (dashed lines).

Both molecules have a distinct high absorption peak at the low energy end of the spectrum, around 1.8 eV for O-IDTBR and just below 2.5 eV for O-IDFBR. The O-IDTBR spectra are thus red shifted compared to the O-IDFBR spectra. Additionally, O-IDTBR absorbs more strongly compared to O-IDFBR both in solution and in the solid state. However, the solid state O-IDTBR spectrum is quite different from the solution spectrum - the low energy absorption peak is red shifted, it has a more distinct vibronic peak structure, and, finally, the absorption strength is greatly enhanced, whereas the solid state and solution spectra for O-IDFBR are very similar. It is known that O-IDTBR is more crystalline than O-IDFBR [7], this is in agreement with seeing a larger difference in solid state and solution spectra for O-IDTBR. The strong increase in absorption strength going from the solution equivalent to the solid state spectrum for O-IDTBR may be related to the strong crystallisation tendency of the O-IDTBR molecule or to its unusually high refractive index, and deserves further study but will not be addressed in this thesis. Note that since solid-state effects like intermolecular interactions are not considered by TDDFT, so the TDDFT calculations in the next section will be compared with the specific absorption strength obtained from solution measurements, rather than those from solid-state measurements.

4.3.2 Calculations of optical absorption by IDTBR and IDFBR using TDDFT

In order to gain an insight into the most stable conformations of IDTBR and IDFBR, I have performed a series of ground state DFT geometry optimisation calculations on different conformers. The different conformers were constructed by rotating the benzothiadizole (BT) and rhodanine groups around the central IDT and IDF units, as shown in figure 4.8 and figure 4.9, respectively, and then performing a geometry optimisation to find the local minimum of the conformers. The most stable conformer is depicted in the top left corner for both structures. There is a significant energy difference between the different conformers of IDTBR, in the range of 69 meV to 87 meV. The energy barrier between the two IDFBR conformers where only the BT units are rotated is much lower, specifically 28 meV, which is very close the thermal energy at room temperature. This difference in energy barriers is likely due to the difference of the interaction due to the sulphur atoms in the BT and IDT units in the case of IDTBR.

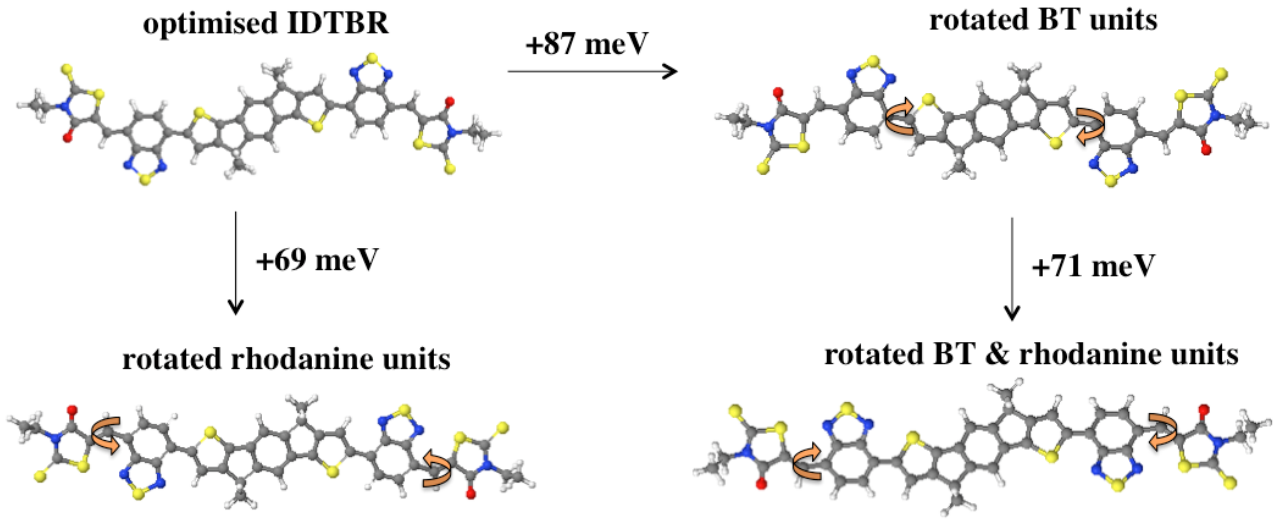

Figure 4.8: Energy barriers between different IDTBR conformers, taken from DFT geometry optimisation calculations using the ωB97XD functional and cc-pVDZ basis set.

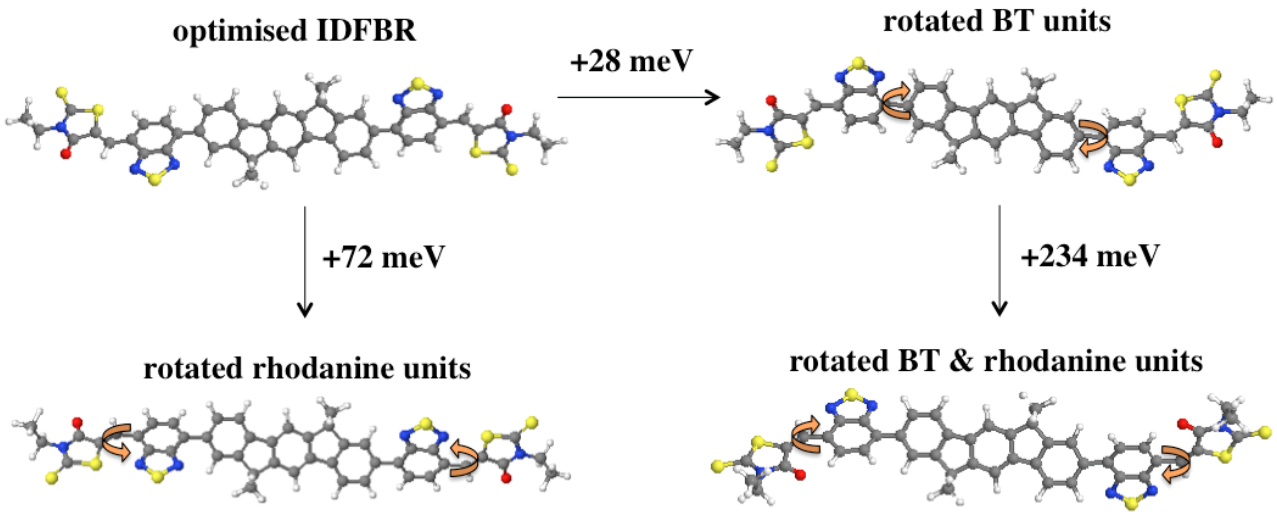

Figure 4.9: Energy barriers between different IDFBR conformers, taken from DFT geometry optimisation calculations using the ωB97XD functional and cc-pVDZ basis set.

The most significant difference between the optimised structures of IDTBR and IDFBR is that IDTBR is planar, whereas IDFBR has non-zero dihedral angles between the IDF, BT and rhodanine units, as shown in figure 4.10. The cost of planarising IDFBR is calculated as the difference in ground state energy between a freely optimised IDFBR molecule and one where its dihedral angles are constrained to 0°. The energy needed to planarise the molecule is very high at 182 meV.

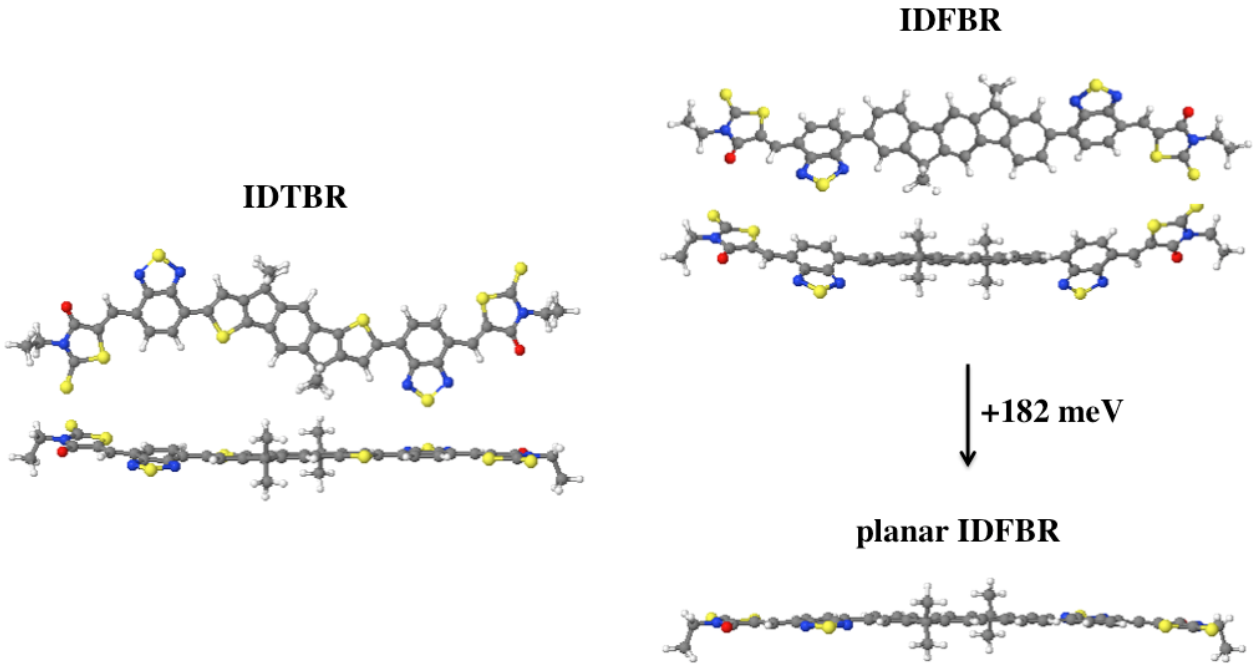

Figure 4.10: Comparing planarity between IDTBR and IDFBR.

Before comparing the optical properties between the two molecules, it is worth first comparing their basic electronic properties. Figure 4.11 depicts the frontier molecular orbitals of the ground state conformations of IDTBR and IDFBR, as well as planarised IDFBR. The associated orbital energies are shown in figure 4.12. For all structures the HOMO is centred on the central IDT or IDF unit and extends across the BT units and partially to the rhodanine units. The LUMO is split into two parts, each mainly localised on the BT units and partially on the rhodanine units, so the BT units act as acceptors in these structures.

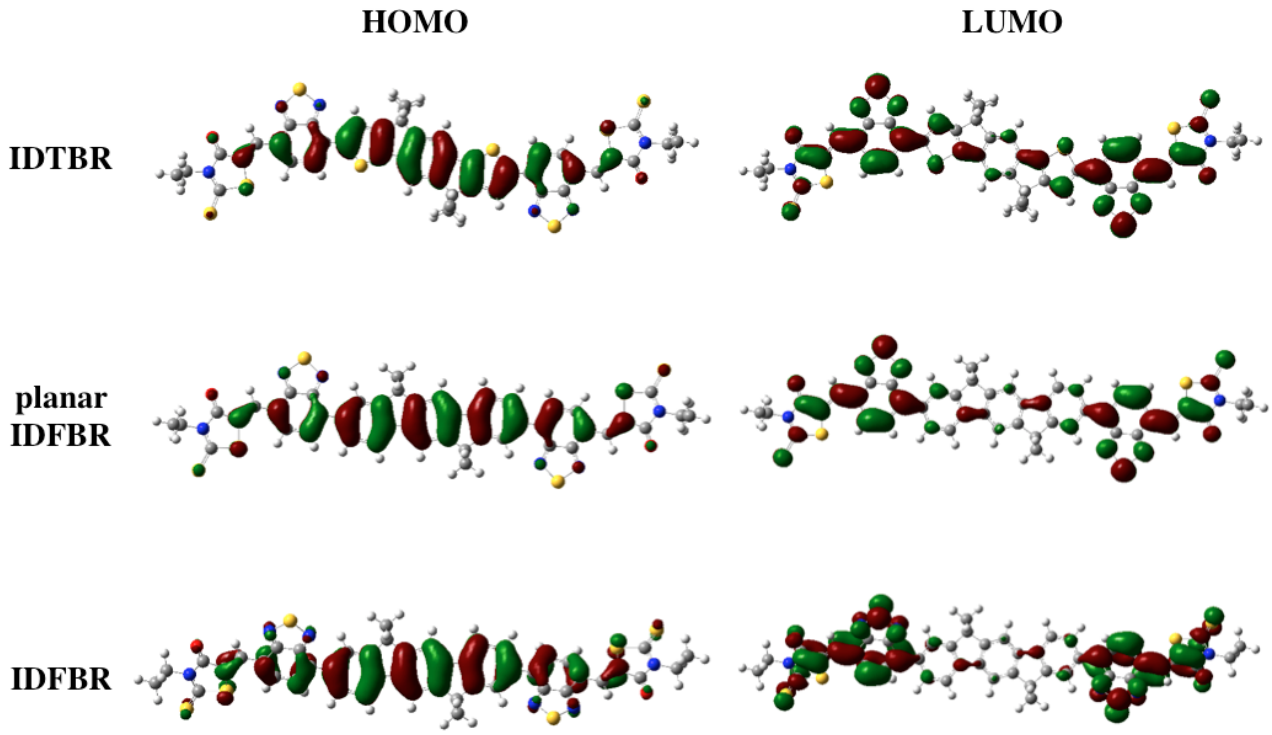

Figure 4.11: Frontier molecular orbitals of freely optimised IDTBR and IDFBR, as well as planarised IDFBR.

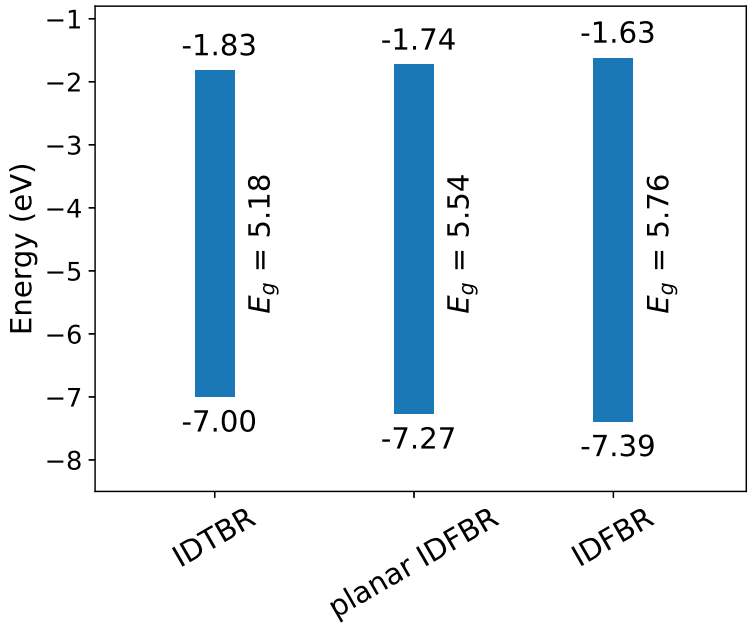

Figure 4.12: HOMO and LUMO energies and the resulting electronic band gaps (E_g) of freely optimised IDTBR and IDFBR, as well as planarised IDFBR.

The LUMO slightly extends into the central IDT or IDF unit - the LUMO is most localised for the IDFBR, followed by the planarised IDFBR and is most extended for the IDTBR. This trend in LUMO localisation is mirrored by the orbital energies - the energy of IDFBR's LUMO is $-1.63\ eV$, planarised IDFBR's is $-1.74\ eV$ and IDTBR's is $-1.83\ eV$ - the most localised LUMO having the highest energy. It is hard to visually evaluate differences in localisation of the HOMOs of the three structures, the energies of the HOMOs follow the opposite trend, IDTBR having the highest energy HOMO at $-7.00\ eV$, followed by planarised IDFBR with $-7.27\ eV$ and freely optimised IDFBR having the lowest HOMO at $-7.39\ eV$. Thus, the electronic band gap (E_g) is increasing going from IDTBR with 5.18 eV, followed by planarised IDFBR with 5.54 eV and freely optimised IDFBR with 5.76 eV. So, of the 0.58 eV difference in band gaps between IDTBR and IDFBR only 0.22 eV or 38% can be attributed to IDFBR not being planar.

Next, in order to compare the optical properties of the two materials, I have calculated the excited states of all the optimised structures described above. Figure 4.13a shows the calculated optical absorption spectra obtained by converting the calculated transition energies E_{ij} and oscillator strengths f_{ij} into the imaginary part of the dielectric function ϵ_2 according to

$$\epsilon_2(E) = \frac{2\pi N_m e^2}{\epsilon_0 m_e} \sum_{ij} \frac{\hbar f_{ij}}{E} \delta(E - E_{ij}), \tag{4.1}$$

where e is the electron charge, ϵ_0 is the permittivity of free space, m_e is the electron mass, $\hbar$ is the reduced Planck's constant and N_m is the volume density of oscillators, which can be approximated as the density of the material (assumed to be 1 $g.cm^{-3}$) divided by the molecule's molecular weight. I choose to calculate ϵ_2 as this optical quantity does not require knowledge of the refractive index, which cannot be extracted from my excited state calculations. In order to compare the calculated spectra to experiment, figure 4.13b plots the experimentally measured spectra converted into ϵ_2 according to

$$\epsilon_2(E) = 2nk = 2n\frac{\lambda}{4\pi}\alpha(E), \tag{4.2}$$

where n and k are the real and imaginary part of the complex refractive index, λ is the wavelength of the incident light and α is the absorption coefficient as shown in figure 4.7. I assumed a refractive index $n = 2$ for both materials; this is also close to the value obtained from ellipsometry [7]. Although I made the comparison for both solid state and solution measurements, only the solution spectra are compared here, as calculations for individual molecules are more comparable to solution spectra mainly consisting of non-aggregated molecules. Although the absolute values of ϵ_2 calculated by TDDFT are larger than the experimentally measured ones, they are of the same order of magnitude and the quantitative trends when comparing IDTBR and IDFBR are in good agreement - the lowest energy absorption peak of IDTBR is red-shifted by about 0.5 eV compared to IDFBR, and the peak height of IDTBR is a little over 50% higher than that of IDFBR for both experiment and calculation.

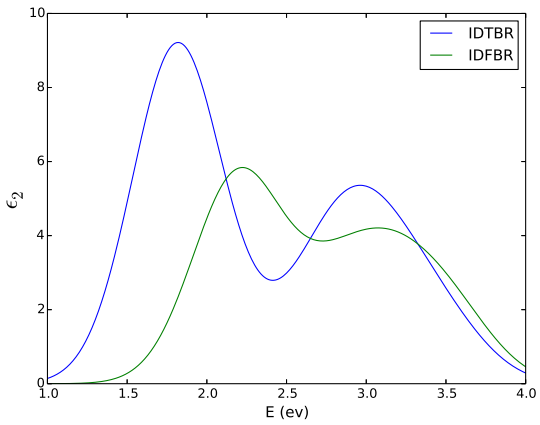

(a) calculation

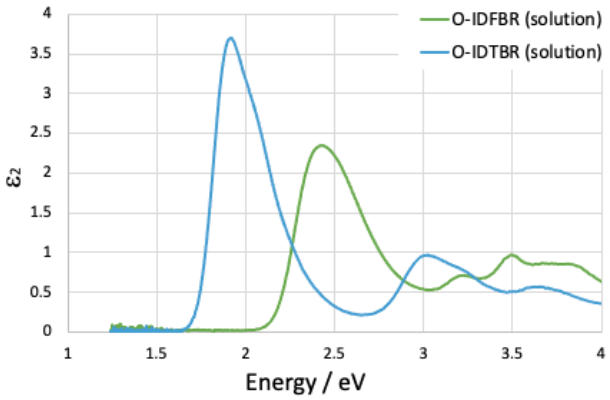

(b) experiment

Figure 4.13: (a) Optical spectra of optimised IDTBR and IDFBR, calculated using TDDFT (CAM-B3LYP functional and cc-pVDZ basis states). (b)

Finally, in order to comment on the relationship between the geometrical structures of the molecules and their optical spectra, figure 4.14 takes a closer look at the lowest energy absorption peaks plotted in 4.13a. As stated earlier, the key difference in geometry between the two molecules is that IDTBR is planar, whereas IDFBR is twisted. In order to evaluate how large a role the difference in planarity plays in their optical properties, I have also included the optical properties of planarised IDFBR in figure 4.14.

The increase in transition energies E_1 (top panel) and decrease in oscillator strength f_1 (bottom

panel) is a different way of visualising the shift and change in height of the first absorption peak in figure 4.13a. As the oscillator strength is proportional to the transition energy and the transition dipole strength $|\mu_1|^2$ (middle panel), we can see that the decrease in the oscillator strength going from IDTBR to IDFBR is due to the significant decrease in transition dipole strength, and only slightly offset by the increase in transition energy. We can also observe that for all three quantities the values for planarised IDFBR lies between those of the optimised IDTBR and IDFBR structures, indicating that the planarity of IDTBR is only part of the explanation why IDTBR absorbs more strongly and at a lower energies.

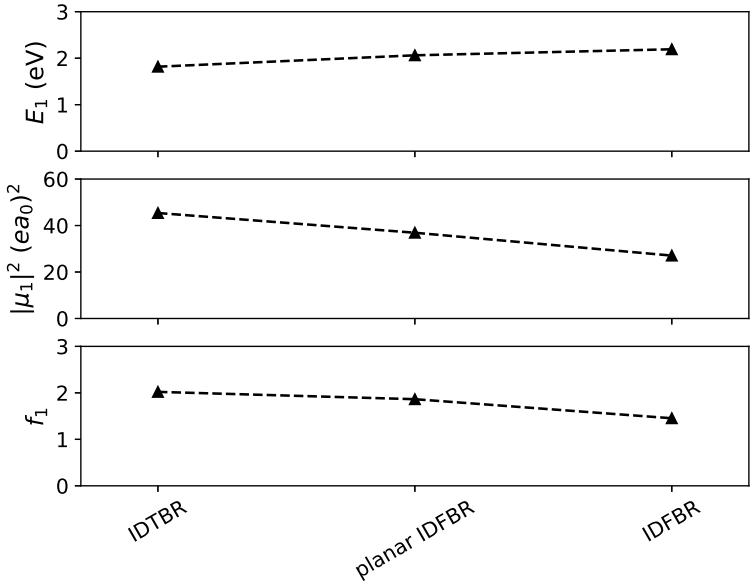

Figure 4.14: Transition energy (E_1), transition dipole strength ($|\mu_1|^2$) and oscillator strength (f_1) of the first excited state of freely optimised IDTBR, IDFBR, as well as planarised IDFBR, calculated using TDDFT (CAM-B3LYP functional and cc-pVDZ basis states).

4.4 Discussion and conclusions

I presented two case studies on how TDDFT can be used to investigate the conformation dependent absorption strength of polythiophene and the two small molecules IDTBR and IDFBR. It was shown that the oscillator strengths of these materials are very sensitive to small changes in geometry, such as coplanarity or colinearity of neighbouring submolecule units.

The results presented in section 4.2 provide some insights into how varying the oligomer length

and conformation of thiophenes affects their optical absorption properties. However, these insights are only valid for individual oligomer chains, and are not easily transferable to more realistic systems of polymer and acceptor molecule blends, which exhibit complex morphologies. In order to build models for the optical properties of organic semiconductors that take account of the large variation in conformations that is present in practice, it is necessary to perform excited state calculations on large numbers of macromolecules in different conformations.[15] This would quickly exceed the length scales that can be accessed practically by TDDFT.

A second factor that impacts the conformation and hence the optical properties of materials is the chemical structure of the components. I explored this by modelling the different optical properties of the chemically similar pair of molecules, IDTBR and IDFBR. The results presented in section 4.3 showed that the difference in the optical properties of IDTBR and IDFBR is partially due to the difference in coplanarity of the submolecule units and partly due to the chemical structure of the central IDF or IDT unit. For example, when comparing the electronic band gaps between the IDTBR, planarised IDFBR and the freely optimised IDFBR, only 38% of the difference can be directly attributed to the difference in planarity. If our goal is to design new high performing acceptor molecules, we need a modelling framework that is capable of incorporating changes in geometry and changes in the intramolecular interactions that result from specific chemical structure. A coarse-grained model in the basis of the submolecule units could give more insights by linking the submolecule on-site energies, transfer integrals and Coulomb interactions to the resultant optical absorption properties, whilst still retaining chemical information through the coarse-grained parameters of the sub-molecular units.

DFT is a good tool to determine the minimum energy conformation of individual polymer fragments or small molecules, which can then be used to estimate the material's optical properties and compare it against other materials. However, in practice a large variety of conformations of molecule or polymer chain may be present in a solid film resulting from the processing conditions, as well as presence of other blend components and phases. In order to address the challenges of TDDFT and gain more insights into what drives the optical absorption properties of conjugated polymers, I am developing a modelling framework that uses a model Hamiltonian in a coarse-grained basis and obtains parameters from *ab initio* calculations, specifically using

the Configuration Interaction Singles method in a basis of Wannier functions. In the next chapter I introduce the approach and its computational implementation using polyacetylene as an example. Finally, in chapter 6 I will present the results of applying this approach to study the conformation dependence of the optical properties of the two polymers - varying the bond length alternation in polyacetylene and the dihedral angle in polythiophene.

Bibliography

[1] Jenny Clark, Carlos Silva, Richard H. Friend, and Frank C. Spano. Role of intermolecular coupling in the photophysics of disordered organic semiconductors: Aggregate emission in regioregular polythiophene. 98(20), May 2007.

[2] Francis Paquin, Hajime Yamagata, Nicholas J. Hestand, Maciej Sakowicz, Nicolas Bérubé, Michel Côté, Luke X. Reynolds, Saif A. Haque, Natalie Stingelin, Frank C. Spano, and Carlos Silva. Two-dimensional spatial coherence of excitons in semicrystalline polymeric semiconductors: Effect of molecular weight. 88(15), October 2013.

[3] Mariano Campoy-Quiles, Toby Ferenczi, Tiziano Agostinelli, Pablo G. Etchegoin, Youngkyoo Kim, Thomas D. Anthopoulos, Paul N. Stavrinou, Donal D. C. Bradley, and Jenny Nelson. Morphology evolution via self-organization and lateral and vertical diffusion in polymer:fullerene solar cell blends. 7(2):158–164, January 2008.

[4] Wing C. Tsoi, Patrick G. Nicholson, Jong Soo Kim, Debdulal Roy, Tim L. Burnett, Craig E. Murphy, Jenny Nelson, Donal D. C. Bradley, Ji-Seon Kim, and Fernando A. Castro. Surface and subsurface morphology of operating nanowire:fullerene solar cells revealed by photoconductive-AFM. *Energy Environ. Sci.*, 4, 2011.

[5] Ardalan Armin, Wei Li, Oskar J Sandberg, Zuo Xiao, Liming Ding, Jenny Nelson, Dieter Neher, Koen Vandewal, Safa Shoaee, Tao Wang, et al. A history and perspective of non-fullerene electron acceptors for organic solar cells. *Advanced Energy Materials*, page 2003570, 2021.

[6] G. Forti, A. Nitti, P. Osw, G. Bianchi, R. Po, and D. Pasini. Recent advances in non-fullerene acceptors of IDIC/ITIC families for bulk-heterojunction organic solar cells. *Int. J. Mol. Sci.*, 21, 2020.

[7] Elham Rezasoltani, Anne AY Guilbert, Jun Yan, Xabier Rodriguez-Martinez, Mohammed Azzouzi, Flurin Eisner, Sachetan M Tuladhar, Zeinab Hamid, Andrew Wadsworth, Iain McCulloch, et al. Correlating the phase behavior with the device performance in binary poly-3-hexylthiophene: Nonfullerene acceptor blend using optical probes of the microstructure. *Chemistry of Materials*, 32(19):8294–8305, 2020.

[8] M. Campoy-Quiles, J. Nelson, D.D.C. Bradley, and P.G. Etchegoin. Dimensionality of electronic excitations in organic semiconductors: A dielectric function approach. *Phys. Rev. B*, 76, 2007.

[9] A.A.Y. Guilbert, M. Schmidt, A. Bruno, J. Yao, S. King, S.M Tuladhar, T. Kirchartz, M.I. Alonso, A.R. Goni, N. Stingelin, S.A. Haque, M. Campoy-Quiles, and J. Nelson. Spectroscopic evaluation of mixing and crystallinity of fullerenes in bulk heterojunctions. *Adv. Funct. Mater.*, 24:6972–6980, 2014.

[10] Felix Peter Vinzenz Koch. *Synthesis and Physical Chemistry of Poly(3-hexylthiophene) a "Monomer-up Approach"*. Thesis, ETH Zurich, 2013.

[11] N. J. Hestand and F. C. Spano. The effect of chain bending on the photophysical properties of conjugated polymers. *J Phys Chem B*, 118(28):8352–63, 2014.

[12] M. S. Vezie, S. Few, I. Meager, G. Pieridou, B. Dorling, R. S. Ashraf, A. R. Goni, H. Bronstein, I. McCulloch, S. C. Hayes, M. Campoy-Quiles, and J. Nelson. Exploring the origin of high optical absorption in conjugated polymers. *Nat Mater*, 2016.

[13] Sarah Holliday, Raja Shahid Ashraf, Andrew Wadsworth, Derya Baran, Syeda Amber Yousaf, Christian B Nielsen, Ching-Hong Tan, Stoichko D Dimitrov, Zhengrong Shang, Nicola Gasparini, et al. High-efficiency and air-stable P3HT-based polymer solar cells with a new non-fullerene acceptor. *Nature communications*, 7(1):1–11, 2016.

[14] Derya Baran, Raja Shahid Ashraf, David A Hanifi, Maged Abdelsamie, Nicola Gasparini, Jason A Röhr, Sarah Holliday, Andrew Wadsworth, Sarah Lockett, Marios Neophytou, et al. Reducing the efficiency–stability–cost gap of organic photovoltaics with highly efficient and stable small molecule acceptor ternary solar cells. *Nature materials*, 16(3):363–369, 2017.

[15] Nicholas E. Jackson, Brett M. Savoie, Kevin L. Kohlstedt, Tobin J. Marks, Lin X. Chen, and Mark A. Ratner. Structural and conformational dispersion in the rational design of conjugated polymers. *Macromolecules*, 47(3):987–992, January 2014.

Chapter 5

Calculating optical properties using W-CIS

5.1 Introduction

Developing computationally efficient methods to model the electronic and optical properties of conjugated polymers is a challenge that has been tackled by many groups over many decades. I have reviewed several approaches in chapter 2 and I will only highlight some of the more recent work here. For example, Barford et al. use a Frenkel exciton basis Hamiltonian to define a two-particle model[1], which is then applied to define chromophores[2][3] in order to study exciton diffusion. A recent review [4] discusses more broadly how their approach can be used to study exciton dynamics, as well as the role of electron-phonon coupling to correctly account for ultrafast processes. These studies use a semi-empirical Hamiltonian, where parameters are obtained by fitting to experimental spectra, and they typically take conformational effects into account by varying the excitonic coupling between monomer units as a Gaussian variable[3]. As outlined in chapter 2, the focus of this thesis is the first step in the photogeneration process - the optical absorption of a photon generating an exciton. Therefore, the modelling framework presented in this chapter is used to calculate only the electronic transitions contributing to the absorption spectrum. However, the main advantage of the approach presented here is that I

obtain the model Hamiltonian matrix elements from *ab initio* calculations, meaning that the model is capable of incorporating changes in geometry, as well as changes in the intramolecular interactions that results from specific chemical structure.

This chapter introduces the Wannier function basis Configuration Interaction Singles (W-CIS) method. As described in more detail in section 3.3.1, the method uses an effective Hamiltonian in a coarse-grained basis, but all the parameters are obtained from first principles calculations. To demonstrate the capabilities of the W-CIS method, I am using it to calculate the excited states for oligoacetylenes of different lengths. Oligomers of polyacetylene were chosen, as it is the simplest conjugated polymer and has been widely studied in the literature.

This chapter covers the following topics:

- section 5.2 contains a detailed description of the computational implementation I follow for the W-CIS method,
- section 5.3 presents the calculated W-CIS Hamiltonian parameters for polyacetylene,
- section 5.4 presents the optical absorption properties of oligoacetylenes calculated using the W-CIS method,
- and section 5.5 shows how the W-CIS approach can be used to characterise exciton delocalisation.

5.2 Computational Implementation

This section contains a description of the computational implementation in which I use first principles calculations on polyacetylene to obtain all the necessary W-CIS Hamiltonian parameters, and diagonalise the Hamiltonian to calculate the optical properties of finite oligomers.

In order to calculate all the parameters I developed a modelling framework, which combines the scientific codes Quantum ESPRESSO[5][6], BerkeleyGW[7][8] and Wannier90[9], as well as original code development to perform integrals between Wannier functions. Additionally, a

series of python scripts were developed that perform the diagonalisation of the Hamiltonian and transforms the output eigenvalues and eigenvectors into a range of optical and electronic properties. The code and associated pre-processing and post-processing scripts can be found in the `github.com/ImperialCollegeLondon/wannier-cis` repository. All calculations in this thesis were performed using Imperial College London's Research Computing Centre[10].

5.2.1 Method overview

The theoretical background of the W-CIS method is described in more detail in section 3.3.1, only the key equations are summarised below.

The W-CIS Hamiltonian matrix $H_{iji'j'}$ can be written as a sum of the one-particle operator matrix $F_{iji'j'}$ and the two-particle operator matrix $V_{iji'j'}$

$$\begin{aligned} H_{iji'j'} &= \sum_{ij}^{N} [F_{iji'j'} + V_{iji'j'}] \\ F_{iji'j'} &= [\epsilon^c - \epsilon^v]\delta_{ii'}\delta_{jj'} + t^c(s)\delta_{jj'} - t^v(s)\delta_{ii'} \\ V_{iji'j'} &= [-U^d(s) + 2U^x(s)]\delta_{ii'}\delta_{jj'} \end{aligned} \tag{5.1}$$

where i, i' are the electron coordinates, j, j' are the hole coordinates, N is the number of monomers and s denotes the separation between particles. Thus, the required parameters are the electron and hole on-site energies ϵ^c, ϵ^v and transfer integrals $t^c(s)$, $t^v(s)$ for the single-particle operator and the direct and exchange Coulomb interaction energies $U^d(s)$, $U^x(s)$ for the two-particle operator. After all the Hamiltonian parameters have been calculated I solve the eigenvalue problem

$$\sum_{i'j'}^{N} H_{ij,i'j'} A^n_{i'j'} = E_n A^n_{ij}, \tag{5.2}$$

where E_n is the transition energy of the n-th excited state, and A^n_{ij} are the eigenvector coeffi-

cients. The transition dipole moment of the n-th excited state $\boldsymbol{\mu}_n$ is then calculated as

$$\boldsymbol{\mu}_n = \sum_{ij} A_{ij}^n \boldsymbol{\mu}(s), \tag{5.3}$$

where $\boldsymbol{\mu}(s)$ is the intermonomer transition dipole moment.

The key contribution of this thesis is the modelling framework developed to obtain the parameters for this model Hamiltonian from *ab initio* calculations. Section 5.2.2 describes how to obtain the Wannier functions that are used to construct the basis of the model Hamiltonian, as well as their associated on-site energies ϵ^v, ϵ^c and transfer integrals $t^c(s)$, $t^v(s)$. Section 5.2.3 then describes how the obtained Wannier functions are used to calculate the Coulomb integrals $U^d(s)$, $U^x(s)$ and intermonomer transition dipole moments $\boldsymbol{\mu}(s)$.

5.2.2 Obtaining maximally localised Wannier functions

This section outlines the details of the electronic structure calculations performed to obtain the maximally localised Wannier functions (WFs), which are used to describe the HOMO and LUMO of the monomer in a polyacetylene chain. I first describe the theoretical details required for the electronic structure calculations and then provide practical instructions how these calculations can be run using the scripts and example input files prepared as part of this modelling framework.

Density-functional theory

First, I perform ab initio density-functional theory (DFT) calculations on an infinite polyacetylene. The unit cell consists of a single acetylene (C_2H_2), a polymer fragment of 5 units is depicted in figure 6.2b. I am using the QUANTUM ESPRESSO software package and employ a plane-wave basis with a cutoff of 80 Ry, the hybrid GAU-PBE exchange-correlation functional, SG15 optimized norm-conserving Vanderbilt pseudopotentials, and the calculations are performed using a $1 \times 1 \times 20$ k-point grid. First, the polymer's geometry was relaxed using

a 10^{-6} total energy and 10^{-5} force convergence threshold. The DFT band structure was then calculated using a 10^{-10} SCF convergence threshold. As can be seen in figure 5.1a, the band gap of polyacetylene is located at the edge of the first Brillouin zone corresponding to $k = \pi/a_0$.

The unit cell is set up such that the long axis is the z-axis, because in the next step when calculating the Hartree-Fock energies of the bands (described in the next section), the BerkeleyGW software package will use Coulomb potential truncation. When considering a one-dimensional system like a polymer, the keyword `cell_wire_truncation` must be chosen, which assumes that the z-axis is periodic, and the x- and y-axis are confined. More details on how to set up the DFT calculations can be found in the documentation and tutorials for the QUANTUM ESPRESSO software package, especially the input file descriptions for `pw.x` for performing the DFT calculations, and `pw2bgw.x` for preparing the input files for the next step using the BerkeleyGW software package.

Hartree-Fock energy correction

Formally, the W-CIS approach is based on the Hartree-Fock (HF) method and therefore the on-site energies, transfer integrals and Coulomb matrix elements should be evaluated using Hartree-Fock Wannier functions and band structures. However, self-consistent Hartree-Fock calculations on extended systems using a plane-wave basis are currently still numerically challenging. Therefore, I assume that the Hartree-Fock Bloch states $\psi^{HF}_{n\boldsymbol{k}}(\mathbf{r})$ (where n is a band index and $\boldsymbol{k}$ denotes the crystal momentum in the first Brillouin zone) are similar to the DFT states $\psi^{DFT}_{n\boldsymbol{k}}(\mathbf{r})$ and calculate the Hartree-Fock band structure $\epsilon^{HF}_{n\boldsymbol{k}}$ using a one-shot perturbation theory approach

$$\epsilon^{HF}_{n\boldsymbol{k}} = \epsilon^{DFT}_{n\boldsymbol{k}} + \langle \psi^{DFT}_{n\boldsymbol{k}} | \, \Sigma_{HF} - V_{xc} \, | \psi^{DFT}_{n\boldsymbol{k}} \rangle \,, \tag{5.4}$$

where $\epsilon^{DFT}_{n\boldsymbol{k}}$ denotes the DFT Kohn-Sham energies, V_{xc} is the PBE exchange-correlation potential and Σ^{HF} is the Hartree-Fock self-energy [8]. This calculation is carried out using the BerkeleyGW software package. The HF-corrected band structure is plotted alongside the DFT band structure in figure 5.1a, it can be seen that the HF correction significantly increases the band gap from 1.67 eV to 7.51 eV and also increases the slope of the bands.

Wannierisation

Next, I transform the valence and conduction bands into maximally localised WFs for the HOMO and LUMO states of the monomer using the Wannier90 code. WFs are localised wavefunctions in real space built by superimposing Bloch functions of different $\boldsymbol{k}$, in the case where band n is separated by a gap from all other bands at all $\boldsymbol{k}$ its WF is given by

$$W_{\boldsymbol{R}}^{n}(\boldsymbol{r}) = \frac{V}{(2\pi)^3}\int_{BZ} d\boldsymbol{k} e^{-i\boldsymbol{k}\cdot\boldsymbol{R}}\psi_{n\boldsymbol{k}}^{DFT}(\boldsymbol{r}), \tag{5.5}$$

the integral is over the whole Brillouin zone (BZ), V is the unit cell volume and $\boldsymbol{R}$ is the real space lattice vector. The phase factor $e^{-i\boldsymbol{k}\cdot\boldsymbol{R}}$ translates the WF by $\boldsymbol{R}$ thus generating several identical WFs located in different units of the real space supercell. This enables the evaluation of the W-CIS parameters at different single-particle separations s. A more detailed account of maximally localised WFs is given by Marzari et al. (2012)[11].

The LUMO WF W^c was obtained by wannierising one conduction band and specifying a frozen energy window between $-1.2\ eV$ and $1.2\ eV$, and the HOMO WF W^v was obtained by wannierising the three highest energy valence bands $n = 3-5$. Figure 6.2b shows that both are highly localized. The corresponding on-site energies ϵ^c, ϵ^v and transfer integrals $t^c(s)$, $t^v(s)$ are extracted from the Wannier-transformed HF Hamiltonian. As I am using a $20 \times 1 \times 1$ k-point grid, I obtain 20 WFs per band, which results in 10 unique transfer integral values due to symmetry. To verify the obtained parameter values (listed in table 5.2) I compare the HOMO and LUMO WF bands to the HF bands in figure 5.1a. The WF bands are given by

$$\epsilon^{WF}(k) = \epsilon^{c,v} + \sum_{s\neq 0}^{s_{max}} 2t^{c,v}(s)cos(ska), \tag{5.6}$$

where a is the unit cell parameter. Note that the two plotted bands accurately reproduce the HOMO and LUMO HF bands throughout the first BZ.

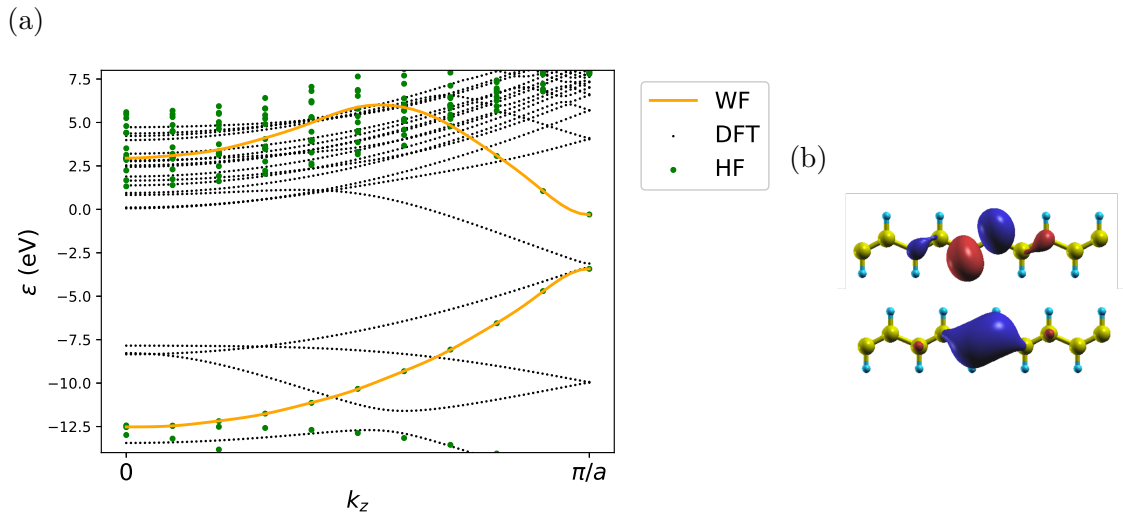

Figure 5.1: (a) DFT, Hartree-Fock and WF bands of polyacetylene, (b) maximally localized Wannier functions of monomer LUMO orbital (W^c) and HOMO orbital (W^v) for polyacetylene.

Computational implementation

Step by step instructions on how to run the calculations described above using the scripts and example input files prepared for this modelling framework can be found here

`github.com/ImperialCollegeLondon/wannier-cis/tree/master/wannierisation`.

Figure 5.2 shows how the three codes are used together to perform the wannierisation by visualising the commands used in the `example_input/qe_hf_w90.sh` script that can be found in the repository linked above. Details on the input and output files and more guidance on running the calculations can be found in the documentation and tutorials of the three codes.

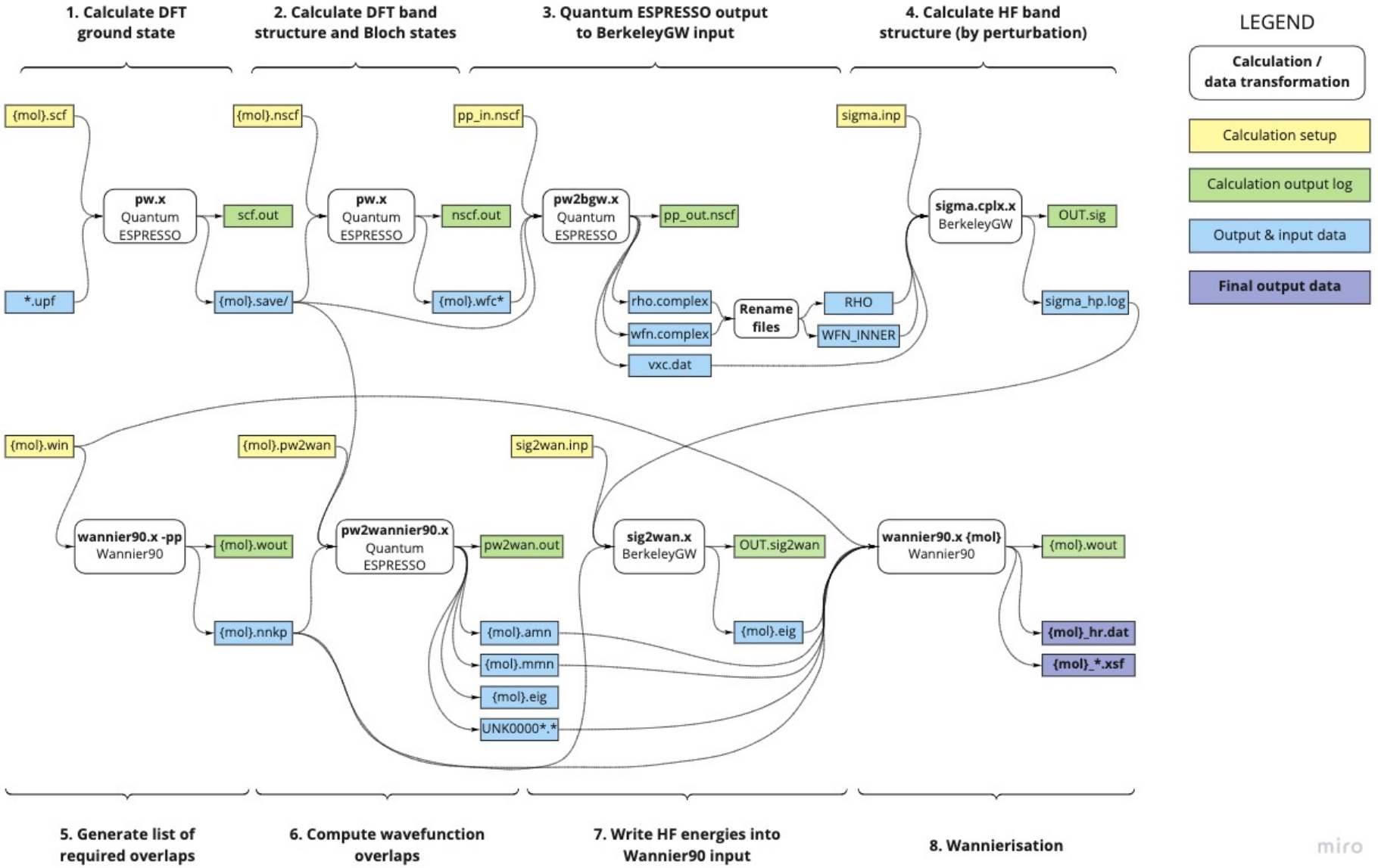

Figure 5.2: Visualisation of the commands used in the script that is used to perform the wannierisation step of the modelling framework presented in this chapter. The white boxes contain the specific executable used in each step, as well as which software package it is from. The yellow boxes show the input files, and the purple boxes show the final output files containing all the necessary data for the next steps.

5.2.3 Wannier function integrals

The final parameters that are needed for the W-CIS Hamiltonian matrix are the direct and exchange Coulomb interaction energies $U^d(s)$, $U^x(s)$, which can be calculated as integrals on a real space grid

$$U^d(s) = \int d^3r \int d^3r' W_i^c(\mathbf{r}) W_{i+s}^v(\mathbf{r}') \frac{1}{|\mathbf{r}-\mathbf{r}'|} W_i^c(\mathbf{r}) W_{i+s}^v(\mathbf{r}'), \tag{5.7}$$

$$U^x(s) = \int d^3r \int d^3r' W_i^c(\mathbf{r}) W_{i+s}^v(\mathbf{r}') \frac{1}{|\mathbf{r}-\mathbf{r}'|} W_{i+s}^v(\mathbf{r}) W_i^c(\mathbf{r}'). \tag{5.8}$$

Additionally, in order to calculate the absorption strength once the W-CIS Hamiltonian is diagonalised, the intermonomer transition dipole moments $\boldsymbol{\mu}(s)$ are required, which can be calculated as follows

$$\boldsymbol{\mu}(s) = -e \int d^3r W_i^c(\boldsymbol{r}) \boldsymbol{r} W_{i+s}^v(\boldsymbol{r}). \tag{5.9}$$

I calculated these parameters by writing a custom C++ code that reads in the WFs obtained from wannier90 and performs numerical integration on a real space Cartesian grid. The resulting values are listed in table 5.2. Calculating the Coulomb integrals numerically is not straightforward due to the singularity at $\boldsymbol{r} = \boldsymbol{r'}$, it is avoided by using pre-computed analytical values for the cubic volume elements at and surrounding the singularity following the example of Larsen and Schwartz [12]. The code and accompanying step by step instructions on how to use it can be found in the following folder

`github.com/ImperialCollegeLondon/wannier-cis/tree/master/wf_integrals`.

Figure 5.3 shows how the Wannier functions obtained in the previous step are used to calculate a Coulomb integral by visualising the functions used in the `core_integration_code/main.cpp` code that can be found in the repository linked above. Table 5.1 contains descriptions of the input arguments of the Wannier function integration code. Example scripts that assign values to these input arguments and execute the code can be found in the `example_input` folder.

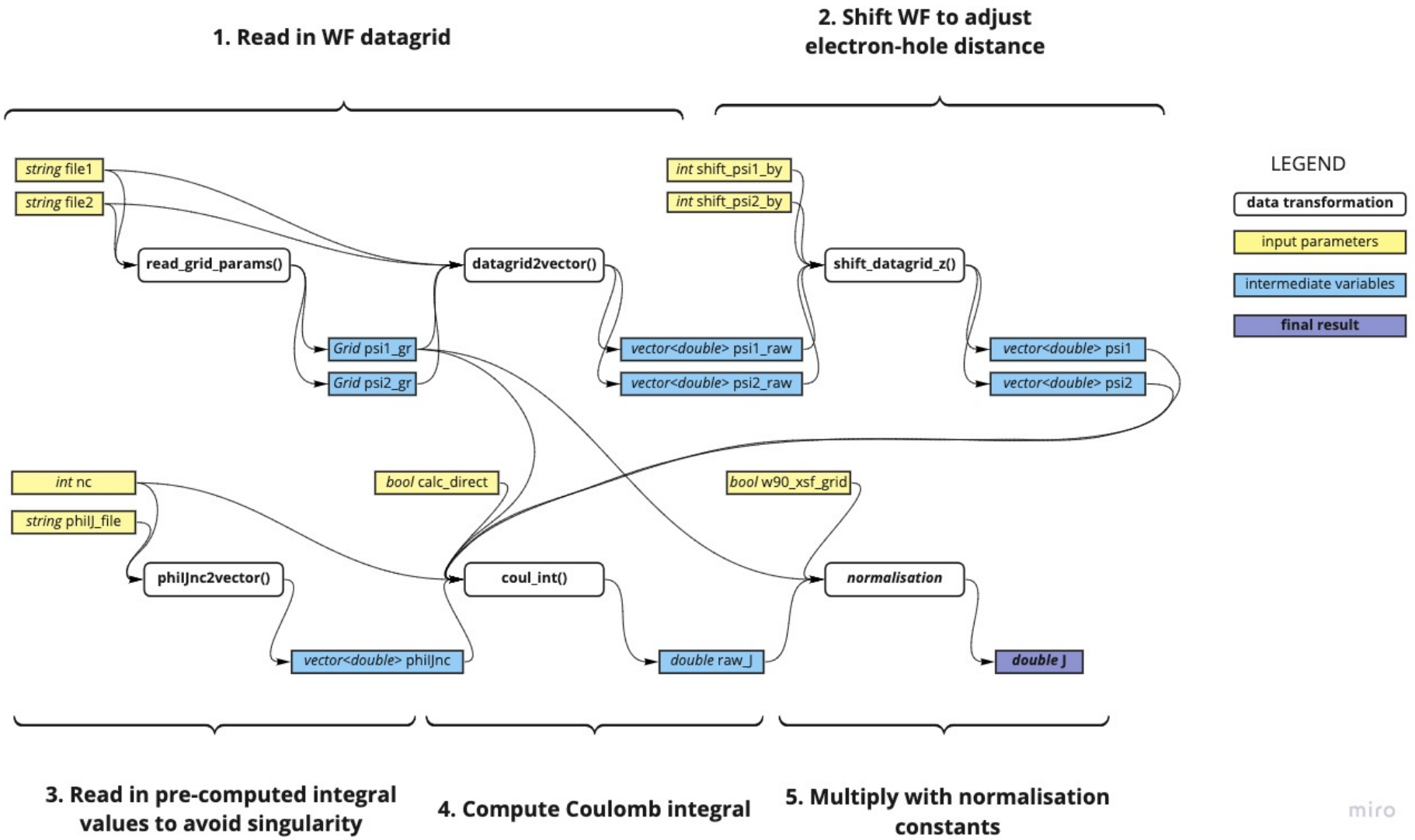

Figure 5.3: Visualisation of the commands used in the script that performs integration between Wannier functions. The white boxes contain the names of the functions defined in the C++ code, the yellow boxes show the input parameters that are defined in the input files, and the purple box shows the final result variable which is written in the output file.

Input	Type	Description
file1	string	Filepath to a wannier function datagrid in xsf format, note that only the 3D datagrid section should be in the file - the first line of the input file has to be the number of data-points in each direction
file2	string	Filepath to a wannier function datagrid in xsf format, note that only the 3D datagrid section should be in the file - the first line of the input file has to be the number of data-points in each direction
Ncells	integer	Number of unit cells in the wannier function supercell (same as the number of k-points used in the DFT calculation)
w90_xsf_grid	boolean	Boolean indicating if the xsf grid is an output of wannier90, this is necessary to apply the appropriate normalisation
shift_psi1_by	integer	Number of unit cells the wannier function read in from "file1" should be shifted along the z axis before integration
shift_psi2_by	integer	Number of unit cells the wannier function read in from "file2" should be shifted along the z axis before integration
calc_direct	boolean	Boolean indicating whether the direct Coulomb integral (equation 5.7) should be computed
calc_exchange	boolean	Boolean indicating whether the exchange Coulomb integral (equation 5.8) should be computed
calc_other	boolean	Boolean indicating whether the overlap integrals and transition dipole moments (equation 5.9) should be computed
nc	integer	Number of grid points around the singularity that should be computed using a pre-computed value for 1/r
phiIJ_file	string	Pre-computed analytical values for 1/r, see [12] for more details

Table 5.1: Descriptions of the input arguments used in the Wannier function integration code, these correspond to the yellow boxes in figure 5.3.

5.2.4 Calculating optical properties

Finally, I solve the W-CIS eigenvalue problem (equation 5.2) by diagonalising the Hamiltonian matrix using a custom Python code using the linear algebra functions of the NumPy library. The core functions constructing and solving the Hamiltonian can be found in the `hamiltonian_utils.py` file in this folder

`github.com/ImperialCollegeLondon/wannier-cis/tree/master/solve_hamiltonian`

This gives the transition energies E_n and the eigenvector coefficients A_{ij}^n that can be used to calculate the transition dipole moment $\boldsymbol{\mu}_n$ (equation 5.3). The oscillator strength is then calculated as

$$f_n = \frac{2}{3} E_n |\boldsymbol{\mu}_n|^2. \tag{5.10}$$

The transition energies, transition dipole moment and oscillator strength are the three key optical properties that will be plotted in sections 5.4 and 5.4.3. Post-processing scripts to plot these and other quantities can also be found in the github folder linked above.

5.3 Ab initio parameters of polyacetylene

All the W-CIS parameters necessary to calculate the optical properties of oligoacetylenes are summarised in table 5.2. The table only includes values for $s \leq 8$, as the calculated optical properties have converged when 8 nearest neighbour interactions are included (figure 5.8).

s	ϵ^c (eV)	t^c (eV)	ϵ^v (eV)	t^v (eV)	U^d (eV)	U^x (eV)	μ_x (ea_0)	μ_y (ea_0)	μ_z (ea_0)
0	3.77	-	-9.45	-	7.69	1.73	$3{\cdot}10^{-4}$	0.73	-1.16
1	-	0.31	-	-1.92	5.06	0.49	$3{\cdot}10^{-4}$	0.06	1.11
2	-	-1.07	-	0.54	3.10	0.17	$-8{\cdot}10^{-4}$	-0.07	-1.03
3	-	0.41	-	-0.24	2.11	0.07	$9{\cdot}10^{-4}$	-0.05	0.94
4	-	-0.07	-	0.13	1.61	0.03	$-2{\cdot}10^{-3}$	-0.04	-0.85
5	-	0.04	-	-0.07	1.31	0.03	$2{\cdot}10^{-3}$	-0.04	0.75
6	-	-0.05	-	0.05	1.11	0.01	$-3{\cdot}10^{-3}$	-0.05	-0.62
7	-	0.04	-	-0.03	0.97	0.01	$2{\cdot}10^{-3}$	-0.04	0.48
8	-	-0.02	-	0.02	0.85	0.01	$4{\cdot}10^{-3}$	-0.05	-0.30

Table 5.2: W-CIS parameters for different single particle separations s: on-site energies ϵ^c, ϵ^v, transfer integrals $t^c(s)$, $t^v(s)$, direct and exchange Coulomb integrals $U^d(s)$, $U^x(s)$ and the components of the intermonomer transition dipole moment $\mu_x(s)$, $\mu_y(s)$, $\mu_z(s)$.

5.3.1 Transfer integrals

The electron and hole transfer integrals represent the electronic coupling between single particle WFs and are off-diagonal terms in the W-CIS Hamiltonian matrix (equation 5.1). They determine the energies of the oligomer's HOMO and LUMO and thus the band gap, which directly affects the transition energy.

Figure 5.4 plots the absolute values of the electron and hole transfer integrals. Both have decayed to near zero when the particles are 4 units apart, which corresponds to about 19 a_0. The hole's transfer integral t_s^v decays nearly exponentially, whereas the electron's transfer integral t_s^c has a significant jump from $s = 1$ to $s = 2$. The irregular decay of the electronic transfer integral can be explained by looking at the changing slope of the lowest conduction band as plotted in figure 5.1a.

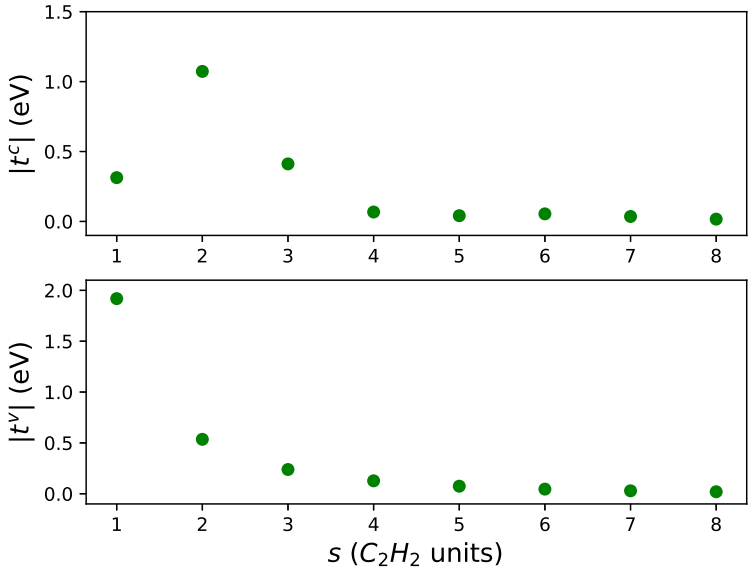

Figure 5.4: Absolute values of the electron (top) and hole (bottom) transfer integrals as a function of particle separation s.

5.3.2 Coulomb interaction

The electron-hole Coulomb interaction energies are diagonal terms in the W-CIS Hamiltonian matrix (equation 5.1) and directly affect the oligomer transition energies by altering the band gap.

The Coulomb interaction energies calculated as WF integrals are plotted as green circles in figure 5.5. They are comparable to commonly used approximations for the Coulomb energy: for the direct Coulomb interaction U^d I have plotted the interaction energy of two point charges (s^{-1}), as well as a Mataga type decay fitted to the WF integral values according to

$$U^d_{Mataga}(s) = U^d(0)(1 + s/s_0)^{-1}, \tag{5.11}$$

and for the exchange Coulomb interaction I have plotted an exponential decay fitted to the WF integral values according to

$$U^x_{exp}(s) = U^x(0)exp(-s/s_0). \tag{5.12}$$

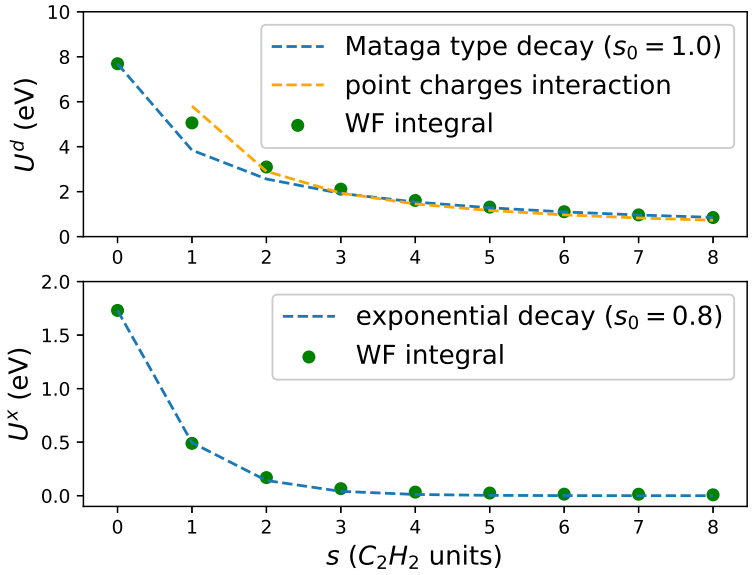

Figure 5.5: (top) Direct Coulomb interaction energies calculated as WF integrals, a fitted Mataga-type decay and the Coulomb interaction energy of two point charges, and (bottom) exchange Coulomb interaction energies calculated as WF integrals and a fitted exponential decay.

5.3.3 Transition dipole moments

The intermonomer transition dipole moments are used to calculate the absorption strength of the excited states once the exciton transition energies and eigenvector coefficients have been calculated (equation 5.3).

Figure 5.6 plots the intermonomer transition dipole moment magnitudes as a function of electron-hole separation s and its components parallel (z) and perpendicular (y) to the long axis. The x-component is not plotted as it is effectively zero (see table 5.2). The Frenkel exciton basis state ($s = 0$) has significant contributions from both the y and z components. The y-component drops to a nearly constant low value for all the charge-transfer exciton basis states ($s > 0$), whereas the z-component decays very slowly. The slow decay of the intermonomer transition dipole moment is the most surprising result from this work. This is the most important difference compared to other semi-empirical models which enables obtaining a superlinear trend in transition dipole strength with oligomer length, as will be discussed in section 5.4.3.

(a)

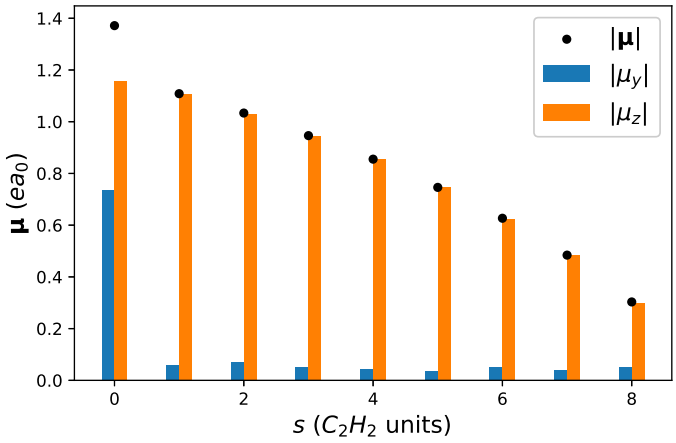

(b)

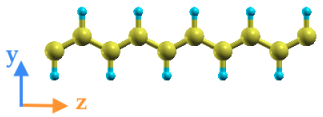

Figure 5.6: a) Intermonomer transition dipole moment magnitudes as a function of electron-hole separation s and the absolute values of its components parallel (z) and perpendicular (y) to the long axis and b) a diagram showing a polyacetylene fragment with 5 units with respect to the Cartesian axes.

5.4 Optical properties of oligoacetylenes

This section presents the optical absorption properties of oligoacetylenes calculated using the W-CIS method.

5.4.1 Optical absorption spectra

Before looking at detailed optical properties of oligoacetylenes, figure 5.7 plots the calculated optical spectra of oligomers of different lengths. The spectra are obtained by applying a Gaussian broadening with $\sigma = 0.25\ eV$ to electronic transition calculated by the W-CIS method. The monomer (N=1) only has one transition, but more than one transition can be observed for the longer oligomers. However, it can be seen that the lowest energy transition is distinctly strongest in oscillator strength for all oligomer lengths. The first transition is the closest in energy to the solar spectrum and strongest in oscillator strength, therefore it is the one that contributes the most to the performance of photovoltaic devices and thus is of most interest, so I look at its progression with oligomer length more closely in the next section.

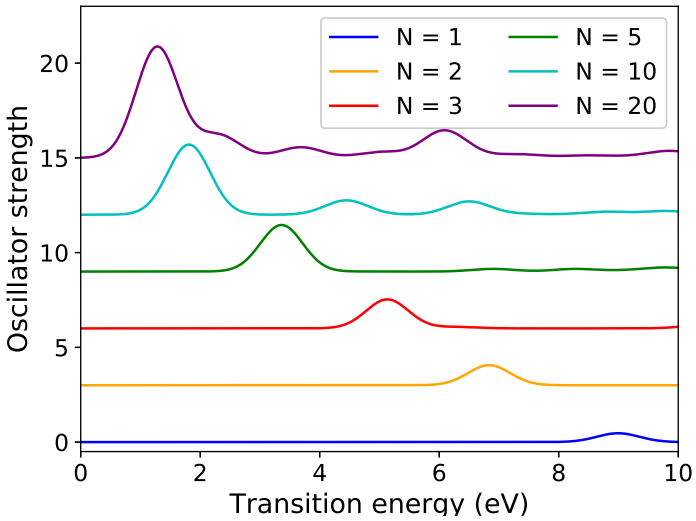

Figure 5.7: Optical absorption spectra showing the W-CIS calculated oscillator strength broadened with a Gaussian function of width $\sigma = 0.25\ eV$ as a function of transition energy for different length oligoacetylenes.

5.4.2 Convergence of optical properties

The transition energy (E_1), specific transition dipole strength ($|\boldsymbol{\mu}_1|^2/N$) and specific oscillator strength (f_1/N) of the first transition are plotted as a function of number of monomers in figure 5.8. The different colour curves show how the optical properties converge with the number of nearest neighbour interactions included in the W-CIS Hamiltonian, which is denoted by the maximum particle separation s_{max}. All the W-CIS results plotted in this chapter apart from this figure use $s_{max} = 8$.

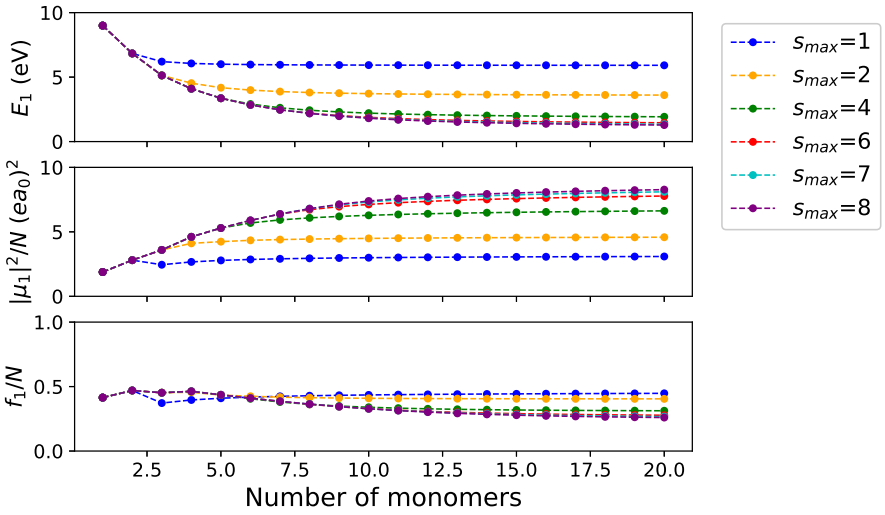

Figure 5.8: Transition energy (E_1), specific transition dipole strength ($|\boldsymbol{\mu}_1|^2/N$) and specific oscillator strength (f_1/N) of the first transition as a function of number of monomers calculated by W-CIS using a different nearest neighbour interaction cut-off indicated by the maximum electron hole separation s_{max}.

The plot shows a decreasing trend for the transition energy with oligomer length and an increasing trend for the specific transition dipole strength. As the oscillator strength is proportional to the product of the transition energy and the transition dipole strength, the trend in specific oscillator strength with oligomer length depends on these two quantities. In this case, the specific oscillator strength is first slightly increasing with oligomer length up to N=4 and then decreasing. These results will be compared with the results of *ab initio* CIS and with the semi-empirical Frenkel exciton model in the next section.

5.4.3 Method comparison

Figure 5.9 plots the transition energy (E_1), specific transition dipole strength ($|\boldsymbol{\mu}_1|^2/N$) and specific oscillator strength (f_1/N) of the first transition as a function of oligomer length as calculated by the W-CIS method (purple) and full *ab initio* CIS (blue). The W-CIS reproduces the full basis CIS results very well. The only difference in trends is the specific oscillator strength for short oligomers - this could be due to the fact that I am calculating properties of finite oligomers using parameters obtained from an infinite polymer chain.

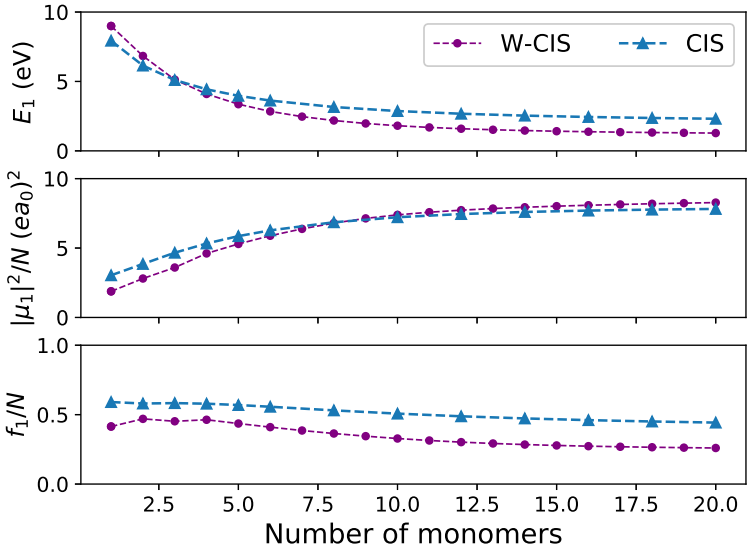

Figure 5.9: Transition energy, specific transition dipole strength and specific oscillator strength of different length oligoacetylenes calculated using W-CIS (purple) and CIS (blue).

I am also comparing the results of the W-CIS method to the widely used semi-empirical Frenkel exciton model to show that including charge transfer (CT) basis states are crucial in order to correctly calculate the transition dipole moments of organic molecules and polymers.

The Frenkel exciton (FE) Hamiltonian matrix is given by

$$H^{FE}_{i,i'} = \tilde{E}_i \delta_{ii'} + J_{ii'}. \tag{5.13}$$

For the FE on-site energies $\tilde{E}_i$ I use the Frenkel exciton energy as calculated from the W-CIS parameters

$$\tilde{E}_i = \epsilon^c - \epsilon^v - U^d(0) + 2U^x(0). \tag{5.14}$$

I approximate the FE transfer integral $J_{i,i'}$ by fitting the FE transition energies to those of W-CIS, as plotted in the top panel of figure 5.10.

Figure 5.10 plots the transition energy (E_1), specific transition dipole strength ($|\boldsymbol{\mu}_1|^2/N$) and specific oscillator strength (f_1/N) of the first transition as a function of oligomer length as calculated by the W-CIS method (purple) and the FE method (black).

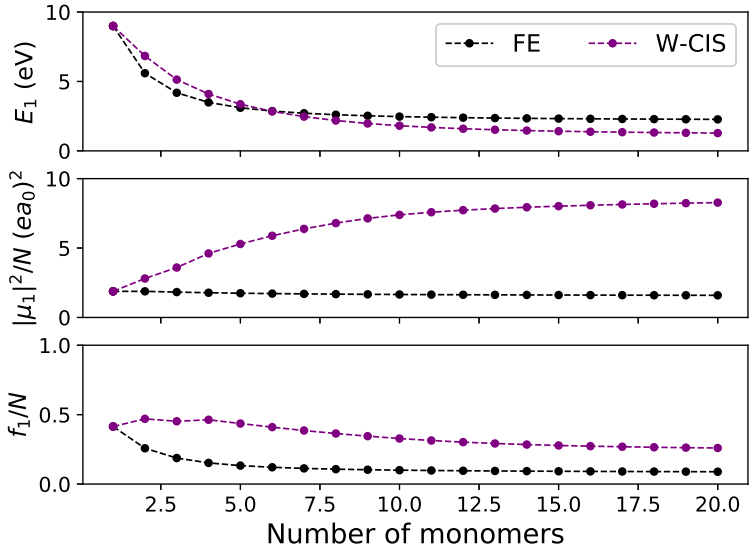

Figure 5.10: Transition energy, specific transition dipole strength and specific oscillator strength of different length oligoacetylenes calculated by W-CIS (purple) and FE (black).

The two methods give very different results for the oligomer length dependence of the specific transition dipole strength - it is slightly decreasing for the FE model, and increasing for the W-CIS method. As the oscillator strength is proportional to the product of the transition energy and the transition dipole strength, the trends in specific oscillator strength also differs between the two methods - the FE method shows a much more distinct decay with oligomer length. The observed difference in absorption strength trends between the W-CIS and FE methods can be explained by comparing the expressions for the transition dipole moment for the two methods. The FE model cannot give an increasing trend in specific transition dipole strength, as, for any N, it is a sum of transition dipole moments of the monomer weighted by the eigenvector coefficients

$$\boldsymbol{\mu}_n^{FE} = \sum_i B_i^n \boldsymbol{\mu}(0), \tag{5.15}$$

so the upper limit is a constant specific transition dipole strength. Whereas in the W-CIS case the transition dipole moment also has contributions from CT basis states

$$\boldsymbol{\mu}_n = \sum_i A_{i,i}^n \boldsymbol{\mu}(0) + \sum_{i,s\neq 0} A_{i,i+s}^n \boldsymbol{\mu}(s), \tag{5.16}$$

thus enabling the result of an increasing specific transition dipole strength and reproducing the trend from ab initio calculations (figure 5.9).

5.5 Exciton characterisation

Although the main purpose of this work is to enable the calculation of absorption strength as a function of polymer conformation at larger length scales, it can also be used to study the effect of structural disorder on exciton delocalisation as is done using similar model Hamiltonians, whose theoretical details and some findings are described in more detail in sections 2.2 and 2.4.3. The results shown in this section serve to demonstrate what additional information beyond optical spectra can be extracted from the results of the modelling framework presented in this chapter. A detailed analysis on how the obtained results compare to those of other model Hamiltonians is out of scope here, especially as many such studies also include the effects of electron-phonon coupling, which I am not considering here. I do, however, include some comparisons to work by Rohlfing and Louie using the GW-BSE method[13], as their approach also calculates the electronic excitations of polyacetylene, but their treatment of the electron-hole interactions is more rigorous than in the W-CIS approach presented in this chapter.

Figure 5.11 shows the electron distribution relative to the hole for the two lowest energy excitons of a long oligoacetylene. The first excited state (blue) is optically active with a high oscillator strength, whereas the second excited state (orange) is optically inactive with a zero oscillator strength. I plot these two states, as they can be directly compared to the exciton wave functions calculated using the GW-BSE approach by Rohlfing and Louie. They also find that the first excited state is optically active and the second is optically inactive, and the corresponding exciton wave functions have the same symmetry as the ones plotted here. However, they report different excitation energies (1.7 eV and 1.8 eV) and the exciton has a larger extent (the electron distribution decays to zero only between 15-20 C_2H_2 units). Even though the quantitative results differ, it is reassuring that the low-energy excitations calculated using W-CIS show qualitative agreement with the GW-BSE method, which rigorously treats electron-

hole interactions.

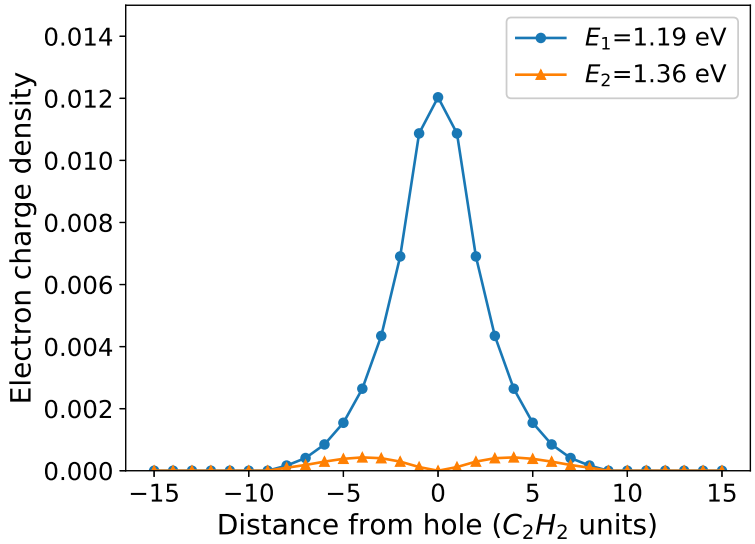

Figure 5.11: Electron charge density relative to the hole, which is fixed at the centre of an oligoacetylene with 31 C_2H_2 units.

Figure 5.12 characterises the strength of the electron and hole interaction of the lowest energy excitation by plotting the exciton binding energy, which is calculated as the difference between the band gap and the transition energy. The binding energy converges to about 2.7 eV at the polymer limit. This is much higher than the binding energy of 0.4 eV found by Rohlfing and Louie [13] using the GW-BSE approach.

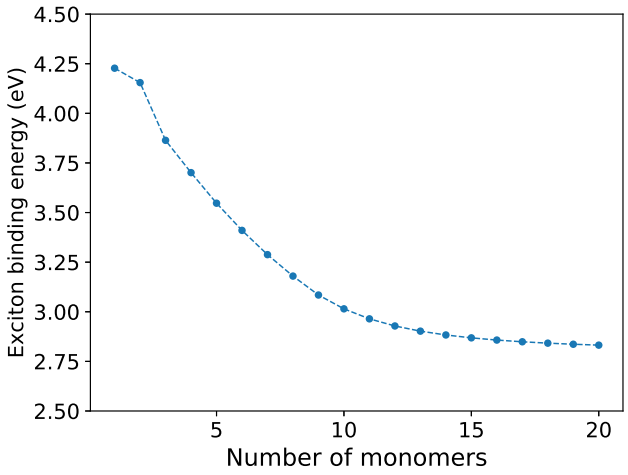

Figure 5.12: Exciton binding energy of different length oligoacetylenes calculated by W-CIS.

Figure 5.13a plots the fraction of different exciton basis states contributing to the first excited state of different length oligomers, this is calculated for each electron-hole separation s as the

sum of the squares of the relevant eigenvector elements $\sum_i |A^1_{i,i+s}|^2$. Additionally, the exciton radius $r_{exciton}$ is plotted in figure 5.13b, which is calculated using the fractions of basis states plotted in figure 5.13a and the relevant electron-hole separations s:

$$r_{exciton} = \sum_{i,s} s \cdot |A_{i,i+s}|^2. \tag{5.17}$$

The figure shows that the charge transfer (CT) basis states ($s > 0$) have a very high contribution to the first excited state, the Frenkel basis state ($s = 0$) contribution drops to about 20% for longer oligomers.

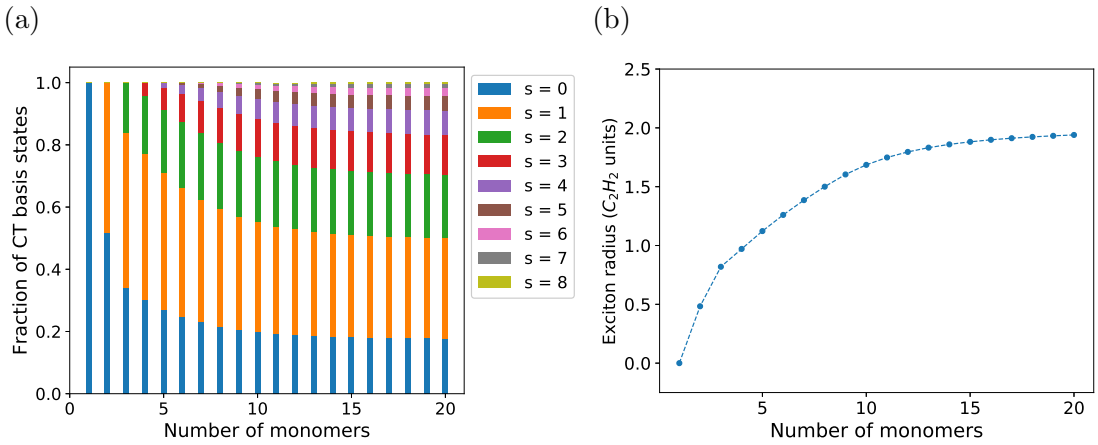

Figure 5.13: a) Contributions of exciton basis states with different electron-hole separations (s) to the first excited state of different length oligoacetylenes. b) Exciton radius of different length oligoacetylenes calculated by W-CIS, the value converges to $r_{eh} = 2.1$ at polymer limit.

5.6 Discussion and conclusions

I have presented the W-CIS approach - a coarse-grained method to calculate the optical absorption properties of conjugated oligomers that uses parameters obtained from ab initio calculations - by detailing the computational implementation (section 5.2), presenting the ab initio parameters of polyacetylene (section 5.3) and describing the resulting optical absorption properties of oligoacetylenes (section 5.4). Finally, I demonstrate that the modelling framework can also be used to extract information about exciton delocalisation (section 5.5).

The main advantage of the W-CIS approach presented in this chapter is that I obtain the model Hamiltonian matrix elements from *ab initio* calculations, meaning that the model is capable of incorporating changes in geometry, as well as changes in the intramolecular interactions that results from specific chemical structure. The importance of this was demonstrated in chapter 4 by presenting two case studies on how TDDFT can be used to investigate the conformation dependent absorption strength of polymers and small molecules, and concluding that these findings were not enough to explain the experimentally observed structure-property relationships. In chapter 6 I will apply W-CIS to study the effect of conformational changes on the optical absorption spectra of two polymers - bond length alteration in polyacetylene and dihedral angles in polythiophene - and link the observed effects on the optical properties to changes in the underlying electronic intermonomer interactions.

As mentioned earlier, I also presented how this approach can be used to extract information on exciton delocalisation. If the current model was extended to also incorporate electron-phonon coupling following examples by Karabunarliev and Bittner[14] or Barford et al.[4], it could also be applied to a wider range of mechanisms within the photocurrent generation process outlined in section 2.2.

Bibliography

[1] W. Barford. Excitons in conjugated polymers: a tale of two particles. *J Phys Chem A*, 117(13):2665–71, 2013.

[2] W. Barford and M. Marcus. Theory of optical transitions in conjugated polymers. I. Ideal systems. *J Chem Phys*, 141(16):164101, 2014.

[3] M. Marcus, O. R. Tozer, and W. Barford. Theory of optical transitions in conjugated polymers. II. Real systems. *J Chem Phys*, 141(16):164102, 2014.

[4] William Barford. Exciton dynamics in conjugated polymer systems. *Frontiers in Physics*, 10, 2022.

[5] Paolo Giannozzi, Stefano Baroni, Nicola Bonini, Matteo Calandra, Roberto Car, Carlo Cavazzoni, Davide Ceresoli, Guido L Chiarotti, Matteo Cococcioni, Ismaila Dabo, Andrea Dal Corso, Stefano de Gironcoli, Stefano Fabris, Guido Fratesi, Ralph Gebauer, Uwe Gerstmann, Christos Gougoussis, Anton Kokalj, Michele Lazzeri, Layla Martin-Samos, Nicola Marzari, Francesco Mauri, Riccardo Mazzarello, Stefano Paolini, Alfredo Pasquarello, Lorenzo Paulatto, Carlo Sbraccia, Sandro Scandolo, Gabriele Sclauzero, Ari P Seitsonen, Alexander Smogunov, Paolo Umari, and Renata M Wentzcovitch. QUANTUM ESPRESSO: a modular and open-source software project for quantum simulations of materials. *Journal of Physics: Condensed Matter*, 21(39):395502 (19pp), 2009.

[6] P Giannozzi, O Andreussi, T Brumme, O Bunau, M Buongiorno Nardelli, M Calandra, R Car, C Cavazzoni, D Ceresoli, M Cococcioni, N Colonna, I Carnimeo, A Dal Corso, S de Gironcoli, P Delugas, R A DiStasio Jr, A Ferretti, A Floris, G Fratesi, G Fugallo, R Gebauer, U Gerstmann, F Giustino, T Gorni, J Jia, M Kawamura, H-Y Ko, A Kokalj, E Küçükbenli, M Lazzeri, M Marsili, N Marzari, F Mauri, N L Nguyen, H-V Nguyen, A Otero de-la Roza, L Paulatto, S Poncé, D Rocca, R Sabatini, B Santra, M Schlipf, A P Seitsonen, A Smogunov, I Timrov, T Thonhauser, P Umari, N Vast, X Wu, and S Baroni. Advanced capabilities for materials modelling with QUANTUM ESPRESSO. *Journal of Physics: Condensed Matter*, 29(46):465901, 2017.

[7] Mark S. Hybertsen and Steven G. Louie. Electron correlation in semiconductors and insulators: Band gaps and quasiparticle energies. *Physical Review B*, 34(8):5390–5413, October 1986.

[8] Jack Deslippe, Georgy Samsonidze, David A. Strubbe, Manish Jain, Marvin L. Cohen, and Steven G. Louie. BerkeleyGW: A massively parallel computer package for the calculation of the quasiparticle and optical properties of materials and nanostructures. *Computer Physics Communications*, 183(6):1269–1289, June 2012.

[9] Arash A. Mostofi, Jonathan R. Yates, Giovanni Pizzi, Young-Su Lee, Ivo Souza, David Vanderbilt, and Nicola Marzari. An updated version of wannier90: A tool for obtaining

maximally-localised Wannier functions. *Computer Physics Communications*, 185(8):2309–2310, August 2014.

[10] Matthew Harvey. Imperial College Research Computing Service, 2017.

[11] Nicola Marzari, Arash A. Mostofi, Jonathan R. Yates, Ivo Souza, and David Vanderbilt. Maximally localized Wannier functions: Theory and applications. *Reviews of Modern Physics*, 84(4):1419–1475, October 2012.

[12] Ross Larsen and Benjamin Schwartz. Efficient real-space configuration-interaction method for the simulation of multielectron mixed quantum and classical nonadiabatic molecular dynamics in the condensed phase. *The Journal of Chemical Physics*, 119(15), 2003.

[13] Michael Rohlfing and Steven Louie. Optical excitations in conjugated polymers. *Phys. Rev. Lett.*, 82(9), 1999.

[14] Stoyan Karabunarliev and Eric R. Bittner. Polaron–excitons and electron–vibrational band shapes in conjugated polymers. *The Journal of Chemical Physics*, 118(9), 2003.

Chapter 6

Conformation dependent optical properties studied using W-CIS

6.1 Introduction

The goal of this thesis is to gain insight into the morphology dependence of the optical absorption properties of conjugated polymers. In chapter 4 I used time-dependent density functional theory (TDDFT) to calculate the optical properties of different conformers of oligothiophenes and the two non-fullerene acceptors (NFAs) IDTBR and IDFBR. The results showed that the oscillator strengths of oligothiophenes and the two NFAs are extremely sensitive to small changes in geometry, such as coplanarity and colinearity of neighbouring units. As a large variety of conformations may be present in a solid film resulting from the processing conditions or presence of other blend components and phases, it is important to perform excited state calculations on large numbers of macromolecules in different conformations in order to effectively study the relationship between the morphology and optical properties. This is also supported by the study of Jackson et al. [1] demonstrating that it is important to consider many conformational or structural isomers to capture significant deviations in the electronic and optical properties of conjugated polymers.

A common approach is to obtain optical spectra using conformational averaging by combining

classical molecular dynamics (MD) with quantum mechanical/molecular mechanics (QM/MM) calculations. This approach was used by Sjoqvist et al.[2][3][4] in the context of using luminescent conjugated oligothiophenes as optical probes for spectral assignment of particular protein deposits. As part of this work they also found a strong correlation between the transition energy of the first excited state and the oligomer's dihedral rotations, which was in agreement with associated experimental spectra. The link between torsional disorder and optoelectronic properties in conjugated polymers has been studied for several decades, where early work separated polymers into submolecules based on conjugation breaks defined by a critical dihedral angle[5][6]. Most later work incorporation torsional disorder into model Hamiltonians by varying electron transfer integrals[7][8] or exciton coupling term[9][10][11] as a function of the dihedral angle, or by treating the exciton coupling energy as a Gaussian variable[12][13]. These model Hamiltonians are discussed in detail in chapter 2, and the main difference between these studies and the W-CIS method presented in chapter 5 is that the latter obtains the parameters from *ab initio* calculations. Therefore, the main advantage of using the modelling framework presented in this thesis is that it can be combined with a classical MD study in such a way that the model Hamiltonian considers both the effect of varying chemical and conformational structure. This is particularly important if the material under consideration has a non-standard response to torsional twists, such as examples reported by Troisi and Shaw [14] which exhibited strong electronic coupling between monomers despite large dihedral angles.

As a first step towards this type of multi-scale study I will introduce periodic conformational distortions to two well studied π-conjugated polymers, polyacetylene and polythiophene, and study the effect of these conformational changes on the optical properties using the coarse-grained W-CIS method. I first study the optical properties of oligoacetylenes with varying bond length alternation (BLA), and then look at oligothiophenes with varying dihedral angles. BLA is defined as the difference between the double bond length d_{double} and single bond length d_{single} shown on the left of figure 6.1. BLA is a result of the Peierls distortion in polyacetylene where relaxation of the nuclei into 'dimers' in the ground state opens up a band gap between the HOMO and LUMO. Then I study the optical properties of oligothiophenes with varying dihedral angles. A dihedral angle is the angle between the planes of neighbouring aromatic

units, where the two planes are defined by two sets of three atoms labeled ABC and BCD, as shown on the right in figure 6.1.

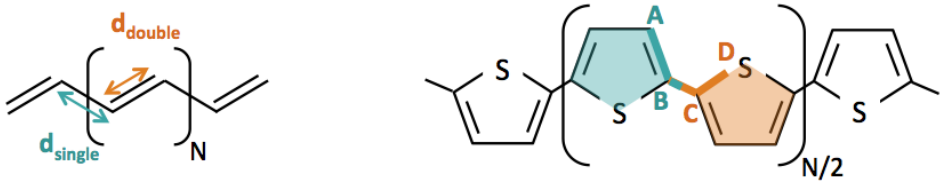

Figure 6.1: Repeat units of (left) polyacetylene showing the double bond length d_{double} and single bond length d_{single} used to calculate BLA and (right) polythiophene showing the two planes used to measure the dihedral angle.

BLA and dihedral angles were chosen, as they are changes in geometry that can be applied to most conjugated systems, and thus the results of these two studies are useful in building a better understanding of how a structure change in a conjugated material affects its optical properties. By studying the effect of systematic structural modifications like these I aim to gain insight into how the geometry of the molecular building blocks influence the parameters that determine the model Hamiltonian, such as the coupling between molecular orbitals or electron-hole interaction energies, and thus to shine a light on the origin of morphology dependent trends of optical properties of conjugated polymers.

6.2 Bond length alternation in oligoacetylenes

This section presents the trends in optical absorption properties of oligoacetylenes as a function of BLA calculated by solving the W-CIS Hamiltonian, and also investigates how the underlying parameters, such as the coupling between molecular orbitals or electron-hole interaction energies, vary with BLA and how these link to the observed optical absorption properties.

6.2.1 Parameterisation

The W-CIS parameters required to calculate the optical properties of oligoacetylenes are obtained from *ab initio* calculations of polyacetylene. In this approach an N-mer oligoacetylene is thus built up from N identical C_2H_2 acetylene units. Table 6.1 summarises the bond lengths and resulting BLA values for the four different polyacetylene structures used in this chapter. These were obtained by performing DFT geometry relaxation calculations with the Quantum Espresso code using a 10^{-6} Ha energy and 10^{-5} $a.u.$ force convergence threshold. The second structure in the table ($BLA = 0.04$Å) is the equilibrium structure obtained from a relaxation calculation without any constraints, and the other structures were obtained from geometry relaxation calculations where the value of d_{double} is constrained but allowing d_{single} and the bond angles to reach optimum values.

d_{double} (Å)	d_{single} (Å)	BLA (Å)
1.39	1.41	0.02
1.38	1.42	0.04
1.37	1.42	0.05
1.36	1.43	0.07

Table 6.1: Bond lengths (d_{single}, d_{double}) and bond length alternation (BLA) of the acetylene structures studied in this chapter.

A detailed description of the electronic structure calculations performed to obtain the maximally localised Wannier functions (WFs) used to describe the HOMO and LUMO of an acetylene unit can be found in section 5.2.2. Here I only present the results of these calculations.

Figure 6.2a plots the HF band structure of polyacetylene with a BLA of 0.02 Å. The WF describing the HOMO ($W_i^v(\boldsymbol{r})$) is obtained by wannierising the three highest valence bands, which are energetically separated from the other bands, and selecting the WF with the highest on-site energy. The WF describing the LUMO ($W_i^c(\boldsymbol{r})$) is obtained by wannierising the lowest conduction band specifying a frozen energy window between -1.2 eV and 1.2 eV in order to disentangle it from the other conduction bands. The figure also plots the wannierised WF bands, which are calculated using the on-site energies ϵ^v, ϵ^c and transfer integrals $t^v(s)$, $t^c(s)$ obtained from the wannierisation (see equation 5.6). Figure 6.2b shows $W_i^v(\boldsymbol{r})$ and $W_i^c(\boldsymbol{r})$

corresponding to the two wannierised bands.

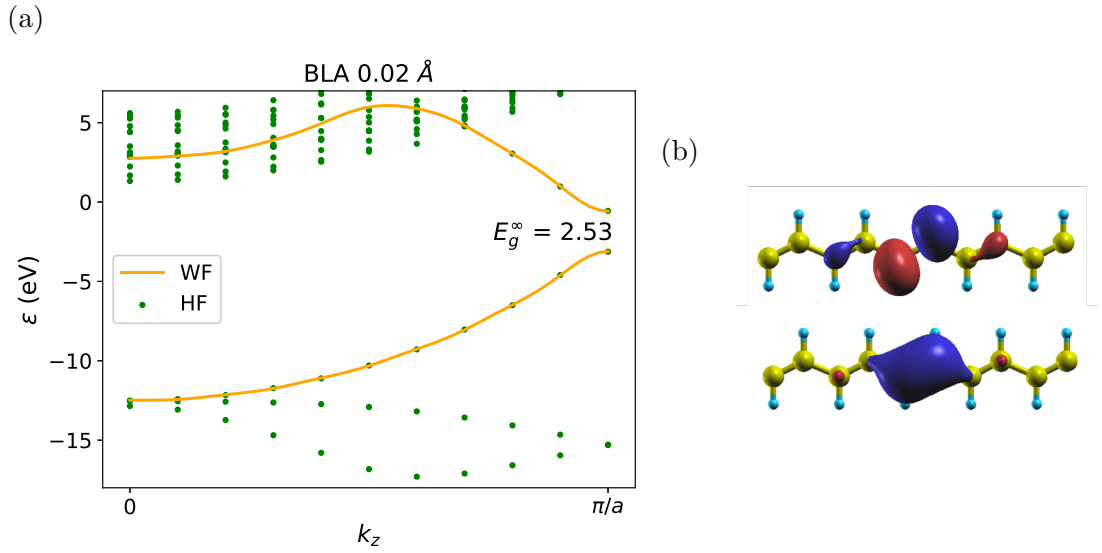

Figure 6.2: a) HF bandstructure (green) of polyacetylene with a BLA of 0.02 Å and the WF bands (orange) corresponding to $W_i^v(\boldsymbol{r})$ and $W_i^c(\boldsymbol{r})$, which are plotted in b).

The band structures of the four polyacetylenes with different BLA are qualitatively very similar, so only one of them is plotted in figure 6.2a. The key differences between them are the energies of the lowest conduction and highest valence bands at the band edge, which are shown in figure 6.3. The figure shows that the band gap is increasing by 1.49 eV when the BLA is increased from 0.02 Å to 0.07 Å, which is both due to a decrease in the valence band edge energy by 0.68 eV and an increase in the conduction band edge energy by 0.81 eV.

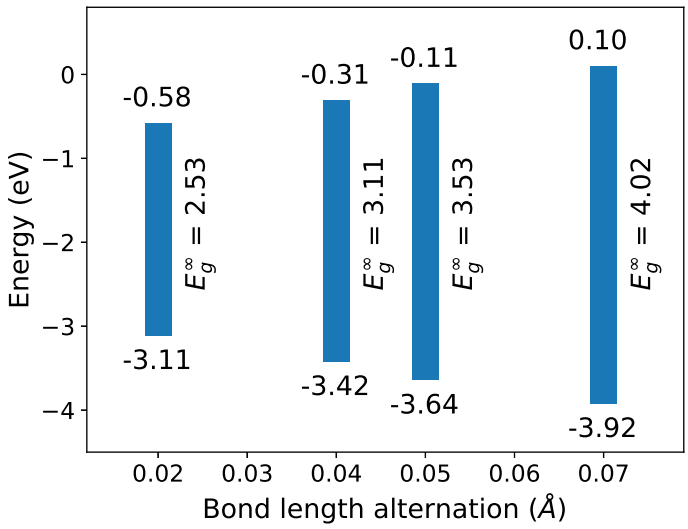

Figure 6.3: The energies of the valence and conduction band edges for polyacetylenes with different BLAs and associated polymer band gaps.

6.2.2 Oligomer optical spectra

The parameters obtained from the DFT calculations on polyacetylene are used to calculate the optical properties of finite oligomers by approximating every unit in the oligomer to be an identical C_2H_2 acetylene unit. Figure 6.4 shows the optical absorption spectra of 20-mer oligoacetylenes with different BLA obtained from solving the W-CIS Hamiltonian. The lowest energy peak of the oligomer spectrum has the highest oscillator strength, and as the BLA is increased from 0.02 Å to 0.07 Å it is blue-shifting and increasing in strength.

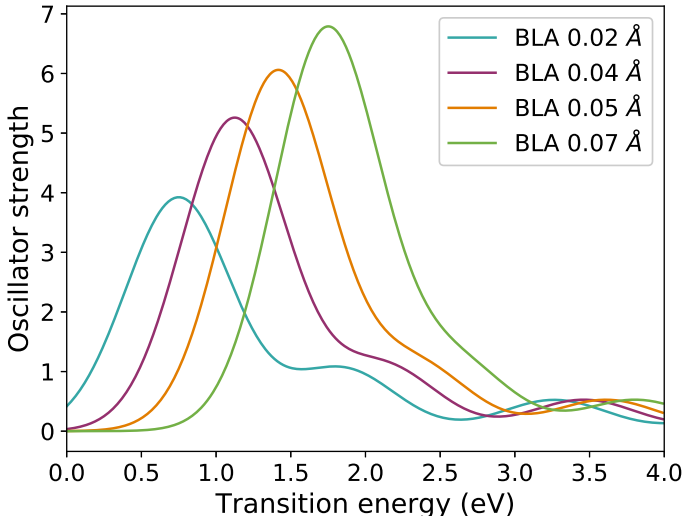

Figure 6.4: Optical absorption spectra showing the W-CIS calculated oscillator strengths broadened with a Gaussian function of width $\sigma = 0.25\ eV$ as a function of transition energy for 20-mer oligoacetylenes with different BLAs.

Figure 6.5 looks at the optical properties shown in the oligomer spectra in more detail. The blue shift is caused by the increase in the transition energy of the first excited state E_1 and the increase in peak height is caused by the increase in oscillator strength f_1 of the first excited state, as shown in figures 6.5a and 6.5c. In order to understand what drives the increase in oscillator strength we need to also look at the transition dipole moment (plotted in figure 6.5b), as the oscillator strength is proportional to the product of the transition energy and the transition dipole strength $|\boldsymbol{\mu}_1|^2$, in atomic units this relation is given as

$$f_1 = \frac{2}{3} E_1 |\boldsymbol{\mu}_1|^2. \tag{6.1}$$

The transition dipole strength is decreasing from 189 $(ea_0)^2$ to 140 $(ea_0)^2$, which corresponds to a 26 % decrease and is much lower than the 132 % increase in transition energy, therefore the oscillator strength shows an increasing trend with BLA despite the decrease in $|\boldsymbol{\mu}|^2$. Thus, both the blue-shift and increase in peak height in the oligomer spectra in figure 6.4 are mainly caused by the increase in E_1, but the quantitative trend of the oscillator strength is also affected by the decrease in $|\boldsymbol{\mu}_1|^2$.

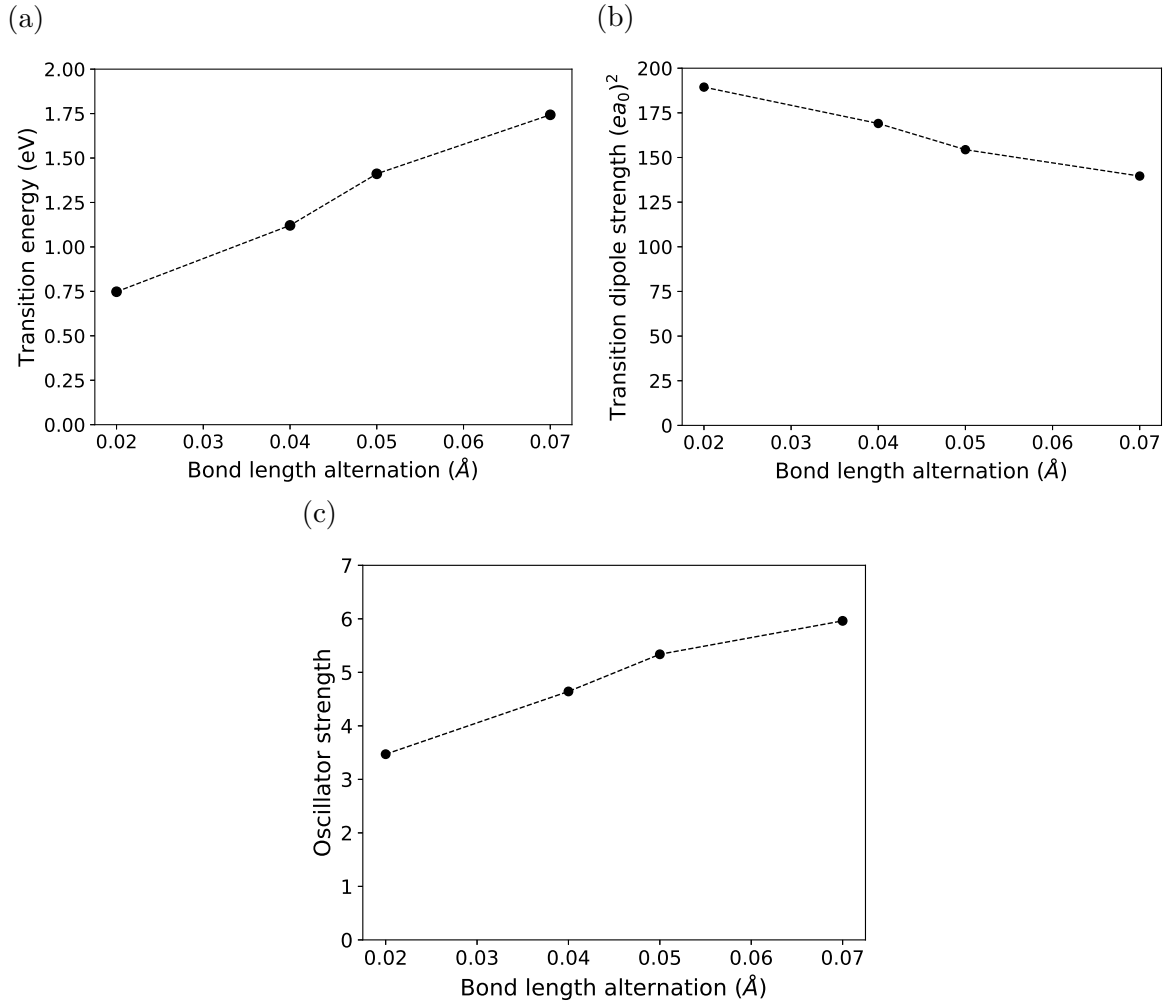

Figure 6.5: (a) Transition energy E_1, (b) transition dipole strength $|\boldsymbol{\mu}_1|$ and (c) oscillator strength f_1 of the first excited state of a 20-mer oligoacetylene as a function of BLA calculated using the W-CIS method.

As shown in figure 6.6 the same trend of increasing transition energy, decreasing transition dipole strength and increasing oscillator strength with increasing BLA is observed for all lengths of oligoacetylenes (except for the specific oscillator strength f_1/N for short oligomers with $N < 5$), but the effect is more pronounced the longer the oligomer.

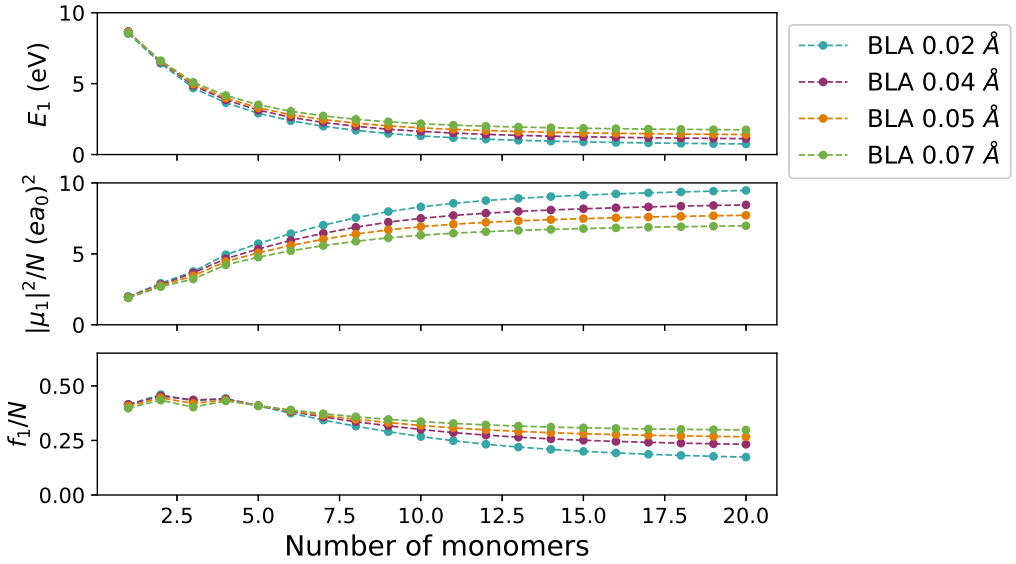

Figure 6.6: Transition energy (E_1), specific transition dipole strength ($|\boldsymbol{\mu}_1|^2/N$) and specific oscillator strength (f_1/N) of the first transition of an oligoacetylene as a function of number of monomers.

6.2.3 Transition energies

In order to further understand the origin of the structure dependent trends in optical properties presented above, I will analyse the W-CIS parameters and other relevant quantities that determine the values of the transition energies.

The transition energy of the first excited state E_1 can be split into a contribution from the band gap E_g and the exciton binding energy E_b. The band gap is the difference between the oligomer HOMO and LUMO energy levels, which can be calculated using a linear combination of molecular orbitals approach, namely by solving the eigenvalue problem

$$\sum_{ii'}^{N} H_{ii'}^{v(c)} A_{i'}^{n} = E_n^{v(c)} A_i^n, \tag{6.2}$$

where $E_n^{v(c)}$ is the energy of the n-th valence (conduction) state and the Hamiltonian consists of the W^v (W^c) on-site energies and transfer integrals:

$$H_{ii'}^{v(c)} = \epsilon^{v(c)} \delta_{ii'} + t^{v(c)}(s). \tag{6.3}$$

The highest E_n^v energy then gives the HOMO energy, and the lowest E_n^c energy gives the LUMO energy. Figure 6.7a plots the calculated oligomer energy levels and corresponding band gaps as a function of BLA. Finally, E_b is simply calculated as the difference between E_g and E_1, where E_1 is obtained by solving the W-CIS Hamiltonian. Figure 6.7b plots the band gaps and exciton binding energies side by side.

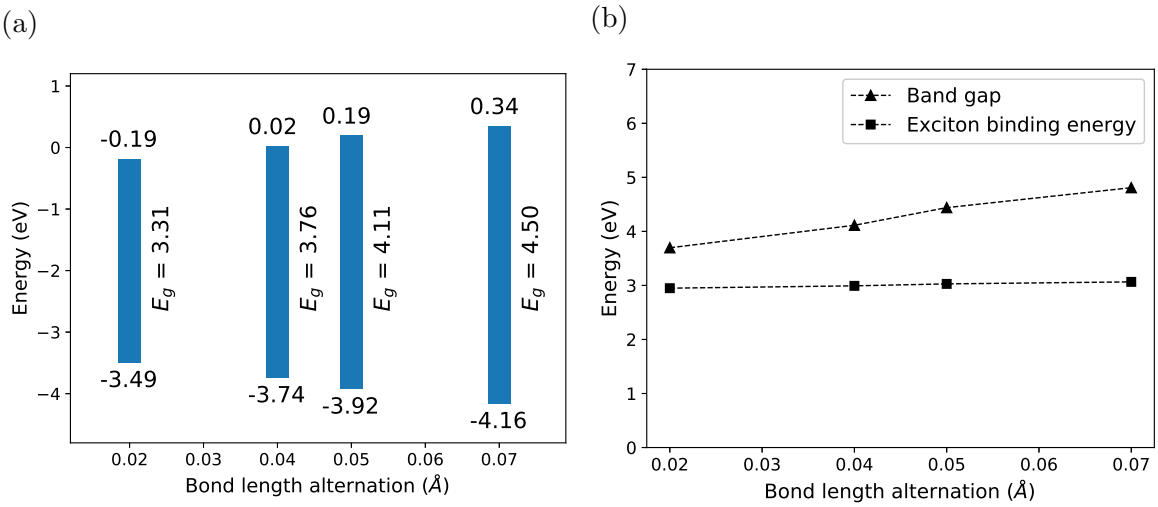

Figure 6.7: (a) HOMO and LUMO energies of 20-mer oligoacetylenes with different BLAs and their associated oligomer band gaps E_g and (b) the same band gaps plotted alongside the exciton binding energy of the oligomers.

The band gap is increasing with increasing bond length alternation, whereas the exciton binding energy is hardly affected. Thus, we can conclude that the increase in transition energy with increasing BLA is driven by the increase in the oligomer's band gap, which in turn determined by the values of the on-site energies and transfer integrals of $W^v(\boldsymbol{r})$ and $W^c(\boldsymbol{r})$.

The on-site energies and transfer integrals for the W-CIS Hamiltonian are obtained by wannierising the highest valence band and lowest conduction band of the polyacetylene structures, as was described in section 6.2.1. The obtained parameters are shown in figure 6.8.

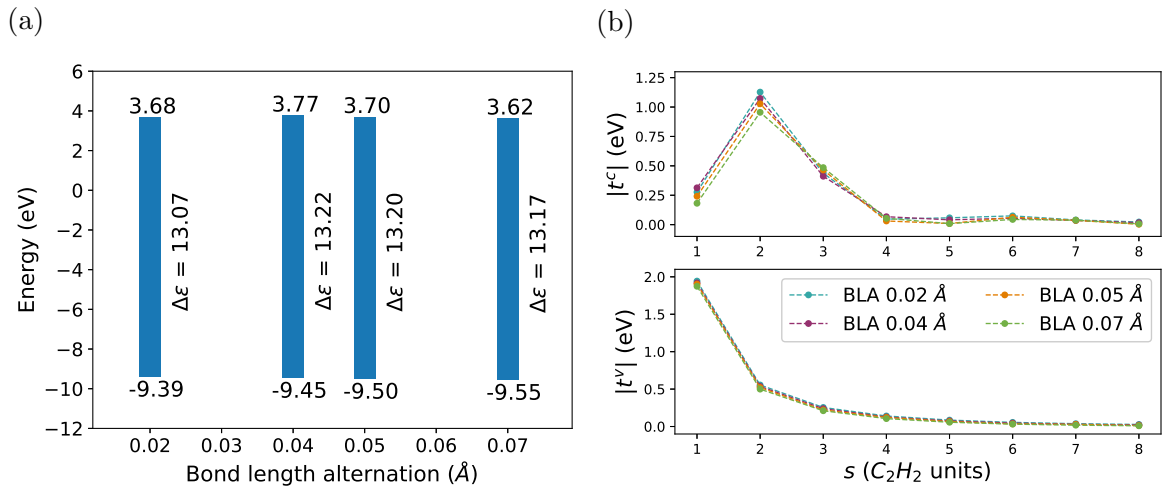

Figure 6.8: (a) On-site energies ϵ^v, ϵ^c of the WFs W^v, W^c representing the HOMO and LUMO of an acetylene unit and their difference $\Delta\epsilon$ and (b) the transfer integrals t^v, t^c of W^v and W^c as a function of particle separation.

Figure 6.8a shows the on-site energies for the HOMO (ϵ^v) and LUMO (ϵ^c) together with their difference ($\Delta\epsilon = \epsilon^c - \epsilon^v$), which corresponds to the band gap of a monomer according to the W-CIS method. The on-site energies do not change much when the BLA is increased - $\Delta\epsilon$ varies within a range of 0.15 eV. Thus the change in on-site energies cannot explain the trend in oligomer HOMO and LUMO energies plotted in figure 6.7a. Figure 6.8b plots the absolute values of the transfer integrals for the HOMO (t^v) and LUMO (t^c) as a function of particle separation s. As the BLA is increased the transfer integral values are decreasing (with the exception of the $t^c(s)$ values at $s = 3, 5$). In other words, the larger the bond length alternation, the less coupled the HOMO and LUMO WFs of neighbouring monomer units are, which in turn is causing the increase in the LUMO level, decrease in the HOMO level and thus the widening of the oligomer band gap shown in figure 6.7.

The exciton binding energy is determined by the electron-hole Coulomb interactions. Figure 6.9a plots the $U^d(s)$ and $U^x(s)$ values and figure 6.9b plots the value of the Coulomb term found on the diagonal of the W-CIS Hamiltonian ($2U^x - U^d$). The Coulomb interaction stays nearly constant with a change in BLA, which is in agreement with the exciton binding energies being nearly constant as was shown in figure 6.7b.

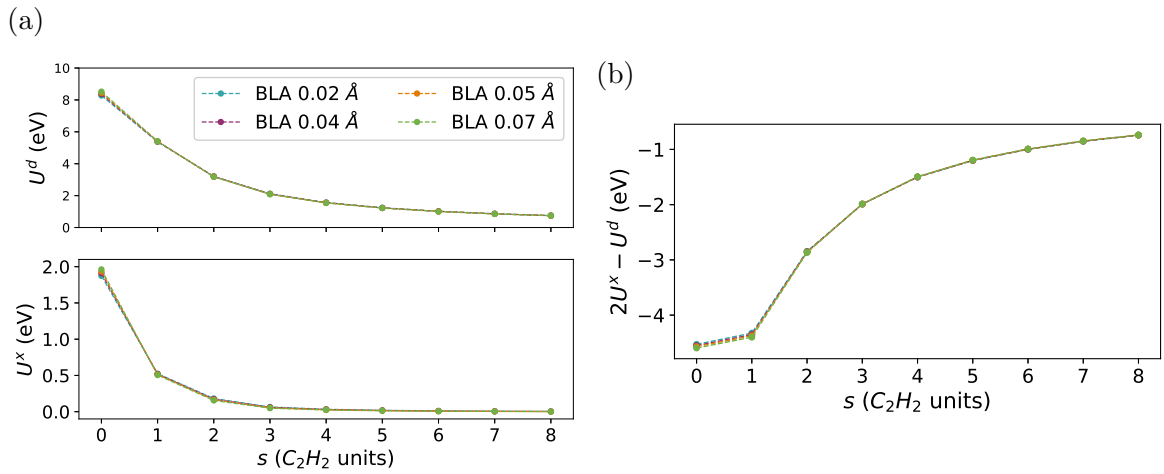

Figure 6.9: a) Direct and exchange Coulomb integral terms $U^d(s)$, $U^x(s)$ for polyacetylene with different BLAs as a function of electron-hole separation s and b) the value of the diagonal Coulomb term of the W-CIS Hamiltonian $2U^x(s) - U^d(s)$.

In conclusion, increasing the BLA is lowering the coupling between HOMOs and LUMOs of neighbouring acetylene units, which results in the widening of the band gap and thus also an increase in the transition energy of the first excited state of the oligomers.

6.2.4 Transition dipole strengths

Even though the increase in transition energy described above is the underlying effect that determines the qualitative trend of the oscillator strength with varying BLA, the oscillator strength quantitatively also depends on the transition dipole strength plotted in figure 6.5b, so it is worth looking into the underlying W-CIS parameters that determine the trend in transition dipole strength for oligoacetylenes with varying BLA.

The transition dipole moment of an oligomer for the n-th excited state is calculated according to this formula

$$\boldsymbol{\mu}_n = \sum_{ij} A^n_{ij} \boldsymbol{\mu}(s), \tag{6.4}$$

where A^n_{ij} are the eigenvector coefficients obtained from diagonalising the W-CIS Hamiltonian, i and j are the electron and hole site indices, and $\boldsymbol{\mu}(s)$ is the intermonomer transition dipole moment as a function of electron-hole separation $s = |i - j|$.

Figure 6.10 plots the intermonomer transition dipole moments as a function of electron-hole separation. As the BLA is increased, the $\boldsymbol{\mu}(s)$ values are decaying faster. In other words, the larger the BLA, the smaller the transition dipole moment between HOMO and LUMO WFs at all separations. This aligns with the decreasing trend in transition dipole strengths of the oligomers plotted in figure 6.5b.

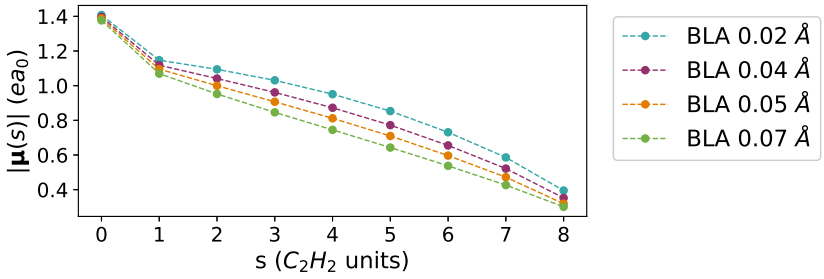

Figure 6.10: Intermonomer transition dipole moment magnitudes $|\boldsymbol{\mu}(s)|$ as a function of electron-hole separation s for polyacetylenes with different BLAs.

The other contributing factor to the oligomer transition dipole moments are the eigenvector coefficients of the first excited state A^1_{ij}. Figure 6.11a plots the fraction of how much different exciton basis states contribute to the first excited state. This is calculated as the sum of the squares of the relevant eigenvector elements $\sum_i |A^1_{i,i+s}|^2$ for each electron-hole separation s. The basis state contributions do not vary much with BLA except for a slight increase in the $s = 0$ and $s = 1$ basis state contributions (blue and orange) and a slight decrease in the $s = 3$ and $s = 4$ basis state contributions (red and purple). A convenient way of quantifying this change in exciton basis state contributions is to calculate the corresponding exciton radii using this formula

$$r_{exciton} = \sum_{i,s} s \cdot |A_{i,i+s}|^2. \tag{6.5}$$

The calculated values are plotted in figure 6.11b showing a mild 8% decrease with increasing BLA, which is consistent with a slight increase in contributions from the lower s basis states and decrease in contributions from the higher s basis states.

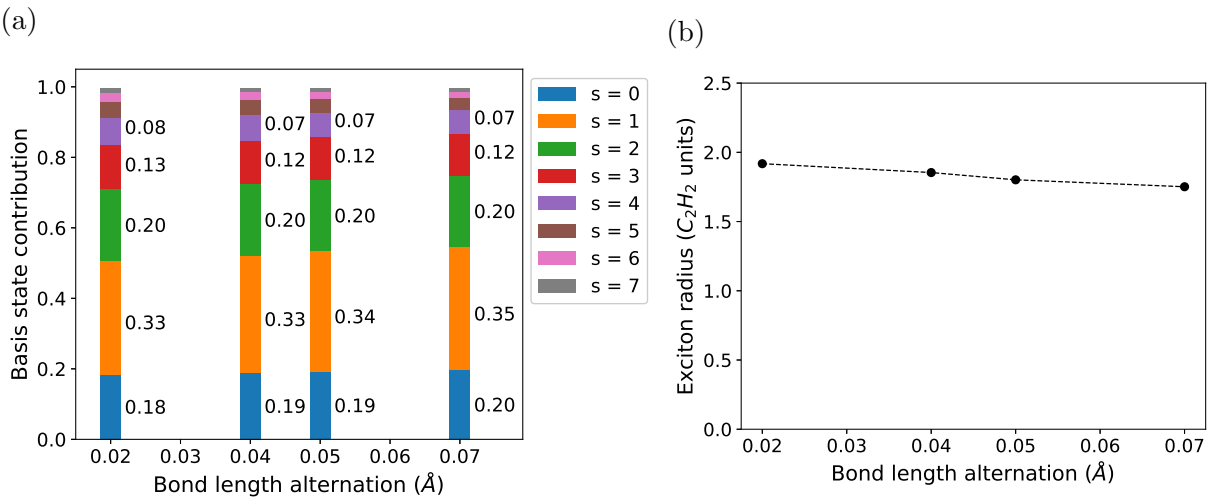

Figure 6.11: a) Contributions of exciton basis states with different electron-hole separations (s) to the first excited state of 20-mer oligoacetylenes with different BLAs and b) exciton radius as a function of BLA.

In the limit that the $\boldsymbol{\mu}(s)$ values were constant, a decrease in exciton radius would result in an increase in oligomer transition dipole moments, as the lower s basis states have higher $\boldsymbol{\mu}(s)$ values. However, the opposite trend is observed, so it can be concluded that the decreasing trend in transition dipole strengths is solely due to the $\boldsymbol{\mu}(s)$ values decreasing with increasing BLA and are not affected by the exciton radius plotted in figure 6.11.

6.3 Dihedral angles in oligothiophenes

Polythiophene is a widely studied and important material in the field of organic semiconductors, even though a lot of new polymers have been designed that display higher efficiencies in devices. It is still used in a lot of studies, for example when designing and evaluating new acceptor materials, because the properties of polythiophene are well studied and can thus be used as a reference material. Additionally, it is cheap and easy to synthesise and process so is most appropriate for commercial applications - and with the combination of new non-fullerene acceptors the device efficiencies are reaching viable levels to use it in devices (section 4.3). Thus, it is worth investigating its optical absorption properties in more detail.

6.3.1 Parameterisation

The W-CIS parameters required to calculate the optical properties of oligothiophenes are obtained from *ab initio* calculations of polythiophene. In this approach an N-mer oligothiophene is thus built up from N identical C_4H_2S thiophene units. The three different polythiophene structures studied in this chapter were obtained by performing DFT geometry relaxation calculations with the Quantum Espresso code using a 10^{-6} Ha energy and 10^{-5} $a.u.$ force convergence threshold. The equilibrium structure obtained from a relaxation calculation without any constraints has a dihedral angle of 0°, and the other structures were obtained by constraining the dihedral angle to 20°, 30° and 45°.

Figure 6.12a plots the DFT band structure of polythiophene with a dihedral angle of 0°, and figure 6.12b plots the HF band structure of the same polymer. The WFs describing the HOMO ($W_i^v(\boldsymbol{r})$) are obtained by wannierising the four highest HF valence bands, which are energetically separated from the other bands, and selecting the two WFs with the highest on-site energies. As the HF conduction bands are entangled such that it is not possible to specify a frozen window to disentangle the bands corresponding to the LUMO, therefore the DFT bands are wannierised instead (see figure 6.12a). The WFs describing the LUMO ($W_i^c(\boldsymbol{r})$) are obtained by wannierising the two lowest DFT conduction bands and specifying a frozen energy window between -0.5 eV and 0.5 eV in order to disentangle it from the other conduction bands. Figure 6.12b also plots the wannierised WF bands, which are calculated using the on-site energies ϵ^v, ϵ^c and transfer integrals $t^v(s)$, $t^c(s)$ obtained from the wannierisation (see equation 5.6). Figure 6.12c shows $W_i^v(\boldsymbol{r})$ and $W_i^c(\boldsymbol{r})$ corresponding to the wannierised bands.

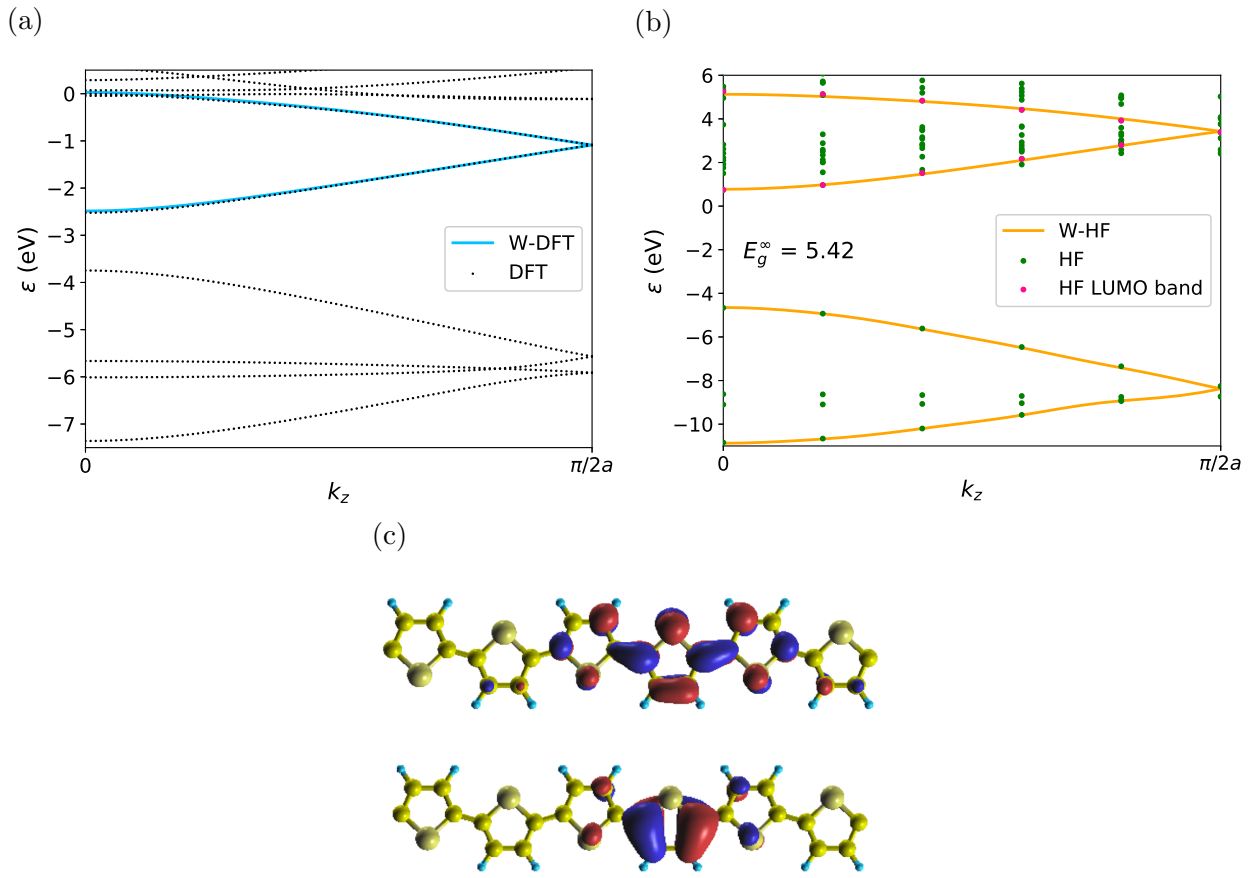

Figure 6.12: a) DFT band structure (black) and conduction WF band (blue) of polythiophene with a 0° dihedral angle, b) the same polymer's HF band structure (green) with highlighted LUMO bands (pink) and valence and conduction WF bands (orange) and the polymer band gap E_g^∞ and c) the HOMO (bottom) and LUMO (top) WFs associated with the wannierised bands.

The band structures of the four polythiophenes with different dihedral angles are qualitatively very similar, so only one of them is plotted in figure 6.12. The key differences between them are the energies of the lowest conduction and highest valence bands at the band edge, which are shown in figure 6.13. The figure shows that the band gap is increasing by 1.5 eV when the dihedral angle is increased from 0° to 45°, which is both due to a decrease in the valence band edge energy by 0.8 eV and an increase in the conduction band edge energy by 0.7 eV.

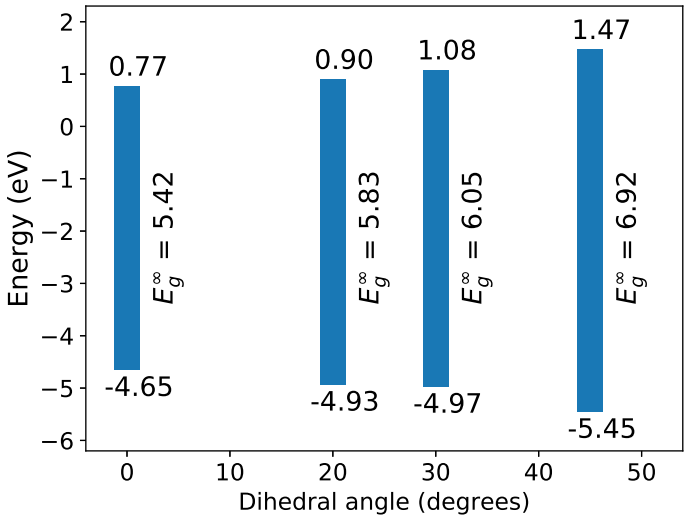

Figure 6.13: The energies of the valence and conduction band edges for polythiophenes with different dihedral angles and associated polymer band gaps.

6.3.2 Oligomer optical spectra

The parameters obtained from DFT calculations on polythiophenes are used to calculate the optical properties of finite oligomers by approximating every unit in the oligomer to be an identical C_4H_2S thiophene unit. Figure 6.14 shows the optical absorption spectra of 20-mer oligothiophenes with different dihedral angles obtained from solving the W-CIS Hamiltonian. The lowest energy peak of the oligomer spectrum has the highest oscillator strength and dominates the spectrum. As the dihedral angle is increased from 0° to 45 ° this lowest peak is blue-shifting. The height of the absorption peak is near constant between 0° and 30° and then drops significantly at 45°.

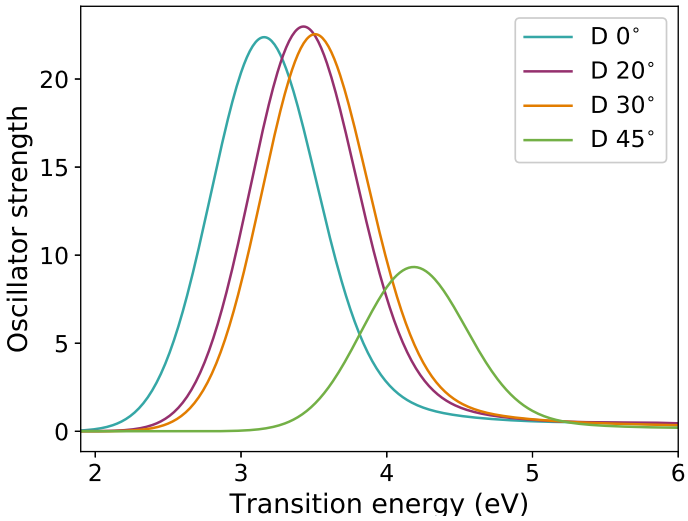

Figure 6.14: Optical absorption spectra showing the W-CIS calculated oscillator strength as a function of transition energy for oligothiophenes with different dihedral angles.

Figure 6.15 looks at the optical properties shown in the oligomer spectra in more detail. The blue shift is caused by the increase in the transition energy of the first excited state E_1 and the trend in peak height follows the trend in oscillator strength f_1 of the first excited state, as shown in figures 6.15a and 6.15c. As stated earlier, the oscillator strength is proportional to the product of the transition energy and the transition dipole strength $|\boldsymbol{\mu}_1|^2$, so in order to understand what drives the increase in oscillator strength we need to also look at the transition dipole moment plotted in figure 6.15b. The transition dipole strength is decreasing from 229 $(ea_0)^2$ to 207 $(ea_0)^2$ as the dihedral angle is increased from 0° to 30° and then drops to 71 $(ea_0)^2$ at 45°. The increase in E_1 and decrease in $|\boldsymbol{\mu}_1|^2$ is comparable between 0° to 30°, so f_1 hardly changes between these dihedral angle values. However, the drop in $|\boldsymbol{\mu}_1|^2$ from 30° to 45° is much larger than the increase in E_1, so the f_1 also shows a dramatic drop.

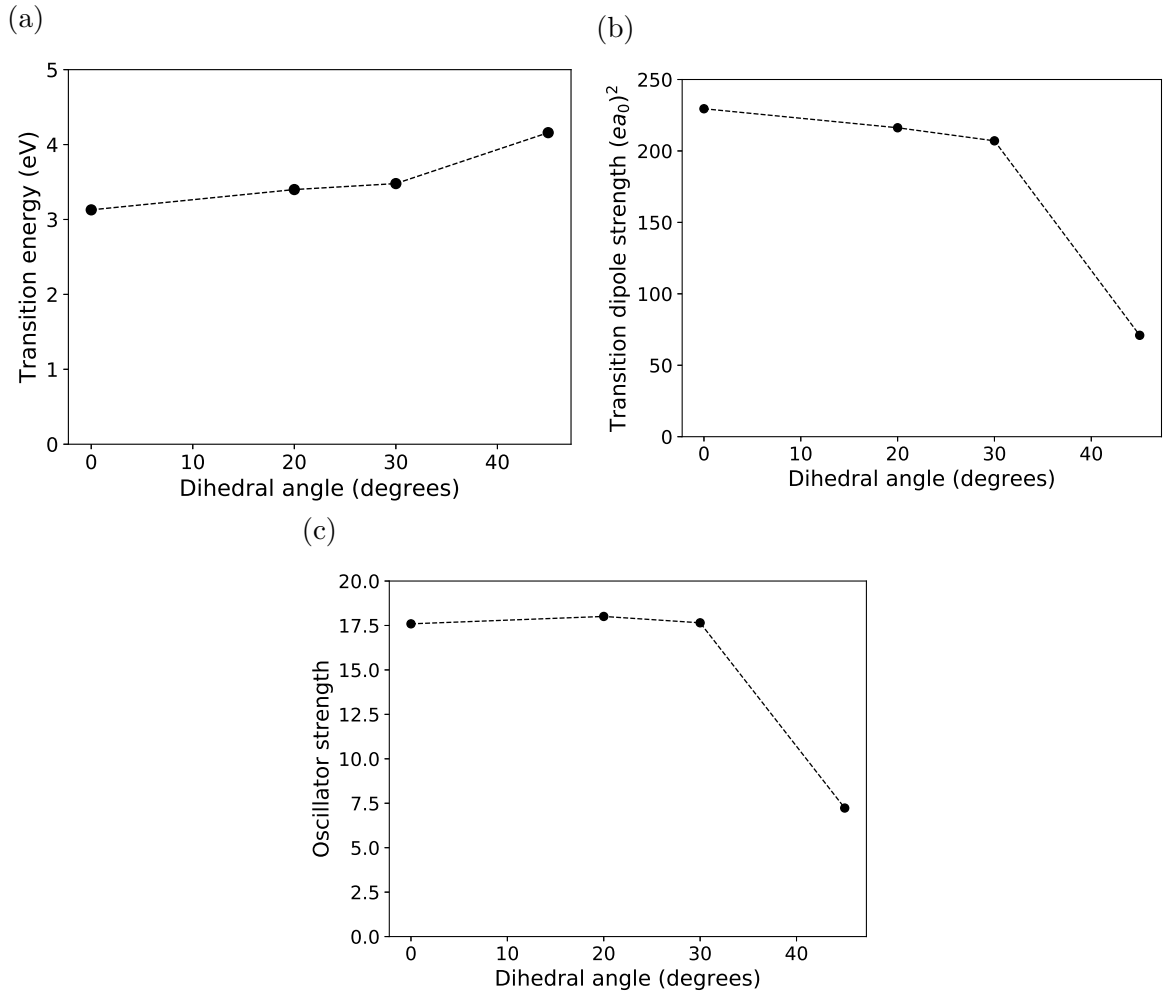

Figure 6.15: (a) Transition energy, (b) transition dipole strength and (c) oscillator strength of the first excited state of a 10-mer oligothiophene as a function of dihedral angle.

As shown in figure 6.16 the same trend in transition energy, transition dipole strength and oscillator strength with increasing dihedral angle is observed for all lengths of oligothiophenes, except for very short oligomers with $N < 3$.

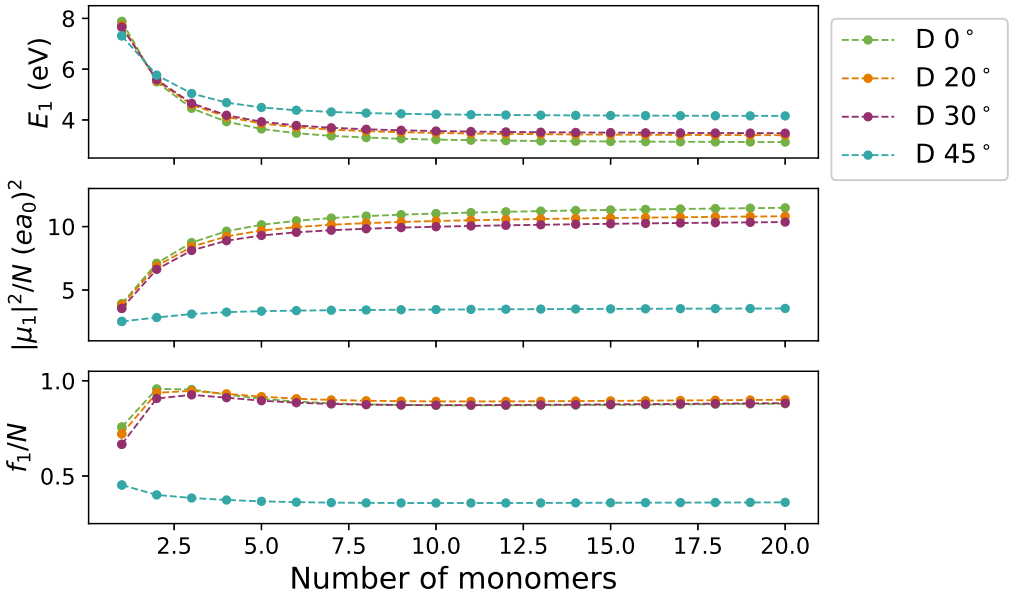

Figure 6.16: Transition energy (E_1), specific transition dipole strength ($|\boldsymbol{\mu}_1|^2/N$) and specific oscillator strength (f_1/N) of the first transition of an oligothiophenes as a function of number of monomers.

The blue-shift in the oligomer spectra with increasing dihedral angle in figures 6.14 and 6.16 is caused by the increase in E_1, whereas the trend in peak height is mainly caused by the decrease in $|\boldsymbol{\mu}_1|^2$. In order to further understand the origin of these structure dependent trends in optical properties, I will analyse the W-CIS parameters and other relevant quantities that determine the values of E_1 and $|\boldsymbol{\mu}_1|^2$.

6.3.3 Transition energies

In order to further understand the origin of the structure dependent trends in optical properties presented above, I will analyse the W-CIS parameters and other relevant quantities that determine the values of the transition energies.

The transition energy of the first excited state E_1 can be split into a contribution from the band gap E_g and the exciton binding energy E_b. Figure 6.17a plots the oligomer HOMO and LUMO energy levels and corresponding band gaps as a function of dihedral angle, and figure 6.17b plots the band gaps and exciton binding energies side by side.

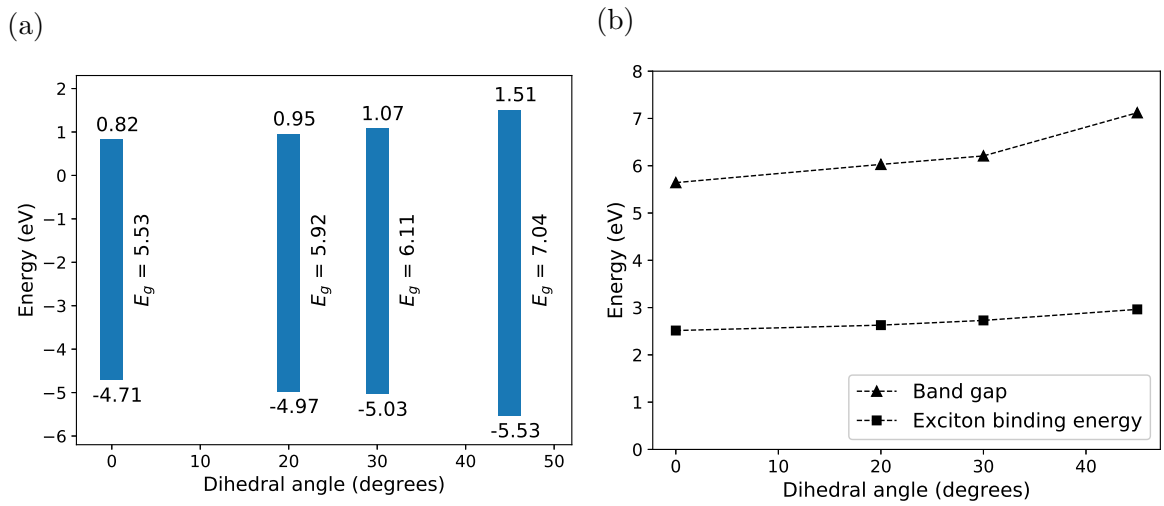

Figure 6.17: (a) HOMO and LUMO energies of 20-mer oligothiophenes with different dihedral angles and their associated oligomer band gaps E_g and (b) the same band gaps plotted alongside the exciton binding energy of the oligomers.

Both the band gap and binding energy are increasing with increasing dihedral angle, but the transition energy exhibits a stronger increase, especially from 30° to 45°. Thus, we can conclude that the increase in transition energy with increasing dihedral angle is mainly driven by the increase in the oligomer's band gap, which in turn determined by the values of the on-site energies and transfer integrals of $W^v(\boldsymbol{r})$ and $W^c(\boldsymbol{r})$.

Figure 6.18a shows the on-site energies ϵ^v and ϵ^c together with their difference $\Delta\epsilon$, which corresponds to the band gap of a monomer according to the W-CIS method. The on-site energies do not change much when the dihedral angle is increased - $\Delta\epsilon$ varies within a range of 0.12 eV. Figure 6.18b plots the absolute values of the transfer integrals t^v and t^c as a function of particle separation s. As the dihedral angle is increased the transfer integral values are decreasing (with the exception of the values at $s = 2$). In other words, the stronger the polymer chain torsion, the less coupled the HOMO and LUMO WFs of neighbouring monomer units are.

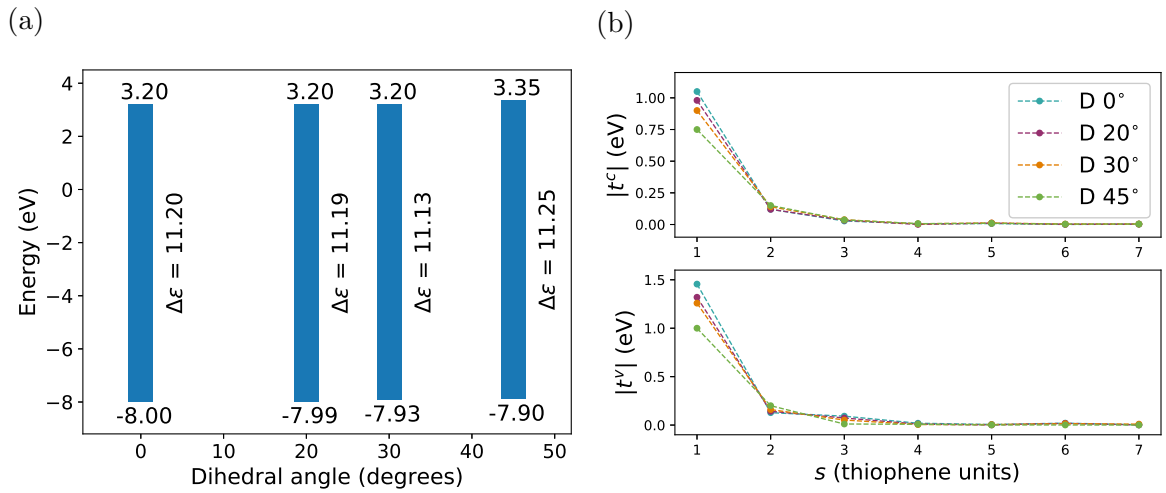

Figure 6.18: (a) On-site energies of the WFs representing the HOMO (W^v) and LUMO (W^c) of thiophene and their difference $\Delta\epsilon$ and (b) the transfer integrals of W^v and W^c as a function of particle separation.

Even though the increase in band gap with increasing torsion is the key driver causing an increase in the first transition energy of the oligomers, figure 6.17b also showed an increase in exciton binding energy with increased torsion. The exciton binding energy is determined by the electron-hole Coulomb interactions, which are plotted in figure 6.19. Figure 6.19b plots the value of the Coulomb term found on the diagonal of the W-CIS Hamiltonian ($2U^x - U^d$). At short electron-hole separations ($s = 0, 1$) the Coulomb term gets more negative with increasing torsion. In other words, the more twisted the oligomer, the stronger the electron-hole Coulomb interaction, which is in agreement with the exciton binding energy increasing with dihedral angle show in figure 6.17b.

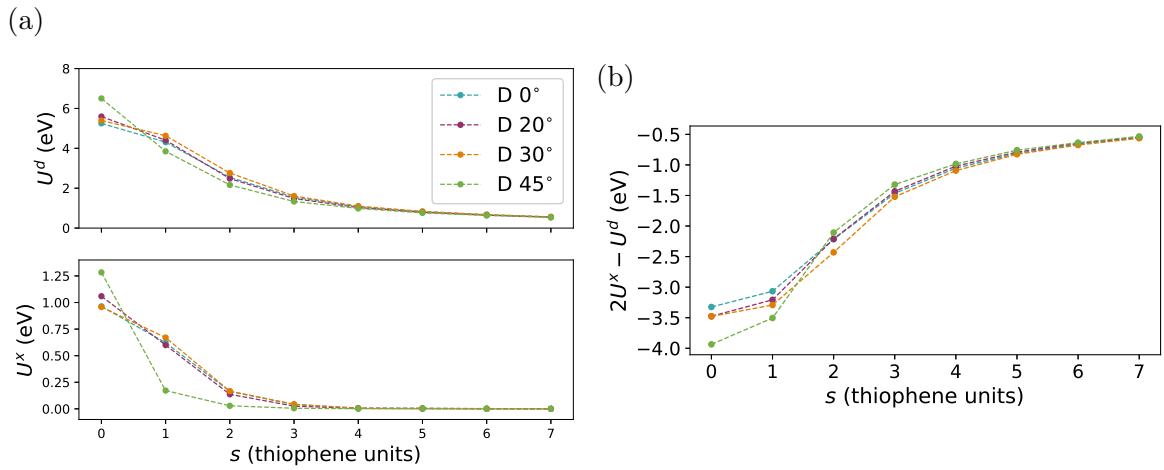

Figure 6.19: a) Direct and exchange Coulomb integral terms $U^d(s)$, $U^x(s)$ for polythiophene with different dihedral angles as a function of electron-hole separation s and b) the value of the diagonal Coulomb term of the W-CIS Hamiltonian $2U^x(s) - U^d(s)$.

In conclusion, increasing the dihedral angle is lowering the coupling between HOMOs and LUMOs of neighbouring thiophene units, which results in the widening of the band gap and thus also an increase in the transition energy of the first excited state of the oligomers. Additionally, the increase of the dihedral angle is also causing a slight increase in the electron-hole Coulomb interaction resulting in an increase in the exciton binding energy, which also contributes to the increase in transition energy of the first excited state.

6.3.4 Transition dipole moments

In order to further understand the origin of the decreasing oscillator strength with increasing dihedral angle torsion described in section 6.3.2, this section analyses the underlying W-CIS parameters and other relevant quantities.

The transition dipole moment is determined by the eigenvector coefficients A_{ij}^n obtained from diagonalising the W-CIS Hamiltonian, as well as the intermonomer transition dipole moments $\boldsymbol{\mu}(s)$ (see equation 6.4).

Figure 6.20 plots the intermonomer transition dipole moments as a function of electron-hole separation. As the dihedral angle is increased, the $\boldsymbol{\mu}(s)$ values are decaying faster, and there is a significantly larger drop in $\boldsymbol{\mu}(s)$ values when going from 30° to 45°. In other words, the

larger the polymer chain torsion, the smaller the transition dipole moment between HOMO and LUMO WFs at all separations. This aligns with the decreasing trend in transition dipole strengths of the oligomers plotted in figure 6.15b.

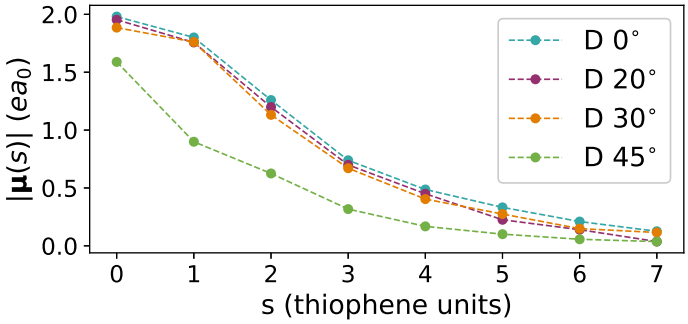

Figure 6.20: Intermonomer transition dipole moment magnitudes as a function of electron-hole separation s for thiophenes with different dihedral angles.

The other contributing factor to the oligomer transition dipole moments are the eigenvector coefficients of the first excited state A^1_{ij}. Figure 6.21a plots the fraction of how much different exciton basis states contribute to the first excited state. The basis state contributions do not vary much with dihedral angle except for an increase in the $s = 0$ and $s = 1$ basis state contributions (blue and orange) and a decrease in the $s = 2$ basis state contributions (green). A convenient way of quantifying this change in exciton basis state contributions is to calculate the corresponding exciton radii, the calculated values are plotted in figure 6.21b showing a decrease with increasing dihedral angle, which is consistent with a slight increase in contributions from the lower s basis states and decrease in contributions from the lower s basis states.

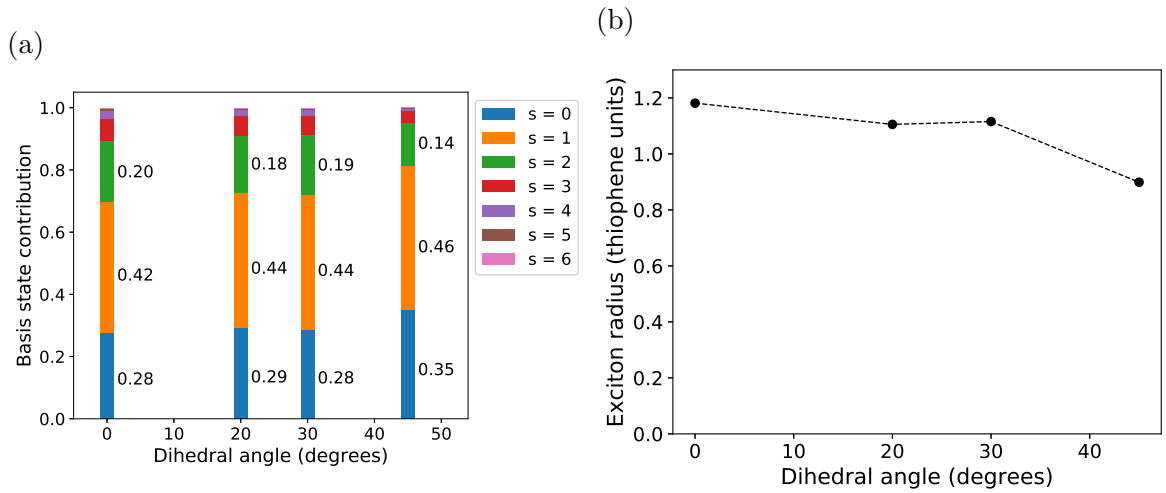

Figure 6.21: a) Contributions of exciton basis states with different electron-hole separations (s) to the first excited state of 20-mer oligothiophenes with different dihedral angles and b) exciton radius as a function of dihedral angle.

In the limit that the $\boldsymbol{\mu}(s)$ values were constant, a decrease in exciton radius would result in an increase in oligomer transition dipole moments, as the lower s basis states have higher $\boldsymbol{\mu}(s)$ values. However, the opposite trend is observed, so it can be concluded that the decreasing trend in transition dipole strengths is solely due to the $\boldsymbol{\mu}(s)$ values decreasing with increasing dihedral angle and are not affected by the exciton radius plotted in figure 6.21.

6.4 Discussion and conclusions

I calculated the optical properties of oligoacetylenes with varying BLA using the W-CIS method. The optical absorption spectra presented in section 6.2.2 show that increasing the BLA results in the lowest energy peak blue shifting and increasing in height, which was shown to be due to a significant increase in the transition energy of the first excited state. A further analysis of the W-CIS parameters showed that this trend is cause by an increase in the band gap, which can be attributed to a decrease in coupling between the WFs representing the HOMO and LUMO of the oligomers.

I also calculated the optical properties of oligothiophenes with varying dihedral angles using the W-CIS method. The optical absorption spectra presented in section 6.3.2 show that increasing the dihedral angle results in the lowest energy peak blue shifting and staying near constant in

height when twisting the chain up to 30° and dramatically dropping in height at 45°. These changes in spectra were shown to be due to an increase in the transition energy and a decrease in the transition dipole strength of the first excited state. A further analysis of the W-CIS parameters in section 6.3.2 showed that the trend in transition energy is mainly caused by an increase in the band gap, but an increase in the exciton binding energy is also contributing. The increase in band gap can be directly attributed to a decrease in coupling between the WFs representing the HOMO and LUMO of the oligomers, and the increase in binding energy can be attributed to a strengthening of the electron-hole Coulomb interaction. Furthermore, the analysis of the W-CIS parameters showed that the decreasing trend in transition dipole strength is caused by a decrease in the intermonomer transition dipole moments.

Varying the bond length alternation or dihedral angle are relatively simple geometry changes that can be applied to most conjugated systems, therefore, the results of this chapter can be used as a first approximation when predicting the effect of these conformational changes in other materials. As outlined in this chapter's introduction, the link between torsional disorder and optoelectronic properties in conjugated polymers has been studied for several decades, where early work separated polymers into submolecules based on conjugation breaks defined by a critical dihedral angle[5][6]. Most later work incorporation torsional disorder into model Hamiltonians by varying electron transfer integrals [7][8] or exciton coupling term[9][10][11] as a function of the dihedral angle, or by treating the exciton coupling energy as a Gaussian variable[12][13]. The main advantage of the W-CIS approach presented in this thesis is that I obtain the model Hamiltonian matrix elements from *ab initio* calculations, meaning that the model is capable of incorporating changes in geometry, as well as changes in the intramolecular interactions that results from specific chemical structure.

Additionally, this study can be treated as the first step towards a multiscale study performing excited state calculations on large numbers of macromolecules in different conformations in order to further study the relationship between the morphology and optical properties of conjugated polymers. In a more extended application of this approach, the dependence of model Hamiltonian parameters on particular degrees of freedom of the inter-monomer geometry could be obtained using series of explicit calculations like these, and the dependence fitted to some

functional form which could then be used to approximate the Hamiltonian elements for more general arrangements of chemical building blocks.

Bibliography

[1] Nicholas E. Jackson, Brett M. Savoie, Kevin L. Kohlstedt, Tobin J. Marks, Lin X. Chen, and Mark A. Ratner. Structural and conformational dispersion in the rational design of conjugated polymers. *Macromolecules*, 47(3):987–992, January 2014.

[2] J. Sjoqvist, M. Linares, M. Lindgren, and P. Norman. Molecular dynamics effects on luminescence properties of oligothiophene derivatives: a molecular mechanics-response theory study based on the CHARMM force field and density functional theory. *Phys Chem Chem Phys*, 13(39):17532–42, 2011.

[3] Jonas Sjöqvist, Mathieu Linares, Kurt V. Mikkelsen, and Patrick Norman. QM/MM-MD simulations of conjugated polyelectrolytes: A study of luminescent conjugated oligothiophenes for use as biophysical probes. *The Journal of Physical Chemistry A*, 118(19):3419–3428, April 2014.

[4] Jonas Sjöqvist, Jerôme Maria, Rozalyn A. Simon, Mathieu Linares, Patrick Norman, K. Peter R. Nilsson, and Mikael Lindgren. Toward a molecular understanding of the detection of amyloid proteins with flexible conjugated oligothiophenes. *The Journal of Physical Chemistry A*, 118(42):9820–9827, October 2014.

[5] Kenneth S. Schweizer. Configurational dependence of the optical properties of pi-conjugated polymers. I. Strong disorder limit. *The Journal of Chemical Physics*, 85(7):4181, 1986.

[6] R. Chang, J.H. Hsu, W.S. Fann, K.K. Liang, C.H. Chang, M. Hayashi, J. Yu, S.H. Lin, E.C. Chang, K.R. Chuang, and S.A. Chen. Experimental and theoretical investigations of absorption and emission spectra of the light-emitting polymer MEH-PPV in solution. *Chem. Phys. Lett.*, 317, 2000.

[7] Vladimir Dobrosavljević and Richard M. Stratt. Role of conformational disorder in the electronic structure of conjugated polymers: Substituted polydiacetylenes. *Physical Review B*, 35(6):2781–2794, 1987.

[8] Z. G. Soos and K. S. Schweizer. Absorption spectrum of flexible conjugated polymers: The weak-disorder limit. *Chem. Phys. Lett.*, 139(2):196–200, 1987.

[9] William Barford and Jonathan R. Mannouch. Torsionally induced exciton localization and decoherence in pi-conjugated polymers. *The Journal of Chemical Physics*, 149(21):214107, December 2018.

[10] William Barford and Max Marcus. Perspective: Optical spectroscopy in pi-conjugated polymers and how it can be used to determine multiscale polymer structures. *The Journal of Chemical Physics*, 146(13):130902, April 2017.

[11] Robert Binder and Irene Burghardt. First-principles quantum simulations of exciton diffusion on a minimal oligothiophene chain at finite temperature. *Faraday Discussions*, 221:406–427, 2020.

[12] Dmitry V. Makhov and William Barford. Local exciton ground states in disordered polymers. *Physical Review B*, 81(16), 2010.

[13] M. Marcus, O. R. Tozer, and W. Barford. Theory of optical transitions in conjugated polymers. II. Real systems. *J Chem Phys*, 141(16):164102, 2014.

[14] Alessandro Troisi and Alex Shaw. Very large pi-conjugation despite strong nonplanarity: A path for designing new semiconducting polymers. *The Journal of Physical Chemistry Letters*, 7(22):4689–4694, November 2016.

Chapter 7

Conclusions

7.1 Summary of thesis achievements

In this thesis I set out to contribute to the knowledge of property-structure relationship of conjugated polymers, specifically how conformational changes of a polymer affect the absorption strength, and thus the efficiency of an organic solar cell. I proposed that in order to further our understanding of the relationship between the morphology of organic semiconductors and their optical properties it is necessary to implement a coarse grained model with a more rigorous treatment of electron-hole interactions than commonly used semi-empirical models.

In chapter 4 I presented two case studies on how TDDFT can be used to investigate the conformation dependent absorption strength polythiophene and the two small molecules IDTBR and IDFBR. It was shown that the oscillator strengths of these materials are very sensitive to small changes in geometry, such as coplanarity and colinearity of neighbouring units. DFT is a good tool to determine the minimum energy conformation of individual polymer fragments or small molecules, which can then be used to estimate the material's optical properties and compare it against other materials. However, in practice a large variety of conformations of molecule or polymer chain may be present in a solid film resulting from the processing conditions, as well as presence of other blend components and phases. Thus, in order to determine the optical absorption properties of an organic material, it is important to perform excited state calculations

on large numbers of macromolecules in different conformations, and this exceeds the length scales that can be accessed practically by TDDFT.

In chapter 5 I presented the W-CIS approach - a coarse-grained method to calculate the excited states of conjugated oligomers that uses parameters obtained from ab initio calculations. I compared the approach to its *ab initio* counterpart CIS and the simpler semi-empirical Frenkel exciton model to conclude that the W-CIS offers a promising compromise between the two - it has the high computational efficiency of a semi-empirical model, but delivers results for optical absorption strength that are in good agreement with ab initio methods. Thus, the W-CIS method is well suited to further explore the optical absorption properties, especially the absorption strength, of conjugated materials in order to explain the origin of high absorption materials and contribute to design rules of new materials for high efficiency solar cells. However, it is worth noting that for now the approach has only been tested on single chains of homopolymers with relatively small repeat units (polyacetylene and polythiophene) and further work is needed to evaluate the limitations of the method when applied to more complex structures.

In chapter 6 I used the W-CIS approach to investigate the effect of varying conformation on the optical properties of two homopolymers, specifically varying the bond length alternation of oligoacetylenes and varying the dihedral angle of oligothiophenes. I showed how the effects of these conformational changes on the optical absorption spectra can be linked to changes in the model parameters characterising the electronic intermonomer interactions, such as HOMO and LUMO coupling energies, electron-hole Coulomb interactions and intermonomer transition dipole moments. Thus, not only does the W-CIS approach offer a more accurate alternative to other commonly used coarse grained models for excited state calculations such as the Frenkel exciton model, it also enables a more intuitive analysis on the origin of conformation dependent optical absorption properties.

To conclude, this work establishes a basis for multi-scale studies on how the knowledge of electronic properties of molecular scale systems can be combined with the knowledge of the relative position and orientation of molecular components in order to understand the macroscopic absorption properties of known compounds. It also showed how this knowledge can be used to

design new organic materials that would exhibit high optical absorption.

7.2 Applications and future work

The ultimate goal of the W-CIS approach presented in this thesis is to enable the modelling of optical properties of a molecular material exhibiting complex morphologies. This could be done by constructing and solving the model Hamiltonian for many conformations of single or multiple polymer chains or molecular crystals, whose structures might be extracted, for example, from molecular dynamics (MD) simulations. Following the calculations presented in chapter 6, such a procedure would involve coarse-graining each MD snapshot, calculating the Wannier functions for appropriate building blocks (monomers, groups of monomers or molecules, depending on the extent of the Wannier functions representing the frontier orbitals) and calculating the electronic coupling elements, Coulomb interactions and transition dipole moments. The most time consuming stage in the current implementation is obtaining the Wannier functions (WFs) representing the HOMO and LUMO of the system in question, as described in section 5.2.2. It would save computational time if the WFs could be calculated for a subset of possible configurations, for example, only for particular torsion angles as was done in chapter 6, and values of parameters for other configurations can be obtained by interpolation. This would allow the model Hamiltonian to be populated more quickly for a larger range of structures and allow more complex molecular morphologies to be sampled.

In chapters 5 and 6, I have demonstrated that the approach can be applied to study the optical properties of two homopolymers with relatively small repeat units as a function of oligomer length and simple geometric degrees of freedom, specifically carbon-carbon bond length alternation and dihedral angle. In order to extend the approach and apply it to more complex structures, further work needs to be done. First, the method should be validated more extensively against traditional methods for calculating excited states such as TDDFT. In chapter 5 the method was compared to *ab initio* CIS, which is a natural methodological comparison. Analysis of the same system (trans-oligothiophene) using TDDFT in chapter 4 and W-CIS in

chapter 6 led to qualitatively and quantitatively similar results but with differences, for example, in transition energies and in the length at which specific absorption peaks. A deeper comparison of model systems using W-CIS, CIS and TDDFT with possible extension to other excited state methods would be necessary to calibrate the method and interpret its predictions. At the same time the method should be compared with other electron-hole Hamiltonian-based coarse grained approaches for excited states of π-conjugated systems.

A key limitation of the model that is worth pointing out is the neglect of vibrational modes, as well as the limitation to steady state conditions. In future developments vibrational modes should be included in order to better reproduce experimental spectra. Vibrational dynamics are necessary to enable dynamic simulations and in a future development they could be included following the treatment of electron-phonon interactions implemented in [1]. Incorporating excited state dynamics would allow basic processes such as exciton transfer and charge separation to be modelled within a coarse-grained molecular assembly [2].

One of the advantages of the W-CIS approach compared to the widely used Frenkel exciton model is its capability to model both Frenkel type and charge transfer excitons in the same system. Thus, an interesting application where the W-CIS approach could enable promising insights is modelling excited states and charge transfer events at the interface between a conjugated polymer and a molecular acceptor. Recent experimental evidence suggests charge transfer at such interfaces can occur with minimal free-energetic driving force [3][4] but little is known about how such phenomena depend upon the relative orientation and position of the donor and acceptor units. The W-CIS approach provides an attractive way to study how the excited states and their energetics depend on the geometry and chemical structure of the donor and acceptor units. In follow-up work within our group, the approach is being adapted to study the nature of excited states at donor:acceptor molecular interfaces within larger molecular assemblies.

Bibliography

[1] Stoyan Karabunarliev and Eric R. Bittner. Polaron–excitons and electron–vibrational band shapes in conjugated polymers. *The Journal of Chemical Physics*, 118(9), 2003.

[2] Matthias Polkehn, Pierre Eisenbrandt, Hiroyuki Tamura, and Irene Burghardt. Quantum dynamical studies of ultrafast charge separation in nanostructured organic polymer materials: Effects of vibronic interactions and molecular packing. *International Journal of Quantum Chemistry*, 118(1):e25502, 2018.

[3] Lorena Perdigón-Toro, Huotian Zhang, Anastasia Markina, Jun Yuan, Seyed Mehrdad Hosseini, Christian M Wolff, Guangzheng Zuo, Martin Stolterfoht, Yingping Zou, Feng Gao, et al. Barrierless free charge generation in the high-performance PM6: Y6 bulk heterojunction non-fullerene solar cell. *Advanced Materials*, 32(9):1906763, 2020.

[4] Ardalan Armin, Wei Li, Oskar J Sandberg, Zuo Xiao, Liming Ding, Jenny Nelson, Dieter Neher, Koen Vandewal, Safa Shoaee, Tao Wang, et al. A history and perspective of non-fullerene electron acceptors for organic solar cells. *Advanced Energy Materials*, page 2003570, 2021.